

ABSTRACT

Title of Document: SYNTHESIS, CHARACTERIZATION, AND KINETIC STUDIES OF IONIZING RADIATION-INDUCED INTRA- AND INTER-CROSSLINKED POLY(VINYL PYRROLIDONE) NANOHYDROGELS

Jung-Chul An, Doctor of Philosophy, 2007

Directed By: Professor Mohamad Al-Sheikhly, Department of Materials Science and Engineering

A polymer nanohydrogel can be defined as a three-dimensional polymer network composed of hydrophilic crosslinked macromolecular chains filled with liquid and possessing a diameter of $1-10^2$ nanometers. Nanohydrogels have drawn huge interest due to their potential applications, such as target-specific drug delivery carriers, absorbents, chemical/biological sensors, and bio-mimetic materials. However, the conventional methods of nanohydrogel synthesis require toxic chemicals (e.g., initiators, crosslinking agents) to form the gel structure. The additional steps required to remove unreacted or residual (undesired) substances cause nanohydrogel fabrication to be complicated, environmentally unfriendly, and unsuitable for biomedical use.

This study aims to develop simple and efficient methods of producing nanohydrogels from polymeric, aqueous solutions using ionizing radiation.

Poly(vinyl pyrrolidone) (PVP) nanohydrogels of various sizes and molecular weights were prepared by pulsed electron beam and steady-state gamma irradiation at different doses (5 and 10 kGy; $1\text{Gy} = 1\text{ J kg}^{-1}$) and temperatures (20 to $77\text{ }^{\circ}\text{C}$). The pervaded volume of the PVP chains becomes smaller at high temperatures (above $50\text{ }^{\circ}\text{C}$) due to the disruption of hydrogen bonds between water and PVP molecules which reduces the size and the molecular weight of the synthesized PVP nanohydrogels. The synthesis parameters (e.g., irradiation temperature, pulse repetition rate, dose rate, and solution concentration) were varied in order to control the size and the average molecular weight of the irradiated sample. In the absence of oxygen, the radiolytically produced free radicals of the thermally collapsed PVP molecules primarily underwent intra-crosslinking reactions, along with a minor contribution from inter-crosslinking reactions. The predominance of the intra-crosslinking mechanism was exhibited at high irradiation temperature ($77\text{ }^{\circ}\text{C}$) in dilute solutions ($c = 0.9 \times 10^{-2}\text{ mol L}^{-1}$). The formation of carbon-centered free radicals along the backbone of the PVP chain at higher pulse repetition rate (300 pulses per second) was found to enhance the intra-crosslinking reaction, thereby leading to the formation of smaller nanohydrogel molecules containing an average hydrodynamic radius (R_h) of $9.9 \pm 0.1\text{ nm}$.

SYNTHESIS, CHARACTERIZATION, AND KINETIC STUDIES OF
IONIZING RADIATION-INDUCED INTRA- AND INTER-CROSSLINKED
POLY(VINYL PYRROLIDONE) NANOHYDROGELS

By

Jung-Chul An

Dissertation submitted to the Faculty of the Graduate School of the
University of Maryland, College Park, in partial fulfillment
of the requirements for the degree of
Doctor of Philosophy
2007

Advisory Committee:
Professor Mohamad Al-Sheikhly, Chair
Professor Lourdes G. Salamanca-Riba
Professor Emeritus Joseph Silverman
Professor Mikhail Anisimov
Dr. Dianne L. Poster

© Copyright by
Jung-Chul An
2007

Dedication

To my loving wife Soon Mo
for her endless encouragement and love,
and
To my loving parents and children
for their patience.

Acknowledgements

First, I would like to express my deepest gratitude to my advisor, Professor Mohamad Al-Sheikhly, for his encouragement, inspiration, and endless patience throughout my work. He has always been my strongest supporter; with invaluable, sage guidance, talent, and good humor which alleviated my difficult days.

I would like to acknowledge Professor Emeritus Joseph Silverman. His borderless knowledge and scientific insight allowed me to investigate a subject from a fundamental aspect. I am also grateful to Dr. Dianne Poster, Research Scientist in the Analytical Chemistry Division at the NIST, for her generous support in the chemical characterizations at NIST, as well as her agreement to serve on my dissertation committee. I extend thanks to Dr. Wyatt N. Vreeland, Chemical Engineer at the NIST, for his guidance in using asymmetric flow field flow fractionation (AFFFF) chromatography and other technical advice. I also owe thanks to Professor Mikhail Anisimov in the Department of Chemical and Biomolecular Engineering for his support in light scattering and also serving as the Dean's representative on my dissertation committee. My appreciation extends to Dr. Andrei Kostko for valuable discussions and training in light scattering analysis. I must thank Professor Lourdes Salamaca-Riba for her thoughtful suggestions and service on my dissertation committee. I would like to acknowledge Mr. Vincent Adams. My experiments could not have been accomplished without his devoted technical support in using the Radiation Facilities at the University of Maryland.

I want to thank all the colleagues in my research group for their humor and encouragement which rejuvenated me even in the hardest of times. The collaboration I experienced here was what the best team could exhibit.

Finally, my gratitude goes to my loving parents and sister. I could not have done this work without their sacrifice, patience, and generosity. Also, I would like to thank all friends in church for their prayers. And thank God for everything.

Table of Contents

Dedication.....	ii
Acknowledgments.....	iii
Table of Contents.....	v
List of Tables.....	vii
List of Figures.....	viii
Chapter 1:.....	1
INTRODUCTION.....	1
Chapter 2:.....	4
BACKGROUND.....	4
2.1 Polymer Nanohydrogel and its Biomedical Importance.....	4
2.2 Radiation Physics and Chemistry.....	9
2.2.1 Interactions of Radiation with Matter.....	9
2.2.2 Gamma Rays.....	11
2.2.3 Electrons.....	13
2.2.4 Radiation Chemical Yield.....	14
2.2.5 Radiation Chemistry of Aqueous Systems.....	15
2.2.6 Reaction Mechanism of e_{aq}^- and $\bullet OH$ with Polymer.....	18
2.3 Radiation Facilities and Dosimetries.....	24
2.3.1 Linear Accelerator Radiation Facility.....	24
2.3.2 Gamma Radition Facility.....	26
2.3.3 Dosimetry.....	28
2.3.3.1 Fricke Dosimetry.....	28
2.3.3.2 Potassium-Thiocyanate Dosimetry.....	31
2.3.3.3 Radiochromic Film Dosimetry.....	32
2.4 Kinetic Measurements (Pulse Radiolysis).....	33
2.5 Characterization Techniques.....	38
2.5.1 Dynamic Light Scattering (DLS).....	38
2.5.2 Asymmetric Flow Field Flow Fractionation (AF4) Chromatography.....	43
2.5.3 Atomic Force Microscopy (AFM).....	49
2.5.4 Environmental Scanning Electron Microscopy (ESEM).....	50
Chapter 3:.....	52
RADIATION-INDUCED SYNTHESIS OF NANOHYDROGELS.....	52
3.1 Introduction and Previous Works.....	52
3.2 Materials and Sample Preparations.....	57
3.3 Results.....	58
3.3.1 Processing Parameter Effects in Electron Beam Irradiation.....	58
3.3.2 Topographical Observations of Nanohydrogels by AFM.....	69
3.3.3 Thermal and Dose-Rate Effects in Steady-State Radiolysis of PVP Aqueous Solutions.....	71
3.4 Discussion and Conclusions.....	76
Chapter 4:.....	80
KINETICS OF FREE RADICAL REACTIONS.....	80

4.1 Introduction and Previous Works	80
4.2 Experiments and Results	81
4.2.1 Absorption Spectra of Transient Species	81
4.2.2 Reaction Rate Constant for Polymer Radical Reaction	86
4.2.3 Activation Energy of Polymer Radical Decay.....	93
4.3 Discussion and Conclusions.....	95
Chapter 5:.....	97
TEMPLATE-ASSISTED SYNTHESIS OF NANOHYDROGELS.....	97
5.1 Introduction and Previous Works	97
5.2 Experiments and Results.....	101
5.3 Discussion and Conclusions.....	109
Chapter 6.....	110
RECOMMENDATION FOR FUTURE WORKS.....	110
6.1 Stimuli-Responsive Nanohydrogels	110
6.2 Magnetic Nanoparticles Embedded Hydrogels.....	112
6.3 Nanohydrogels Prepared by Nano-phase Separation	113
6.4 Gel Nanoparticles Network.....	116
Appendix	118
AFFFF Results of the PVP Nanohydrogels.....	118
References.....	139

List of Tables

Table 2.1	Yield of ferric ions in the electron irradiation of oxygen-containing solutions of ferrous sulfate in 0.4 M sulfuric acid.....	29
Table 3.1	Weight averaged molecular weights (M_w , g mol ⁻¹) of the PVP samples ($c = 0.9 \times 10^{-2}$ mol L ⁻¹) synthesized at various temperatures	60
Table 3.2	Weight averaged molecular weights (M_w , g mol ⁻¹) of the PVP samples ($c = 0.45 \times 10^{-2}$ mol L ⁻¹) synthesized at 77 °C.	60
Table 3.3	Crosslinking parameters (c_x , G_x) of the synthesized PVP products at different concentrations; irradiation temperature = 77 °C.....	64
Table 3.4	Weight averaged molecular weights (M_w , g mol ⁻¹) of the PVP samples synthesized by γ -ray irradiation at 77 °C.....	74

List of Figures

Figure 1	Applications of nanohydrogels.....	1
Figure 2.1	Particle size effects in the evasion of the reticulo-endothelial system (RES).....	6
Figure 2.2	Target-specific drug delivery with an aid of EPR (Enhanced Permeability and Retention) effect.....	7
Figure 2.3	Simplified scheme of the spur model for the track of an energy-rich electron water (the distance between neighboring spurs in the track of the primary electron is drawn too short by a factor of 20, those of the σ -electron by a factor of 6).....	10
Figure 2.4	Compton Scattering; The energy and momentum of the incident photon are shared between the scattered photon and the recoiling electron.....	12
Figure 2.5	Space-Time development of a spur in a dilute, aqueous system.....	16
Figure 2.6	Reaction mechanisms of hydrated electrons with PVP.....	18
Figure 2.7	Reaction mechanisms of hydroxyl radicals with PVP.....	19
Figure 2.8	H transfer reaction mechanism of PVP carbon-centered free radicals.....	20
Figure 2.9	Disproportionation reaction mechanism of PVP carbon-centered free	

	radicals.....	21
Figure 2.10	The crosslinking reaction schematics: inter-molecular (a), intra-molecular crosslinking (b).....	22
Figure 2.11	Schematic of major functional component of the UMCP LINAC (Magnetron and Vac Ion Pump shown reversed).....	25
Figure 2.12	The UMCP LINAC facility.....	25
Figure 2.13	Schematic of the UMCP ⁶⁰ Co Gamma sources & housing.....	27
Figure 2.14	The UMCP ⁶⁰ Co Gamma facility.....	27
Figure 2.15	A calibration curve for the radiochromic film dosimetry in this work; The changes of the absorption of the Far West radiochromic films (Lot No. UM 35) at 605 nm were measured at the dose range of 0.5 to 70 kGy by the spectrophotometer.....	32
Figure 2.16	Schematic diagram of pulse radiolysis analysis system.....	33
Figure 2.17	The photomultiplier signal profile.....	34
Figure 2.18	The typical bimolecular decay of the (CNS) ₂ ⁻ monitored at 480 nm in the air-saturated solution.....	36
Figure 2.19	General correlation function plot (a) and corresponding R _h distribution analysis (b) from the DLS measurement of unirradiated PVP aqueous solution (c = 9 x 10 ⁻² mol L ⁻¹) at 25°C.....	41

Figure 2.20	Schematic of DLS apparatus at the UMCP.....	42
Figure 2.21	DLS apparatus: Photocor Complex system	42
Figure 2.22	Schematic of separation mechanism of AFFFF chromatography.....	44
Figure 2.23	AFFFF equipments for the measurements of R_h and molar mass.....	48
Figure 2.24	UV-VIS absorbance spectrum of PVP aqueous solution.....	49
Figure 2.25	Schematic of atomic force microscope.....	50
Figure 3.1	Properties of PVP in aqueous solution as a function of an average absorbed dose; M_w of PVP = $1.3 \times 10^6 \text{ g mol}^{-1}$, dose/pulse = 0.32 kGy, pulse frequency = 0.5 Hz, pulse duration (width) = 2 μs	53
Figure 3.2	Schematic illustration of the formation process of PVA microgels during γ -ray irradiation.....	53
Figure 3.3	Keto-enol tautomerism in the pyrrolidone ring of PVP.....	56
Figure 3.4	D_t and R_h of PVP polymer chains ($M_w = (3.94 \pm 0.12) \times 10^5 \text{ g mol}^{-1}$) as a function of temperature.....	59
Figure 3.5	Differential molar mass distribution of the PVP samples ($c = 0.9 \times 10^{-2}$ mol L^{-1}) synthesized at 20 °C with the irradiation conditions: 5 kGy at 300 Hz (a-1), 5 kGy at 20 Hz (a-2), 10 kGy at 300 Hz (a-3), 10 kGy at 20 Hz (a-4). P is unirradiated PVP.....	61

Figure 3.6	Differential molar mass distribution of the PVP samples ($c = 0.9 \times 10^{-2}$ mol L ⁻¹) synthesized at 60 °C with the irradiation conditions: 5 kGy at 300 Hz (b-1), 5 kGy at 20 Hz (b-2), 10 kGy at 300 Hz (b-3), 10 kGy at 20 Hz (b-4). P is unirradiated PVP.....61
Figure 3.7	Differential molar mass distribution of the PVP samples ($c = 0.9 \times 10^{-2}$ mol L ⁻¹) synthesized at 77 °C with the irradiation conditions: 5 kGy at 300 Hz (c-1), 5 kGy at 20 Hz (c-2), 10 kGy at 300 Hz (c-3), 10 kGy at 20 Hz (c-4). P is unirradiated PVP.....62
Figure 3.8	Differential molar mass distribution of the PVP samples ($c = 0.45 \times 10^{-2}$ mol L ⁻¹) synthesized at 77 °C with the irradiation conditions: 5 kGy at 300 Hz (d-1), 5 kGy at 20 Hz (d-2), 10 kGy at 300 Hz (d-3), 10 kGy at 20 Hz (d-4). P is unirradiated PVP.....62
Figure 3.9	c_x (a) and G_x (b) of the synthesized PVP nanohydrogels ($c = 0.9 \times 10^{-2}$ mol L ⁻¹) as a function of irradiation temperature at different doses and pulse repetition rates.....65
Figure 3.10	Change of R_h of the synthesized PVP nanohydrogels ($c = 0.9 \times 10^{-2}$ mol L ⁻¹) as a function of irradiation temperature at different pulse repetition rates; 5 kGy (a) and 10 kGy (b) as used total dose.....67
Figure 3.11	R_h of the synthesized PVP nanohydrogels with different concentrations ($c = 0.9 \times 10^{-2}$ and 0.45×10^{-2} mol L ⁻¹) at identical irradiation

	temperature (77 °C); 20 Hz (a) and 300 Hz (b) as used pulse repetition rate.....	68
Figure 3.12	Atomic force microscopy images of the dried films of the cast aqueous PVP solutions: a planar view and a cross-sectional profile of the linear PVP (a) and the nanohydrogels of PVP (b), 3D views of the linear PVP (c) and the nanohydrogels of PVP (d).....	70
Figure 3.13	Change of R_h of the PVP polymer nanohydrogels synthesized by γ -ray irradiation as a function of temperature (a) and dose at 77 °C (b).....	73
Figure 3.14	Differential molar mass distribution of PVP samples ($c = 0.9 \times 10^{-2}$ mol L ⁻¹) synthesized by γ -ray irradiation at 77 °C with the irradiation conditions; 5 kGy (I) and 10 kGy (II). P is unirradiated PVP.....	74
Figure 3.15	PVP samples prepared by γ -ray irradiation at 20 °C with the solution concentrations from 0.1 wt% (0.9×10^{-2} mol L ⁻¹) to 1.1 wt% (9.9×10^{-2} mol L ⁻¹).....	75
Figure 3.16	Average R_h of the PVP nanohydrogels synthesized by γ -ray irradiation at different temperatures and concentrations.....	75
Figure 3.17	Schematic diagram of the mixed crosslinked PVP nanohydrogels formation; dilute solution of PVP ($c = 0.9 \times 10^{-2}$ mol L ⁻¹) (a), collapsed coils at high temperature (b), diffusive interaction of coils (c), C-centered radical formation upon ionizing radiation (d), intra- and inter-crosslinks formation of PVP chains (e).....	78

Figure 4.1	The comparison of build up between N ₂ O- and air-saturated KSCN solutions monitored at 480 nm.....	82
Figure 4.2	Absorption spectrum of the transient species formed (measured at 2 μs after 3 μs width pulse) by pulse radiolysis of N ₂ O-saturated 0.9 x 10 ⁻² mol L ⁻¹ PVP (M _w = (3.94 ± 0.12) x 10 ⁵ g mol ⁻¹) aqueous solution at 25 °C. Inset is the buildup profile of the transient species at 390 nm.....	83
Figure 4.3	Absorption spectrum of the transient species of N ₂ O-saturated PVP aqueous solution (measured at 2 μs after 3 μs width pulse) at 25 °C; concentration of PVP solution is 0.9 x 10 ⁻² mol L ⁻¹ and molecular weight of PVP is 4 x 10 ⁴ g mol ⁻¹ . Inset is the buildup profile of the transient species at 390 nm	84
Figure 4.4	Chemical structures of N-vinyl pyrrolidone (VP) (a) and Poly(vinyl pyrrolidone) (PVP).....	84
Figure 4.5	Absorption spectrum of the transient species of N ₂ O-saturated VP aqueous solution (measured at 1 μs after 3 μs width pulse) at 25 °C; concentration of VP solution is 0.5 x 10 ⁻² mol L ⁻¹	85
Figure 4.6	Change of molar absorption coefficient (ε _{390 nm}) as a function of temperature in N ₂ O-saturated PVP aqueous solutions (c = 0.9 x 10 ⁻² mol L ⁻¹).....	86

Figure 4.7	Second order decay profile of the transient species at 390 nm in N ₂ O-saturated PVP aqueous solutions ($c = 0.9 \times 10^{-2} \text{ mol L}^{-1}$) at 25 °C....	87
Figure 4.8.1 – 4.8.9	Decay profiles of (PVP-H) [•] radicals monitored at 390 nm in N ₂ O-saturated PVP solutions ($c = 0.9 \times 10^{-2} \text{ mol L}^{-1}$) at various temperatures in the range of 28 – 77 °C.....	88 - 92
Figure 4.9	Change of the second order reaction (decay) rate constant ($2k_2$) as a function of temperature in N ₂ O-saturated PVP aqueous solutions ($c = 0.9 \times 10^{-2} \text{ mol L}^{-1}$).....	93
Figure 4.10	Arrhenius plot of the PVP radical decay rate constant from which average activation energies: $E_a = 1.0 \pm 0.4 \text{ kcal mol}^{-1}$ (I) and $6.8 \pm 1.9 \text{ kcal mol}^{-1}$ (II) were derived for two different temperature regions in N ₂ O-saturated PVP aqueous solutions ($c = 0.9 \times 10^{-2} \text{ mol L}^{-1}$).....	94
Figure 5.1	Schematic of a real chain confined in a cylinder of diameter D	98
Figure 5.2	Schematic illustration of the formation of PVP nanostructures and the FESEM images of PVP nanotubes (a) and PVP nanowires (b).....	99
Figure 5.3	ESEM image of the cross section of alumina nanoporous membrane used in this experiment; The highly ordered open pore and capillary structure found with the average diameter of 200 nm and the height of 60 μm.....	102

Figure 5.4	<p>Schematic procedure of the template-assisted γ-ray irradiation; contact the nanoporous membrane on PVP aqueous solution (1), introduce solution into the capillaries of the membrane (2), steady-state ionizing radiation (γ-ray) to produce the crosslinked gel structure in trapped PVP within the capillaries of the membrane (3), separate PVP nanohydrogels from membrane by dissolving it in a sodium hydroxide solution (4).....</p>	103
Figure 5.5	<p>ESEM micrographs of the synthesized PVP nanohydrogels from N_2O-saturated PVP aqueous solutions ($c = 9 \times 10^{-2} \text{ mol L}^{-1}$) by the nano-template assisted γ-ray irradiation with a dose of 10 kGy at 25 °C; micrograph magnifications are 30,000x (a) and 50,000x (b).....</p>	105
Figure 5.6	<p>AFM micrographs of the synthesized PVP nanohydrogels from N_2O-saturated PVP aqueous solutions ($c = 9 \times 10^{-2} \text{ mol L}^{-1}$) by the nano-template assisted γ-ray irradiation with a dose of 10 kGy at 25 °C: planar view (a) and 3D view (b) (scanned area = 2 x 2 μm for both pictures).....</p>	106
Figure 5.7	<p>AFM micrographs of the synthesized PVP nanohydrogels from N_2O-saturated PVP aqueous solutions ($c = 9 \times 10^{-2} \text{ mol L}^{-1}$) by the nano-template assisted γ-ray irradiation with a dose of 10 kGy at 25 °C: planar view (a) and 3D view (b) (scanned area = 0.85 x 0.85 μm (a), 0.8 x 0.8 μm (b)).....</p>	107

Figure 5.8	FTIR spectra of the unirradiated (PVP-raw) PVP and the synthesized nanohydrogels from N ₂ O-saturated PVP aqueous solutions ($c = 9 \times 10^{-2} \text{ mol L}^{-1}$) by the nano-template assisted γ -ray irradiation with a dose of 10 kGy at 25 °C (PVP-10kGy).....	108
Figure 6.1	Schematics of the stimuli-responsive nanohydrogels: pH-responsive poly(acrylic acid), PAA (a), temperature-responsive poly(N-isopropyl acrylamide), pNIPAAm (b); LCST stands for lower critical solution temperature.....	111
Figure 6.2	G_{ij} functions vs. the mole fraction of water x_1 for water (1) – organic component (2) (i.e., acetone) mixtures at 25 °C.....	114
Figure 6.3	R_h distribution (with average $R_h = 98 \pm 5 \text{ nm}$) of the PVP nanohydrogels synthesized by nano-phase separation technique; total irradiated dose = 10 kGy, $9 \times 10^{-2} \text{ mol L}^{-1}$ PVP in water/acetone mixture.....	115
Figure 6.4	The hierarchical structure of the gel nanoparticles network.....	116
Figure 6.5	The synthesis route for the multi-functional and multi-component gel nanoparticles network.....	117

Polymer gels may be categorized by their dimensions as either nano- or macroscopic gels, and each type may be selectively produced through the control of the gel-forming crosslinking reactions used to produce them. The inter-molecular crosslinking process which yields macroscopic gels has been extensively studied and is relatively well understood [5-8]. However, the radiation-induced synthesis of polymer nanogels, which is based on an intra-molecular crosslinking process, is less explored. An understanding of the mechanism of crosslink formation is very important in order to control the final, physical properties (e.g., size, conformation, molecular weight, crosslinking density, etc.) of the produced nanohydrogel materials.

In this work, polymer nanohydrogels were prepared from dilute poly(vinyl pyrrolidone) (PVP) aqueous solutions by means of irradiation with either pulsed, high energy electrons or steady-state γ -rays. The effects of radiation synthesis parameters (e.g., total dose, pulse repetition rate, etc.) as well as physical parameters (e.g., solution concentration and irradiation temperature) on the nanohydrogel products are presented in Chapter 3.

Pulse radiolysis was used to study the kinetics of gel-forming crosslinking reactions, and is discussed in Chapter 4. The second order decay of carbon-centered free radicals on the PVP backbone through inter- and intra-molecular crosslinking was observed. Changes in the PVP chain conformation at different temperatures were also found to affect the kinetics of these radical reactions.

Chapter 5 is devoted to the discussion of a novel synthesis process of PVP nanohydrogels through the irradiation of samples within a nano-template. Chapter 6

contains recommendations for future work which are based on the research presented in this dissertation. Studies of various stimuli-responsive functional nanohydrogels will be carried out and extended through investigations of their physicochemical properties. A novel process for the synthesis of nanohydrogels through the irradiation of nano-phase separated materials is described, and the preliminary result of this work is discussed. Proposed experiments for the formation of multi-functional and multi-component gel nanoparticle structures will also be discussed.

Chapter 2:

BACKGROUND

2.1 Polymer nanohydrogel and its biomedical importance

A hydrogel is composed of two-components: a three-dimensional polymer network and water. The combination of these components forms a material that exhibits both good fluidity and mechanical stability [9]. The chains of the polymer are chemically crosslinked by stable and flexible covalent bonds [9]. A hydrogel typically has a very low shear modulus and a disordered structure containing a considerable amount of water [10]. This network can be swollen and retain concentrations of liquid 100 times (or more) its dry weight if the solvent is compatible with the polymeric component (i.e., a good solvent for the polymer in its uncrosslinked form). The equilibrium concentration is a function of the crosslink density, chemical composition, and surrounding environment. Bio- or medical materials are the most anticipated applications of polymer hydrogels. Polymer systems have many advantages over conventional lipid –based vesicles which cause them to be more conducive to drug loading, storage stability, and *in vivo* controlled drug release [11, 12].

Classical methods used to synthesize micro- and nano-sized polymeric gel particles are based on conventional, thermally initiated polymerization, usually in an emulsion [13, 14]. However, these preparation methods are often accompanied by toxic monomers, initiators, crosslinking agents, etc. These unreacted substances must

be completely and carefully removed from the final product, which is a disadvantage for use in biomedical applications. These requirements demonstrate the need for a safe and clean alternative synthesis method.

Ionizing radiation techniques have already been proven to be advantageous in the synthesis of macroscopic hydrogels, particularly those for biomedical applications (e.g., wound dressing and controlled drug delivery devices [6, 15]). These techniques, as explained in Chapter 2.2.6, are based on the ionizing radiation-induced production of hydroxyl radicals and hydrogen atoms in water, which subsequently react with macromolecules to yield randomly dispersed polymer radicals. These radicals undergo recombination to form permanent covalent bonds. When a sufficient dose is applied, all the chains become linked together into a three-dimensional network.

Pulse radiation (i.e., pulsed electron beam radiation-induced radiolysis) is an alternative technique to synthesize nanohydrogels [16, 17]. This method involves the application of a succession of short and intense pulses of electrons to rapidly generate carbon-centered radicals on individual polymer backbones. It promotes a crosslinking reaction within the same chain (intra-crosslinking) through radical recombination while suppressing the formation of crosslinks between different chains (inter-crosslinking). Since the only substances contained in the system are polymer molecules and water, potentially harmful agents are excluded and purification steps can be omitted by using this procedure. Thus, this process is a clean, environment-friendly technique that does not involve the generation of waste, and has a very low cost. Ionizing radiation-induced crosslinking has unique advantages. Control of the process parameters (e.g., dose, dose rate, etc.) can be used to obtain either nano- or

microgels with various crosslink densities, molecular weights, and desired dimensions. High-energy ionizing radiation can also be used to sterilize the materials produced with a dose of 25 kGy. However, the dose requirements for the synthesis of hydrogels are usually less than 10 kGy. These potentially advantageous features, which are currently unmatched by conventional techniques, are important for the development of therapeutic systems based on nanohydrogels (e.g., target-specific drug delivery). Nanohydrogels may serve as matrices for the intravenous controlled release of drugs, where the release rate and localization of release site are governed by the size and crosslink density of the gel [18, 19]. Nano-sized drug carriers can provide benefits with interesting features, such as an increased rate of response to external stimuli (i.e., response rate toward change of stimuli that is inversely proportional to the square of the size of the gel [20]) and higher circulation times in the blood stream which result in raised chances of drug delivery to specific organs through the evasion of the reticulo-endothelial system (RES) (Figure 2.1) [21, 22].

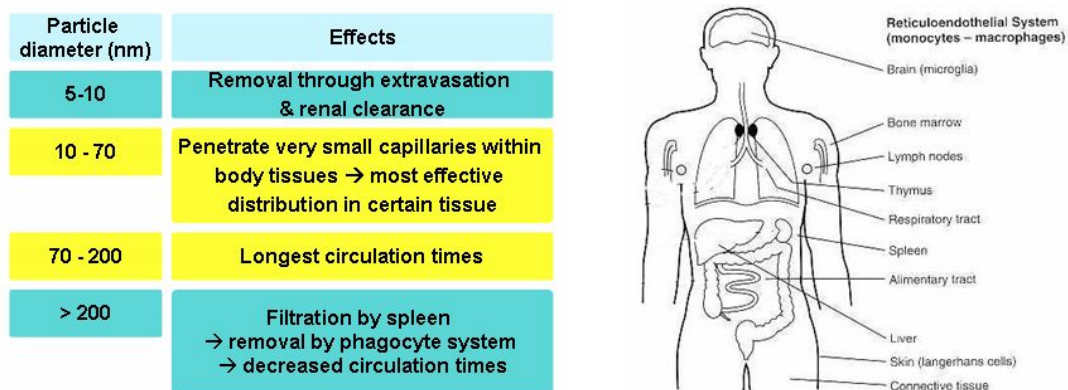


Figure 2.1. Particle size effects in the evasion of the reticulo-endothelial system (RES).

They are also effective carriers for target-specific drug delivery to tumor tissues. Nanoscopic particles can accumulate (in the passive mode) preferentially near tumor sites through what is known as the Enhanced Permeability and Retention (EPR) effect. The EPR effect is mediated by four major factors: (i) hypervascularity of tumor tissues due to active angiogenesis, (ii) defective anatomical structure of tumor blood vessels (leaks in the vessel walls), (iii) enhanced production of vascular mediators such as nitric oxide and bradykinin, and (iv) incomplete lymphatic drainage system [23].

Figure 2.2 shows the selective uptake of a nanohydrogel-drug conjugate within a tumor angiogenic vessel.

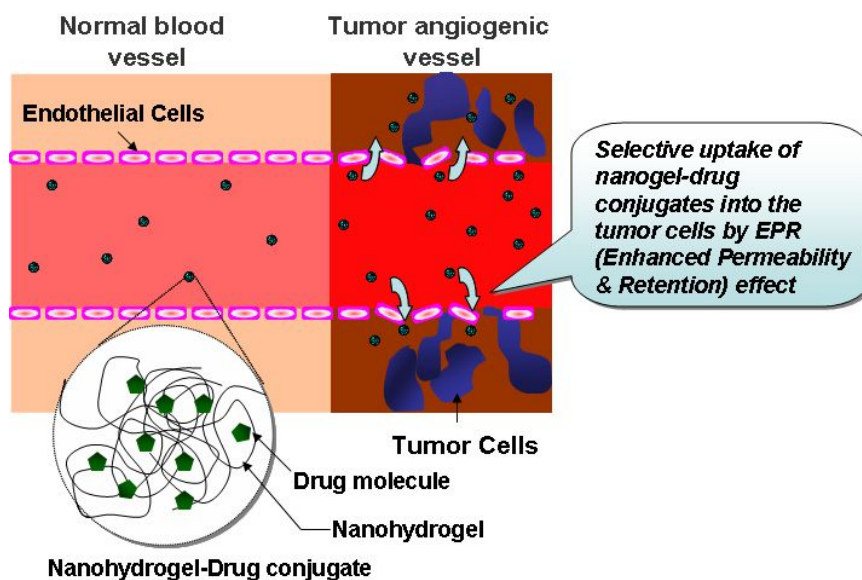


Figure 2.2. Target-specific drug delivery with an aid of EPR (Enhanced Permeability and Retention) effect.

Additional applications of nanohydrogels include carriers or cell markers for medical tests [24, 25], blocking agents for dental channels, synovial fluid substitutes, fast-response gels for stimuli-sensitive medical devices, artificial organs, etc. Absorbents,

rheology control additives, catalyst carriers in membrane reactors, and a matrix for DNA sequencing [26] can also be considered as the promising fields of applications.

2.2 Radiation physics and chemistry

In this chapter, the basic principles of radiation physics and chemistry are reviewed and adapted in order to explain the experimental system investigated in this work. The characteristics of different types of ionizing radiation sources and free radical reactions induced by ionizing radiation are discussed.

2.2.1 Interactions of radiation with matter

The types of radiation used in these experiments are steady-state radiolysis and pulsed electron irradiation using cobalt-60 (^{60}Co) radioisotope and electron beam linear accelerator respectively. The energy deposited in a complex homogeneous medium is proportional to the electron fraction of each component. The relative proportions of radiation-induced chemical products may vary by what is known as the linear energy transfer (LET) and the composition of the absorbing medium. LET ($\text{keV } \mu\text{m}^{-1}$) is associated with the nature and the energy of the incident radiation and is defined as the linear rate of energy loss of ionizing (charged) particles which are present in the radiation ray or arise from it while traversing a medium. Low LET radiation generates ions (e.g., anions, positive ions, and secondary electrons) and electronically excited species in the form of small clusters (spurs) or columnar tracks. These reactive species can then induce chemical changes in a material. As energy is transferred from fast charged particles to matter, the particles lose kinetic energy and leave behind a trail of ionized and excited species in their path. High-energy electrons traveling through water lose energy in discrete steps of approximately 100

eV to yield primary ionized species of the interaction, especially hydroxyl radicals and hydrated electrons [27, 28]. The volume in which energy is deposited at each discrete step is known as a spur. In water, the mean radius of a spur is approximately 1 nm and the mean separation between successive spurs is approximately 200 nm [27, 29]. The scheme of spur model is represented at following Figure 2.3 [30].

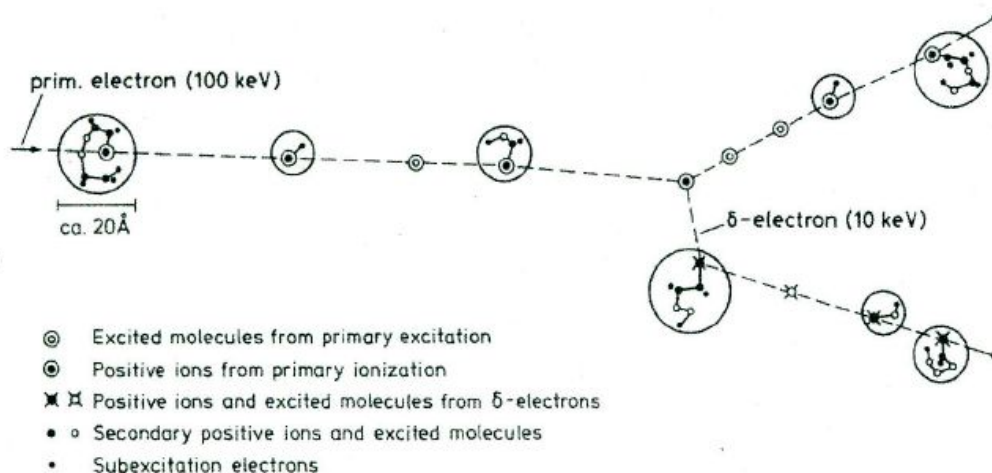


Figure 2.3. Simplified scheme of the spur model for the track of an energy-rich electron water (the distance between neighboring spurs in the track of the primary electron is drawn too short by a factor of 20, those of the δ -electron by a factor of 6) [30].

The primary chemical species are generated after physical deposition of the energy in less than 10^{-12} s.

Low LET radiation (such as high energy electron or γ -rays) induces more widely separated ionized and excited species in spurs, whereas high LET radiation (such as heavy charged particles (e.g., α -particles)) generates cylindrical particle tracks which are densely populated with spurs. ^{60}Co and electron beam accelerators are frequently used as radiation sources due to their relatively low cost, availability,

and convenience. Gamma photons from ^{60}Co and high energy electrons from electron beam accelerators produce secondary electrons when they interact with matter. The LET of 1.25 MeV gamma photons and 7 MeV electrons are approximately 0.2 eV nm^{-1} in aqueous media [31].

2.2.2 Gamma rays

Gamma rays are a form of electromagnetic radiation produced from the radioactive decay (e.g., ^{60}Co) with energies in the keV to MeV range. The ^{60}Co radioisotope emits a beta particle with energy of 0.31 MeV by beta decay and transforms into excited Nickel-60 ($^{60}\text{Ni}^*$), which contains a half life of 5.3 years. It then drops down to its ground state through the emission of two gamma rays with energies of 1.17 MeV and 1.33 MeV (1.25 MeV average energy) [28].



In the experimental facility used this work, the 0.31 MeV energy from beta decay is completely absorbed in the stainless steel cladding (wall thickness = 8 mm, shown in Figure 2.10) where ^{60}Co radioisotope material is enclosed, thereby causing its radiation effect to be negligible.

The major radiation interaction mechanisms of gamma rays include the photoelectric effect, Compton scattering, and pair production. In this experiment, the 1.25 MeV (average) energy of the ^{60}Co gamma ray lost most of its energy through Compton scattering. Compton scattering is an elastic interaction where an incident gamma photon transfers enough energy to eject a loosely bound or free atomic electron

within a material, causing the electron to be accelerated while the photon is deflected from the incident direction with reduced energy [27]. The probability of Compton scattering decreases as the energy of the photon increases. A schematic diagram of Compton scattering is shown in Figure 2.4 and the corresponding descriptive equation is given in Eq. (2.3) [27]. The excitation and ionization generated by the scattered photons become insignificant after several interactions, whereas the scattered Compton electrons produced are higher in energy and contribute more to the chemical changes which eventually take place in the material. A few Compton electrons can produce ionizing events on the order of 10,000, whereas a single 1.25 MeV gamma photon can only produce several ionization events before it disappears.

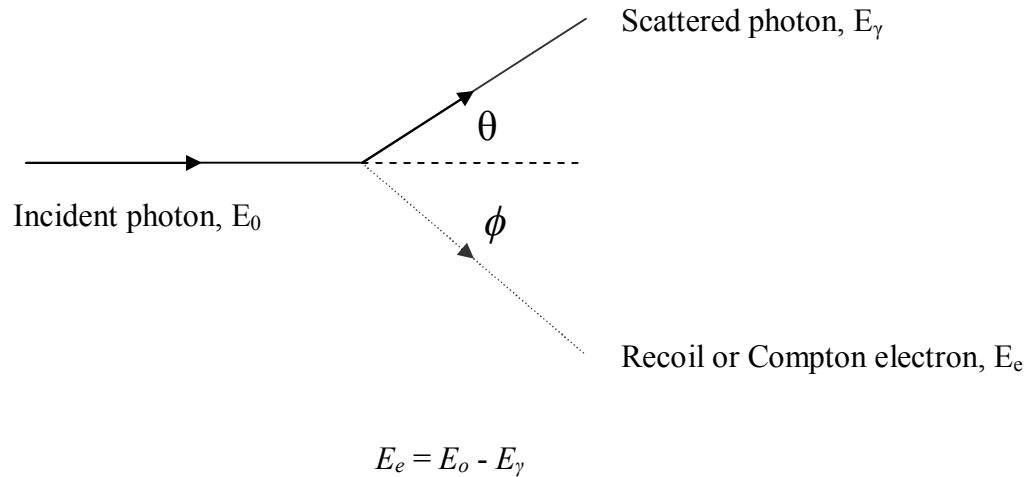


Figure 2.4. Compton Scattering [27]; The energy and momentum of the incident photon are shared between the scattered photon and the recoiling electron.

$$\frac{E_\gamma}{E_0} \cong \frac{1}{1 - 2E(1 - \cos\theta)} \quad (2.3)$$

2.2.3 Electrons

Electron beam ionizing radiation involves the interaction of electrons with matter by several processes, including emission of ionizing radiation as well as elastic and inelastic collisions. The type interaction is determined mainly by the energy of incident electrons. Electrons produced by the UMCP LINAC have energy of 7 MeV which is lost primarily through inelastic collisions. As the primary electrons are slowed down, cascades of secondary, tertiary and consecutive electrons are produced. The electron energy loss by ionization and excitation is described in the following Bethe equation [27]:

$$-\left(\frac{dE}{dl}\right)_{col} = \frac{2\pi N e^4 Z}{m_e v^2} \left[\ln \frac{m_e v^2 E}{2I^2 (1-\beta^2)} - (2\sqrt{1-\beta^2} - 1 + \beta^2) \ln 2 + 1 - \beta^2 \right] + \frac{1}{8} (1 - \sqrt{1-\beta^2})^2 \quad \text{J m}^{-1} \quad (2.4)$$

where $(dE/dl)_{col}$ is specific energy loss or stopping power S , N is the number of atoms per unit volume, e is the charge on the electron, Z is the atomic number of the stopping material, m_e is the rest mass of the electron, v is the velocity of the electrons, β is v/c , c is the velocity of light, and I is the mean excitation potential for the atoms of the stopping material. The mass collision stopping power, $(S/\rho)_{col}$ is defined as follows:

$$\left(\frac{S}{\rho}\right)_{col} = -\left(\frac{dE}{dl}\right)_{col} \times \frac{1}{\rho} \quad (2.5)$$

where ρ is the density of material.

To calculate the maximum range of penetration of electrons produced by the UMCP LINAC, the following empirical equation may be used [32]:

$$R = 530 E - 106 \quad (2.6)$$

where R is electron range (mg cm^{-2}) and E is electron maximum energy (7 MeV for the UMCP LINAC). R is given as 3.6 g cm^{-2} for 7 MeV electrons, so by knowing solution density, the maximum range (cm) of the electrons in the solution can be calculated.

2.2.4 Radiation chemical yield

The radiation chemistry emphasizes the chemical changes induced by interactions of ionizing radiation with materials. The radiation chemical yield (G value) is defined as the moles of product produced or destroyed per joule of absorbed ionizing radiation energy (generally expressed as $\mu\text{mol J}^{-1}$ in SI units, or described as the number of molecules chemically changed per 100 eV of absorbed energy). The SI unit of absorbed dose is the gray (Gy) which is defined as the amount of the absorbed energy in joules per unit mass (kg) [27, 28]. The expression radiation chemical yield is as follows:

$$G(\mu\text{mol} / \text{J}) = \frac{C(\text{mol} / \text{L}) \times 10^6}{D(\text{Gy}) \times \rho(\text{kg} / \text{L})} \quad (2.7)$$

where C is the concentration of product formed or destroyed, D is the absorbed dose, and ρ is the bulk density. Most G values are typically less than $1 \mu\text{mol J}^{-1}$, whereas higher values generally indicate a chain reaction.

2.2.5 Radiation chemistry of aqueous systems

The interactions of the radiation with a material are distributed in proportion to the electron fraction of each component. Thus, in the case of a dilute solution of polymer, which is the interest in this work, primary reactive species are predominantly formed in the solvent (water) and then induce secondary chemical effects in minor solutes [27]. This is a good example of secondary effects which yield products by ionizing radiation. Direct effects predominate in systems where the reactive radicals cannot move freely (such as soils) or where a particular species comprises a larger mass fraction of the total matrix. In those cases, ionizing induced degradation usually occur. Direct effect normally produces primary products, such as a high energy electron and a consequent cation or interactions of the high energy electron as it is thermalized.

The radiation chemistry of water and aqueous solutions have been widely studied for their biological and ecological importance. Irradiation of such aqueous systems with γ -rays or high energy electrons (low LET) generates the following primary products: hydrated electrons (e_{aq}^-), hydrogen atoms (H), and hydroxyl radicals (\bullet OH). Electrons with thermal energies become hydrated (e_{aq}^-) as they are surrounded with polar water molecules within approximately 10^{-12} s. Charged particles (ions) also change into a hydrated form as ions are surrounded by shells of water molecules, with the electrostatic attraction between the ion and water dipoles holding them together [27]. The following Figure 2.4 represents the space-time development of a spur, transformation of intermediate species, and their diffusion driven expansion. In the water radiolysis products, species generated around 10^{-7} s

after deposition of energy are $\bullet\text{OH}$, e_{aq}^- , H , H_3O^+ , H_2O_2 and H_2 . Each product's radiation chemical yield (G value) are presented in the case of water at natural pH as follows [33]:

$$G(e_{\text{aq}}^-) = G(\bullet\text{OH}) = G(\text{H}_3\text{O}^+) = 0.28; G(\text{H}) = 0.062; G(\text{H}_2) = 0.047; G(\text{H}_2\text{O}_2) = 0.072 \quad (\mu\text{mol/J}) \quad (2.8)$$

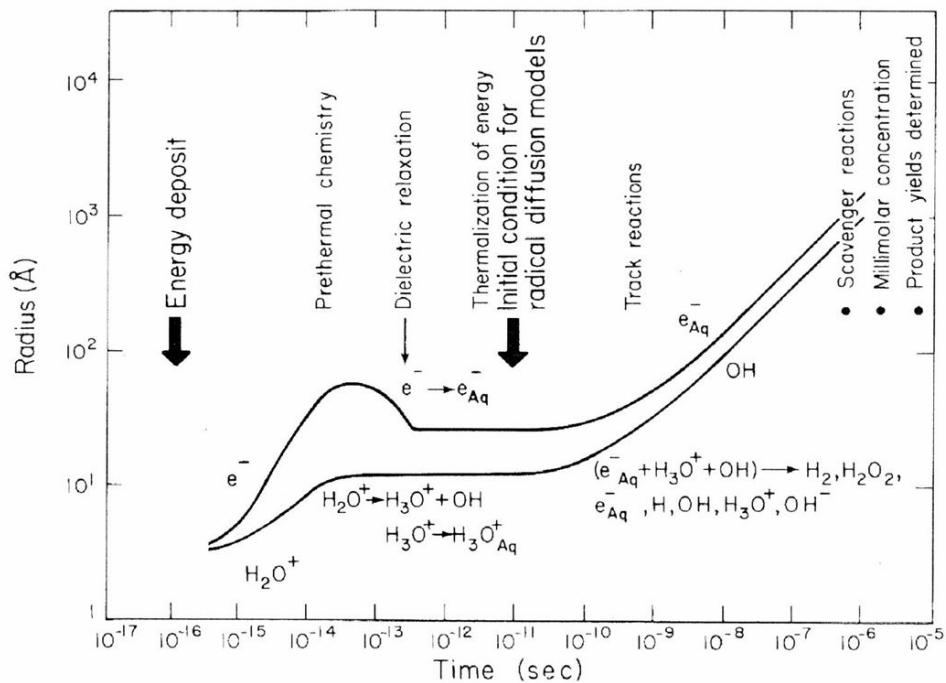


Figure 2.5. Space-Time development of a spur in a dilute, aqueous system [34].

The $\bullet\text{OH}$ are very reactive in oxidizing species. They add to unsaturated bonds (e.g., double bonds) with rate constants near the diffusion controlled limit and readily abstract H from the C-H bonds of macromolecular chains to yield carbon-centered radicals. Because the O-H binding energy in water is very high ($\Delta H(\text{H-OH}) = 495 \text{ kJ mol}^{-1}$), abstractions of carbon-bound H-atoms ($\Delta H(\text{C-H}) = 385 - 410 \text{ kJ mol}^{-1}$) are

always exothermic reactions. Due to this high reactivity, the H-abstraction by $\bullet\text{OH}$ is non-selective process [35]. H atoms can also contribute to this abstraction of H as follows:



where R represents alkyl or aryl group, $\text{R}\bullet$ represents each radical.

Besides H-abstraction, $\bullet\text{OH}$ can also be involved in addition to double bonds:



The $\bullet\text{OH}$ predominantly reacts with polarized double bonds at the electron-rich center [36] due to its electrophilicity [37].

The hydrated electron (e_{aq}^-), a localized electron surrounded by oriented water molecules, is a strong reducing agent. Its one-electron transfer reaction can be expressed as follows [38]:



where n is the charge on the solute S. It reacts preferentially with the vacant orbital of a system, and is highly reactive with organic molecules with low-lying vacant orbitals (such as most aromatics, carbonyl compounds, halides, disulfides, thiols, and nitro compounds). The e_{aq}^- reacts with oxygen to yield the superoxide radical ion ($\text{O}_2^{\bullet-}$) (reaction 2.12). The $\text{O}_2^{\bullet-}$ is then converted into $\text{HO}\bullet_2$ depending on the pH of the solute as is described in the following reaction 2.13. [30]



2.2.6 Reaction mechanism of e_{aq}^- and $\bullet OH$ with polymer

The aqueous polymer system of this work consists of water as a solvent and hydrophilic PVP as a solute. Water absorbs most of the ionizing radiation energy since the concentrations of PVP solutions studied in this work were very dilute (i.e., below overlap concentration) in most cases. The initial reactive species upon ionizing radiation are the $\bullet OH$, e_{aq}^- , and H atoms which are described in Chapter 2.2.5. The reaction mechanism of these species with PVP is represented in Figure 2.6 and 2.7. The e_{aq}^- reacts with carbonyl group of PVP to yield radical anions (A) and (B), followed by a rapid protonation of each transient ion.

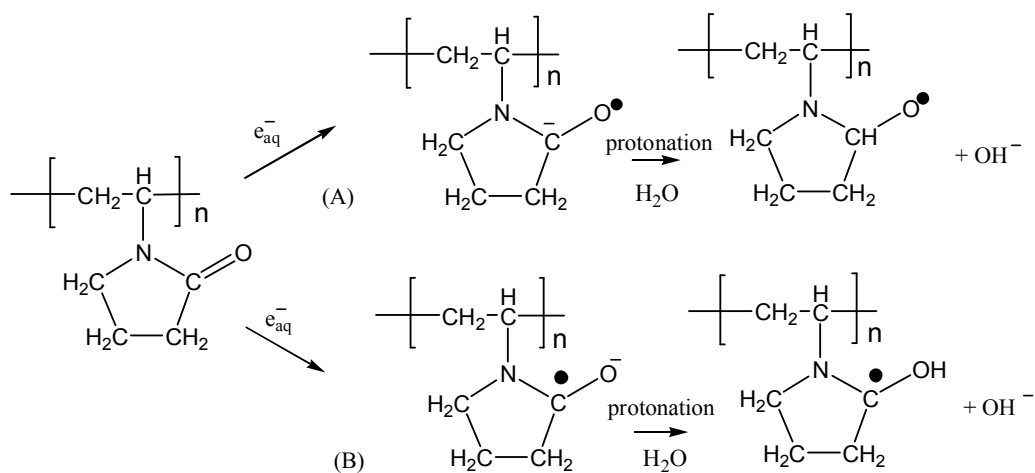


Figure 2.6. Reaction mechanisms of hydrated electrons with PVP.

In general, $\bullet OH$ reacts with polymer either by abstracting H or adding to a double bond [27]. Since PVP does not have unsaturated carbon within its structure, H abstraction is expected to occur at the carbon in the aliphatic polymeric backbone (Figure 2.7 (C)) as well as at the carbon in the pyrrolidone ring (Figure 2.7 (D)).

Both abstractions produce carbon-centered free radicals (PVP is shown as Zwitterion structure).

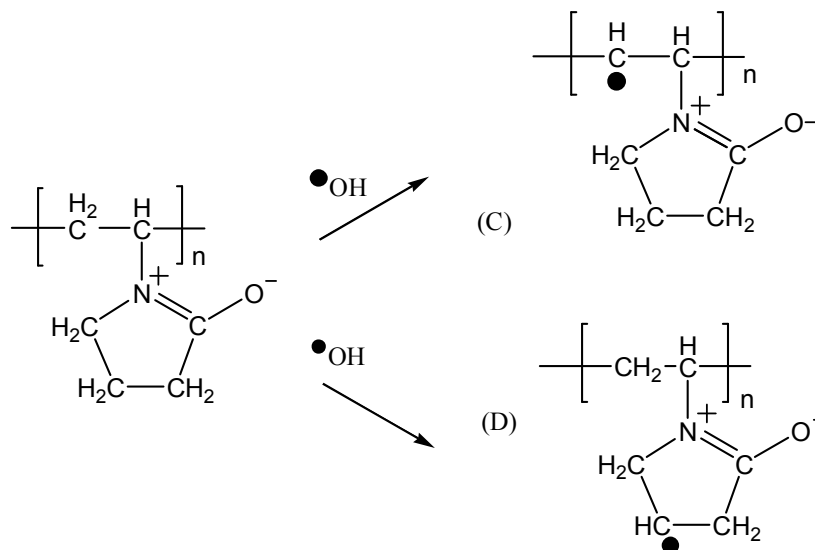
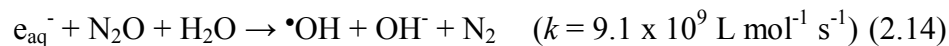


Figure 2.7. Reaction mechanisms of hydroxyl radicals with PVP.

In this study, $\bullet\text{OH}$ is the major species in the reaction with PVP, since e_{aq}^- is converted into $\bullet\text{OH}$ by nitrous oxide according to the following reaction [39]:



The yield of carbon-centered radicals is thereby increased. The H atoms have a much lower yield than that of hydroxyl radicals (ca. 10% of the hydroxyl radicals in N_2O -saturated solutions) and the rate constants of reaction with polymer chains are lower [17]. The PVP carbon-centered free radicals subsequently undergo one of these reactions: scission, hydrogen transfer, recombination, or disproportionation [17]. Major scission reactions only happen when the lifetime of polymer radicals are very

long, such as in poly(acrylic acid) [7]. Hydrogen transfer does not affect the polymer structure, but disproportionation is a competing reaction with crosslinking as is shown in Figure 2.8 and 2.9 [27].

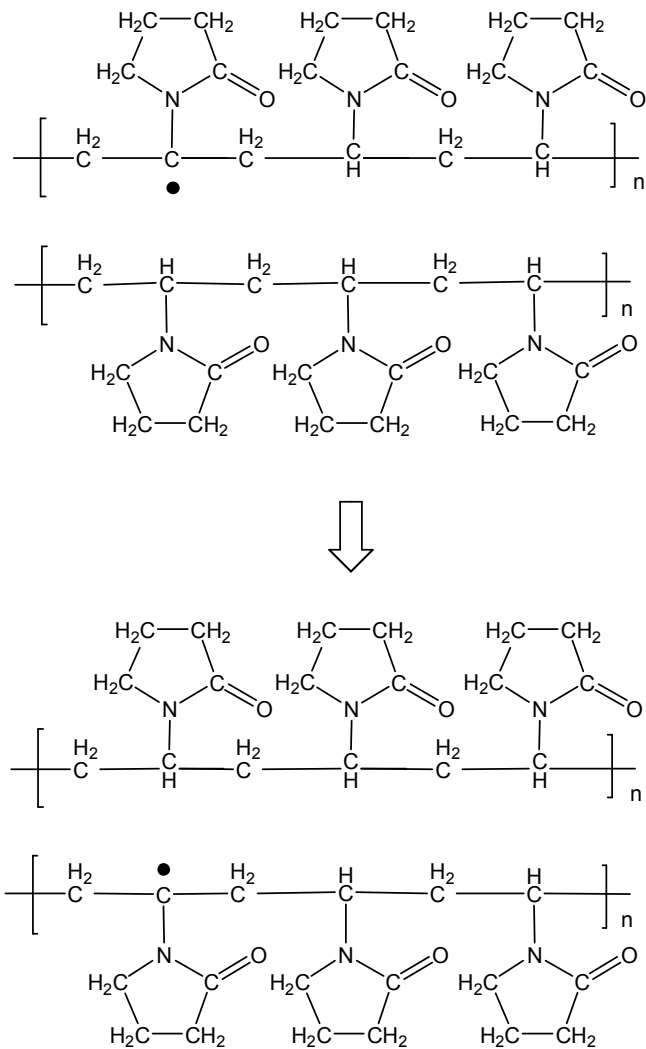


Figure 2.8. H transfer reaction mechanism of PVP carbon-centered free radicals.

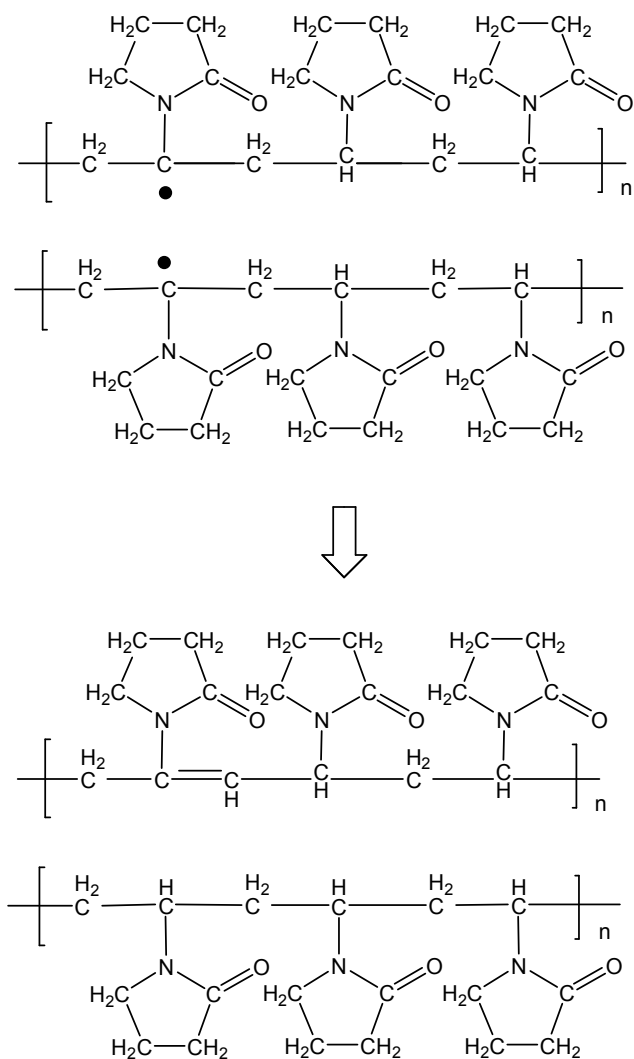


Figure 2.9. Disproportionation reaction mechanism of PVP carbon-centered free radicals.

The radical recombination reaction is the most important type of reaction for gel formation, and it can occur between adjacent polymer chains (inter-molecular crosslinking) or within single polymer chain (intra-molecular crosslinking). Figure 2.10 shows a schematic of the two types of crosslinking reactions. Inter-molecular (also called wall-to-wall) crosslinking is expected to increase the average size and molecular weight of starting polymer chains, whereas intra-molecular recombination retains the molecular weight with reduced dimension.

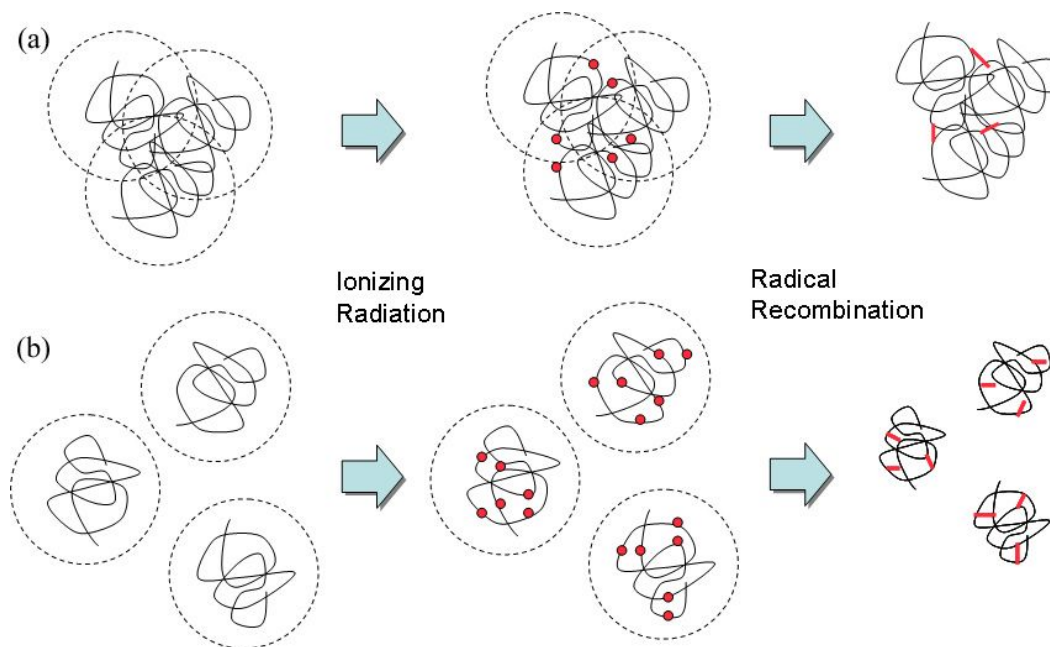


Figure 2.10. The crosslinking reaction schematics: inter-molecular (a), intra-molecular crosslinking (b).

If the concentration of polymer solution is high and the dose rate (Gy s^{-1}) is relatively low (e.g., γ -ray radiation), the number of radicals existing simultaneously on a single polymer chain is much less than one. This causes the probability of forming intra-molecular crosslinking bonds to be much less than that of inter-molecular crosslinks between adjacent chains. On the other hand, if the dose rate (Gy s^{-1}) and dose per pulse (Gy pulse^{-1}) are high (e.g., electron beam radiation at high pulse repetition rate), then multiple carbon-centered radicals can exist simultaneously within a single chain and form intra-molecular crosslinks. This occurs due to the higher probability of interaction between radicals on a single chain than that of different chains. The changes in size (R_h) and molecular weight of nanohydrogels synthesized at various processing conditions were measured by the asymmetric flow

field flow fractionation (AF4) chromatography.

2.3 Radiation facilities and dosimetries

2.3.1 Linear accelerator radiation facility

For the synthesis and the kinetic measurements of the nanohydrogels studied in this work, a fixed mount Varian[®] electron beam linear accelerator (LINAC) at the University of Maryland, College Park (UMCP) was used. Figure 2.11 shows a schematic of the major functional components of the UMCP LINAC. The actual equipment is shown in Figure 2.12. It consists of a pulse transformer, electron gun, gun housing (consisting of the gun steering, anode, and collimator), injection focus bending magnet coils, accelerator guide, power supply, vacuum pump, and current regulator chassis. Electron pulses are emitted from a heated filament into the cavity of the accelerator waveguide structure (about 1.5 m in length) with a 3 microsecond pulse width at a continuous variable repetition rate of up to 550 pulses per second at a pulse level of approximately 80 kV. The filament is made from barium aluminate (BaAl_2O_4), which is a thermionic material. When it is heated, electrons are boiled off and broken freely from the surface atoms. The emitted electrons are accelerated to the cathode by a 3 kV dc control potential, focused, and then passed through a collimating aperture. A thin lens magnet placed between the cathode and collimator provides the variation of injected current by causing change in the focal length and collimator beam diameter. In these experiments, electron beam energy is tuned to 7 MeV (tunable range of between 1 to 8 MeV) with a maximum beam current of 200 mA. Pulse repetition rate is varied from 20 to 300 pulses per second (Hz). Samples were prepared in 5 - 10 mL clear serum vials and sealed with the rubber septum and

aluminum caps and placed at a 10 – 15 cm distance from the electron emission port.

The dose per pulse was maintained within a range of 30 – 35 Gy for most of this work.

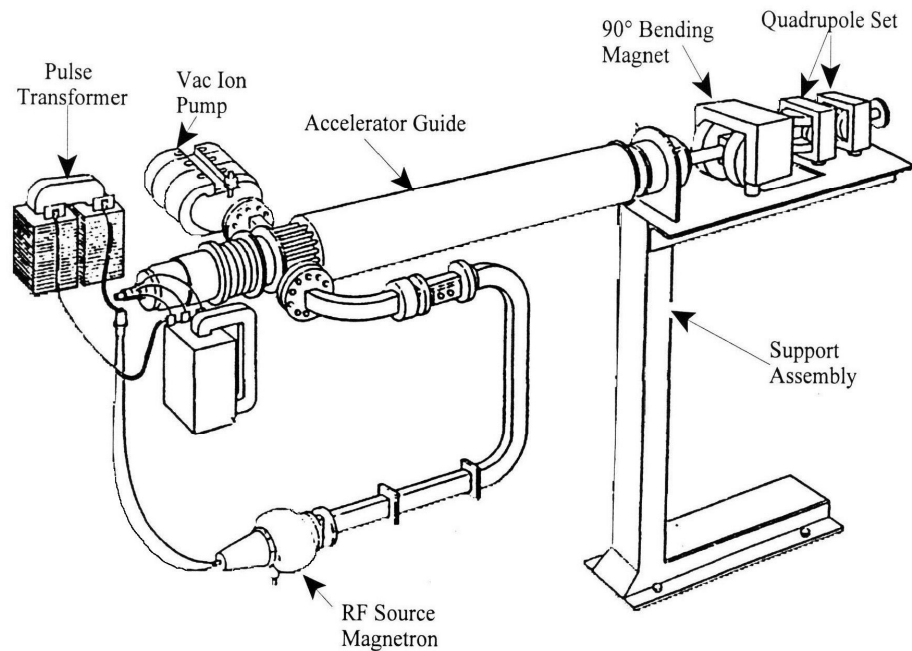


Figure 2.11. Schematic of major functional component of the UMCP LINAC (Magnetron and Vac Ion Pump shown reversed) [40].

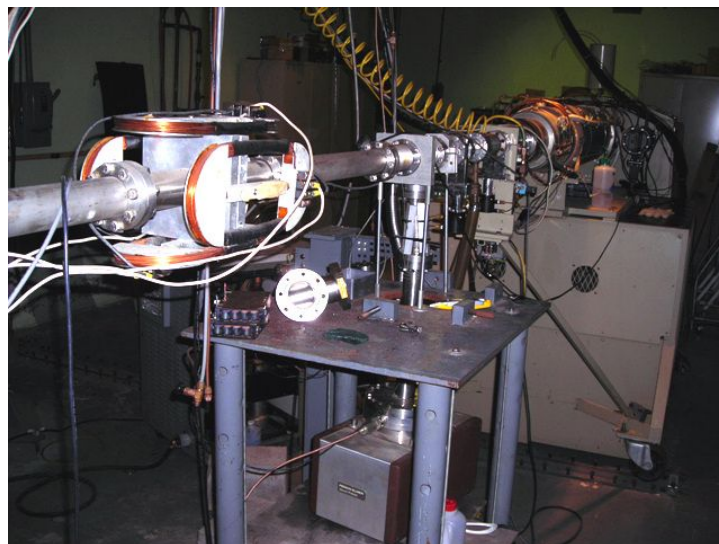


Figure 2.12. The UMCP LINAC facility

2.3.2 Gamma radiation facility

Another radiation source used for the synthesis of nanohydrogels is the ^{60}Co γ -ray radiation facility at the UMCP. The radiation cell houses ten Neutron Products, Model 200324 ^{60}Co source pencils (total activity was 8.25×10^{13} Bq (2230 curies) at the time of experiments) arranged in an annulus (Figure 2.13) that delivers dose rates of 3.5 kGy h^{-1} (equivalent to 0.972 Gy s^{-1}). The walls facing unrestricted areas are composed of 2307 kg m^{-3} concrete reinforced with steel bars and are from 1.2 to 1.5 m thick. Entrance to the vault is through an interlocked doorway which is closed during irradiations by a 0.5 m thick shielded steel door. The source is stored at the bottom of a water-filled stainless steel tank (1.2 m diameter by 4.3 m deep) which is enclosed in a sealed concrete cylinder when not in use. When it is being operated, the source is raised from the bottom of the pool to 0.76 m above floor level, where an aluminum lid is mounted on top of the pool tank (Figure 2. 14). For all γ -ray radiations performed in this work, up to four 5 mL glass vials are mounted on a polystyrene plate and inserted into a 7.6 cm internal diameter sample holder fitted to the aluminum lid which is mounted on the top of the pool tank.

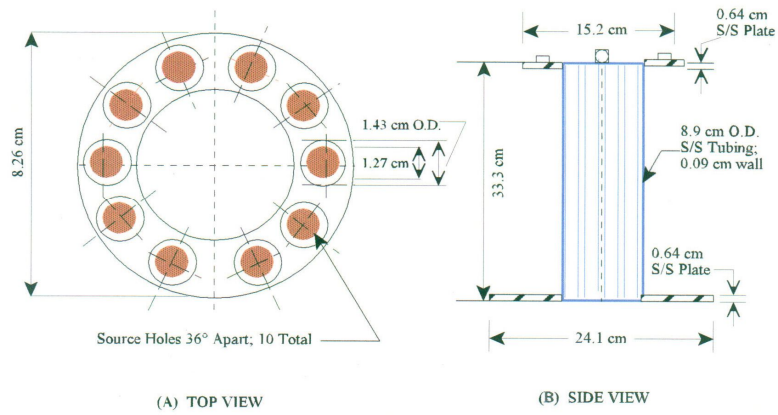


Figure 2.13. Schematic of the UMCP ^{60}Co Gamma sources & housing [40].



Figure 2.14. The UMCP ^{60}Co Gamma facility.

2.3.3 Dosimetry

To determine the dose deposited in the system, three types of dosimetry were used in this project: (1) Fricke solution [27], (2) potassium-thiocyanate solution [27], and (3) radiochromic film [27]. The spectrophotometer model used to measure the change in absorbance of these dosimeters upon irradiation is a Beckman™ DU Series 7000. The setup wavelength of the spectrophotometer measured was 605 nm for the radiochromic film and 304 nm for the Fricke solution.

2.3.3.1 Fricke dosimetry

In the most of the samples studied in this project, dilute aqueous polymeric solutions were irradiated with ionizing radiation sources to prepare nanohydrogels. An accurate estimation of the absorbed dose was obtained through the solution-based Fricke dosimeter. The absorbed dose is determined by chemical changes in the dosimeters which occur upon exposure to ionizing radiation. These chemical changes (e.g., production of specific ions upon radiolysis) lead to changes in the optical properties (e.g., absorbance at specific wavelength) of the dosimeters which can then be measured by the spectrophotometer. The Fricke dosimeter used in this work consisted of an air-saturated 10^{-3} M solution of ferrous sulfate in 0.4 M sulfuric acid. Reagent-grade chemicals [ferrous sulfate hydrate ($\text{FeSO}_4 \cdot 7\text{H}_2\text{O}$), sodium chloride (NaCl), and sulfuric acid (H_2SO_4)] used for Fricke dosimetry were purchased from J.T. Baker, Phillipsburg, NJ. and Fisher Chemical, Pittsburgh, PA.. As the Fricke solution is sensitive to trace quantities of organic impurities which can lead to higher $G[\text{Fe}^+]$ values and erroneously low absorbed dose, a 10^{-3} M sodium chloride solution

was added to suppress the oxidation of ferrous (Fe^{2+}) ions [27]. The initial yield of standard a Fricke dosimeter is independent of irradiation dose rate in the range of $0.2 - 2 \times 10^6 \text{ Gy s}^{-1}$ with added sodium chloride. But at higher dose rate above that range such as irradiations with UMCP LINAC, the amount of ferric ions (Fe^{3+}) formed decreases because the doses are great enough for radicals to react mutually rather than reacting with the solute [41]. The reduction of G-value as a function of dose rate is shown in Table 2.1.

Table 2.1. Yield of ferric ions in the electron irradiation of oxygen-containing solutions of ferrous sulfate in 0.4 M sulfuric acid.

kGy per 1.4 μsec pulse	G-value (number of molecules changed per 100 eV) in air saturated 10^{-3} M FeSO_4
0.01	15.2
0.02	14.9
0.04	14.5
0.08	13.7
0.16	12.6
0.64	9.1

Source: Adapted from [41].

The G-value used in these Fricke experiments was 14.9 (equivalent to $1.5442 \times 10^{-5} \text{ mol J}^{-1}$ in SI unit) based on the average dose rate of 7 MeV electrons from UMCP LINAC. The highest dose that an air-saturated solution can accurately measure is about 500 Gy; since dissolved oxygen becomes depleted beyond this dose [27].

The yield of Fe^{3+} from the oxidation of Fe^{2+} is given by [38]:

$$G[\text{Fe}^{3+}] = 2G[\text{H}_2\text{O}_2] + 3G[\text{H}^\bullet] + G[\bullet\text{OH}] \quad (2.15)$$

The number of Fe^{3+} ions produced in Fricke solution during irradiation was determined by the spectrophotometric measurement of absorbance changes at 304 nm. The molar concentration of Fe^{3+} ions is proportional to the oxidation of Fe^{2+} to Fe^{3+} ions.

The amount of absorbed dose can be calculated by following equation [27]:

$$D_F (\text{in Gy}) = \frac{\Delta A}{\varepsilon l \rho G[\text{Fe}^{3+}]} \quad (2.16)$$

where:

ΔA is the difference in absorbance (optical density) between the irradiated and the unirradiated solution at 304 nm

ε is the molar extinction coefficient for ferric (Fe^{3+}) ions at the wavelength of maximum absorption (304 nm), in $\text{L mol}^{-1} \text{cm}^{-1}$

l is the optical path length (sample thickness), in cm

ρ is the density of the dosimeter solution, in g cm^{-3}

$G[\text{Fe}^{3+}]$ is the yield of the reaction for the radiation in use, in mol J^{-1} .

The absorbed dose was measured by substituting $\varepsilon = 2174 \text{ L mol}^{-1} \text{cm}^{-1}$ (at 23.7°C), $l = 1.0 \text{ cm}$, $\rho = 1.024 \text{ kg L}^{-1}$, and $G[\text{Fe}^{3+}] = 1.5442 \times 10^{-6} \text{ mol J}^{-1}$ for 7 MeV electrons in equation [40].

The molar extinction coefficient of ferric ions in sulfuric acid (H_2SO_4) has a relatively large temperature coefficient increase of 0.7 percent per degree centigrade

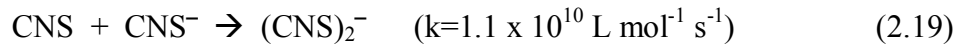
between 20 and 30 °C, so a correction for this effect is required by using following equation [27]:

$$\text{Absorbed Dose (corrected)} = \frac{\text{absorbed dose (measured at } t_2 \text{ °C)}}{1 + 0.007 (t_2 - t_1)} \quad (2.17)$$

where t_1 is the temperature (°C) where the extinction coefficient was determined and t_2 is the temperature (°C) where the absorbed dose is measured [40].

2.3.3.2 Potassium-Thiocyanate dosimetry.

The dosimetry required for pulse radiolysis studies is different from other types of dosimeters used in continuous radiation because of the short life time scale (in the order of 10^{-6} to 10^{-3} s) of the formed transient radicals and high absorbed dose rate (about 10^6 to 10^{10} Gy s^{-1}) used in this analysis technique [27]. The high dose rate irradiation yields high concentration of transient radicals and promotes the possibility of radical-radical reactions rather than radical-solute reactions. The change of absorbance of transient species is measured to calculate absorbed dose [27]. Upon irradiation of a potassium thiocyanate solution, the radiation-induced thiocyanate ions react with $\bullet\text{OH}$ radical as follows:



The absorbance of $(\text{CNS})_2^-$ dimer at 480 nm ($\epsilon_{480 \text{ nm}} = 7600 \text{ L mol}^{-1} \text{ cm}^{-1}$) and its disappearance by a second order reaction can be monitored by pulse radiolysis techniques.



2.2.3.3 Radiochromic film dosimetry

This solid-state dosimetry was mainly used to locate the electron beam centerline and map the dose distribution where the sample is positioned to verify the dose uniformity. The radiochromic dye (e.g., hexa(hydroxyethyl) aminotriphenylacetonitrile in this work) incorporated into the nylon film of the dosimeter undergoes chemical reaction upon ionizing radiation, creating and/or enhancing optical absorption bands. The radiochromic film, manufactured by Far West Technology (FWT) Inc., was used [42] and the absorbance changes upon irradiation were measured at 605 nm (i.e. centered peak wavelength for color change) using the spectrophotometer. The calibration curve of the film for this work is shown in Figure 2.15. The absorbance increases as irradiated dose increases and the absorbed dose is then calculated from this proportional relationship. The dose range can be accurately measured between 1 to 30 kGy, where the absorbance increases linearly with increasing dose.

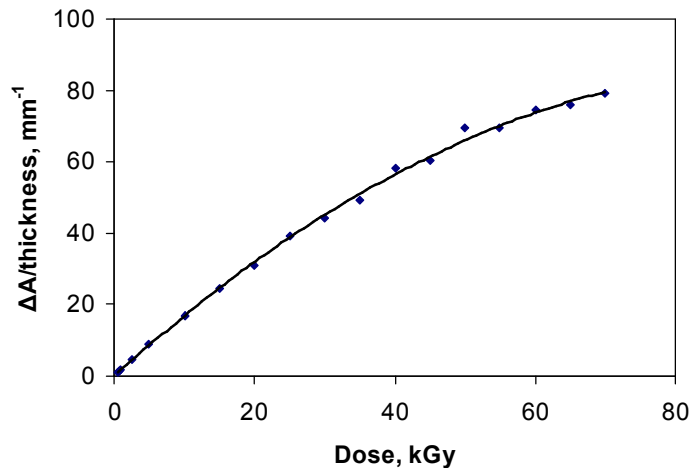


Figure 2.15. A calibration curve for the radiochromic film dosimetry in this work; The changes of the absorption of the Far West radiochromic films (Lot No. UM 35) at 605 nm were measured at the dose range of 0.5 to 70 kGy by the spectrophotometer.

2.4 Kinetic measurements (Pulse radiolysis)

Pulse radiolysis is the analytical technique where ionizing radiation-induced transient species are observed by a direct, in-situ detection method (e.g., conductimetry, optical spectroscopy, and electron spin resonance). This analysis gives informative insight into the mechanism of chemical reactions within microseconds (even picoseconds) induced by ionizing radiation. In this study, an optical spectroscopic method was used to study the fast reaction kinetics (e.g., rate constants, ionizing radiation yield, etc.) of various transients. The fine structure of absorption spectra can give in-depth information of the radiolysis reactions. Figure 2.16 shows a schematic diagram of this system.

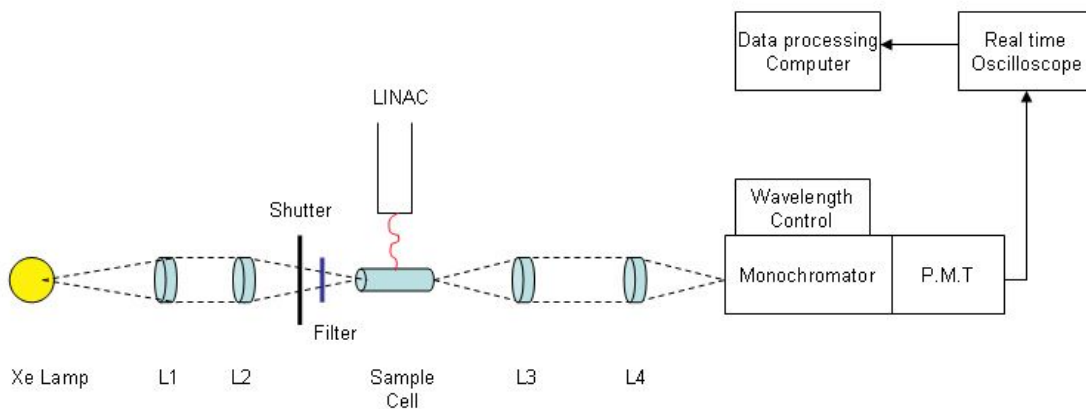


Figure 2.16. Schematic diagram of pulse radiolysis analysis system.

The system consists of a continuous light source (75W Xenon lamp, spectral distribution of 185 – 2000 nm, model L2174, Hamamatsu Corp.), focusing lenses, remote-controlled shutter, glass filter, Suprasil[®] glass sample cell, monochromator (model GM 252, Kratos Analytical), photoelectric detector (photomultiplier tube with

spectral response of 160 – 900 nm, model R955, Hamamatsu Corp.), and an oscilloscope (model Infiniium® 54820A, Agilent technology). The polymer aqueous solution under investigation is contained in an absorption sample cell and the time variation of transmission of sample at given wavelengths is measured by light beam intensities. Figure 2.17 shows the schematic signal profile (optical absorption change) from the photomultiplier

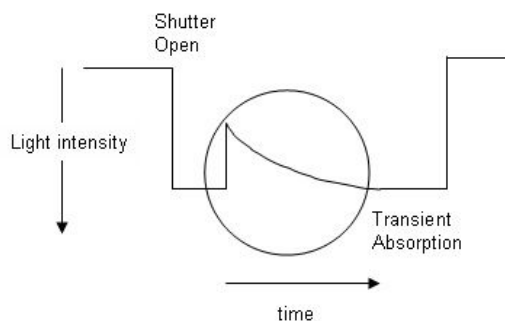


Figure 2.17. The photomultiplier signal profile.

Within a characteristic range of wavelengths, transients generated by radiolysis reactions can absorb the light and the changes in the absorbance of the sample can be observed as a function of time. From this information, the (pseudo) first- or second-order rate constant of free radical reactions and ionizing radiation yield can be calculated. The absorbance range of carbon-centered free radicals on PVP chains is expected within the 320 - 450 nm range with a maximum at approximately 390 nm [43]. The absorbance is calculated as the logarithm of the ratio of intensities before and at different times after the electron pulse according to Beer's Law:

$$A = \varepsilon \times b \times c \quad (2.21)$$

$$A = -\log_{10} T = -\log_{10} \left(\frac{I}{I_0} \right) \quad (2.22)$$

$$c = G \times D, \quad \varepsilon = \frac{\Delta A}{G D l} \quad (2.23)$$

where A is absorbance, ε is molar extinction coefficient ($\text{L mol}^{-1} \text{cm}^{-1}$), b is optical cell path length (cm), c is the sample concentration (mol L^{-1}), T is transmittance, I is intensity of light after traveling the sample, I_0 is original intensity of light from the source, ΔA is the absorbance difference, G is the G-value ($\mu\text{mol J}^{-1}$) of the sample, and D is dose ($\text{Gy} = \text{J kg}^{-1}$).

The absorbed dose from single electron pulse was measured by potassium-thiocyanate (KSCN) dosimetry (Chapter 2.3.3.2). The dose was determined from the maximum absorbance after 3 μs electron pulse using following formula.

$$D = \frac{\Delta A \times N_A}{\varepsilon_{480 \text{ nm}} \times G \times l} \quad (2.24)$$

where D is dose (Gy), ΔA is absorbance difference, N_A is Avogadro's number, $\varepsilon_{480 \text{ nm}}$ is molar absorption coefficient of $(\text{CNS})_2^-$ at 480 nm ($7600 \text{ L mol}^{-1} \text{cm}^{-1}$), G is G-value of $(\text{CNS})_2^-$ dimer formed upon ionizing radiation (2.9 molecules/100 eV, equivalent to $0.3 \mu\text{mol J}^{-1}$) and l is optical path length of the cell (1 cm). A typical second order decay profile of radiolytically formed $(\text{CNS})_2^-$ dimer at 480 nm is represented in Figure 2.18. The average dose was about 100 - 130 Gy pulse^{-1} in most pulse radiolysis experiments.

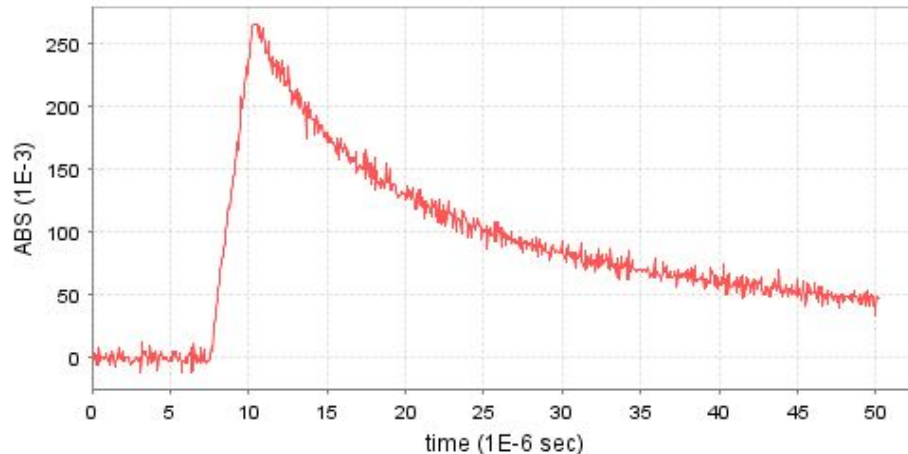
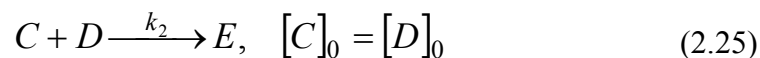


Figure 2.18. The typical bimolecular decay of the $(\text{CNS})_2^-$ monitored at 480 nm in air-saturated solution.

For quantitative kinetic studies, conditions are usually selected for the system such that a given elementary reaction will predominate as completely as possible [44]. In this work, the second order reaction between carbon-centered PVP radicals is important to understand the crosslinking reactions which form hydrogel structures.

The bimolecular reaction between same transients can be represented as follows:



where C and D are reactants, E is a product, k_2 is a second order reaction rate constant ($\text{L mol}^{-1} \text{s}^{-1}$), $[C]$ and $[D]$ are the concentration of reactant C and D (mol L^{-1}), $[C]_0$ and $[D]_0$ are the initial concentration of reactant C and D (mol L^{-1}).

The rate expression corresponding to Eq. (2.25) is given by:

$$\frac{-d[C]}{dt} = k_2[C]^2 \quad (2.26)$$

which integrates to

$$\frac{1}{[C]_t} - \frac{1}{[C]_0} = k_2 t \quad (2.27)$$

C is identical with D so that the reaction is C + C, reaction rate constant k_2 is replaced by $2 k_2$ in equations (2.26) to (2.29).

$$\frac{C}{C_0} = \frac{1}{1 + C_0 k_2 t} \quad (2.28)$$

$$\frac{A}{A_0} = \frac{1}{1 + \frac{A_0}{\epsilon l} k_2 t} \quad (2.29)$$

where t is time, A is absorbance, A_0 is absorbance when t (time, sec) = 0, ϵ is molar extinction coefficient ($\text{L mol}^{-1} \text{cm}^{-1}$), l is optical cell path length (cm). The second reaction rate constant $2 k_2$ can be calculated from the slope of the following $1/A$ vs. t , second order curve fitted plot.

2.5 Characterization techniques

2.5.1 Dynamic light scattering (DLS)

Temperature-controlled dynamic light scattering (DLS) equipment at the Institute for Physical Science and Technology at the UMCP was used to investigate the temperature effects on the size and chain diffusivity of the PVP samples. DLS, also known as photon correlation spectroscopy (PCS) and quasi-elastic light scattering (QELS), can probe structural relaxations and dynamics. This method determines the translational diffusion coefficient (D or D_0) and hydrodynamic radius (R_h) by measuring time-dependent fluctuations in the scattering intensity at a particular angle θ [45-47]. Fluctuations in the scattering intensity are correlated to give an intensity autocorrelation function $g(\tau)$ as a function of the correlation (delay) time τ . The autocorrelator averages the product of two scattered light intensities $I(t)$ and $I(t + \tau)$ measured at different time. $I(t)$ is converted to $\langle I(t)I(t + \tau) \rangle$ by the autocorrelator. The correlation function $g(\tau)$ is defined as follows.

$$g(\tau) = \lim_{T_A \rightarrow \infty} \frac{1}{T_A} \int_0^{T_A} I(t)I(t + \tau) dt = \langle I(t)I(t + \tau) \rangle \quad (2.30)$$

It shows that $I(t)I(t + \tau)$ is averaged over long period T_A to give what is known as the ensemble average: average over all possible configurations of the molecules in the solution. If the system is in equilibrium, the ensemble average is constant with time, such that $\langle I(t)I(t + \tau) \rangle = \langle I(0)I(\tau) \rangle$.

The scattering intensity $I(t)$ fluctuates around an average $\langle I \rangle$, so that $I(t)$ can also be described in terms of a fluctuating component $\Delta I(t)$ as:

$$I(t) = \langle I \rangle + \Delta I(t) \quad (2.31)$$

Since by definition $\langle \Delta I(t) \rangle = 0$, the autocorrelation function can be represented as:

$$g(\tau) = \langle I(t)I(t+\tau) \rangle = \langle I \rangle^2 + \langle \Delta I(t) \Delta I(t+\tau) \rangle \quad (2.32)$$

This can then be divided by $\langle I \rangle^2$ to give:

$$\begin{aligned} \langle I(t)I(t+\tau) \rangle / \langle I \rangle^2 &= 1 + \langle \Delta I(t) \Delta I(t+\tau) \rangle / \langle I \rangle^2 \\ &= 1 + f_c g_2(\tau) \end{aligned} \quad (2.33)$$

where f_c is a coherence factor that depends on the instrument geometry, which is defined by:

$$f_c \equiv \langle \Delta I^2 \rangle / \langle I \rangle^2 \quad (2.34)$$

$g_2(\tau)$ is the normalized intensity autocorrelation function, which is defined as:

$$g_2(\tau) \equiv \langle \Delta I(t) \Delta I(t+\tau) \rangle / \langle I \rangle^2 \quad (2.35)$$

The measured scattering intensity autocorrelation function $g_2(\tau)$ can be converted into the autocorrelation function $g_1(\tau)$ of electric-field $E_s(t)$ through the Siegler relation.

$$g_2(\tau) \equiv |g_1(\tau)|^2 \quad (2.36)$$

$$g_1(\tau) \equiv \frac{\langle E_s^*(t) \cdot E_s(t+\tau) \rangle}{\langle E_s^*(t) \cdot E_s(t) \rangle} \quad (2.37)$$

where $E_s(t)$ is the electric field at time t , and $*$ indicates the complex conjugate. If the scattering species is a dilute monodisperse spherical particle, then the electric-field correlation function forms a single exponential decay of time (τ), which is given by:

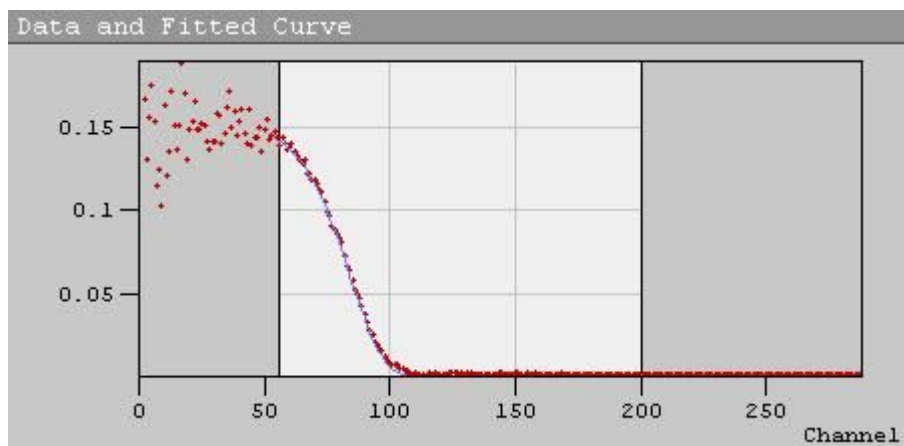
$$g_1(\tau) = \exp(-Dq^2 \tau) \quad (2.38)$$

where D is the translational diffusion coefficient of the particle and q is the wave vector. The hydrodynamic radius (R_h) can then be calculated using the Stokes-Einstein relationship:

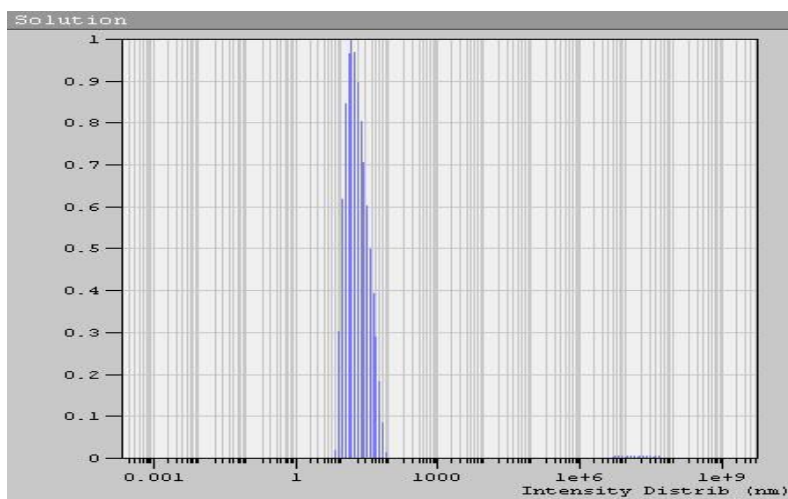
$$R_h = \frac{k_B T}{6\pi\eta D} \quad (2.39)$$

where k_B is the Boltzmann constant, T is the absolute temperature, and η is the viscosity of the solvent.

The translational diffusion coefficient D and hydrodynamic radius R_h of the unirradiated PVP was measured by DLS (Photocor Complex system, Photocor Instrument) at various temperatures. All collected data were processed and statistically analyzed by Dynals v2.0 software (Alango software co.). A general correlation function and corresponding R_h distribution analysis for the unirradiated PVP is represented in Figure 2.19. The schematic and photo of the DLS apparatus are shown in Figure 2.20 and 2.21.

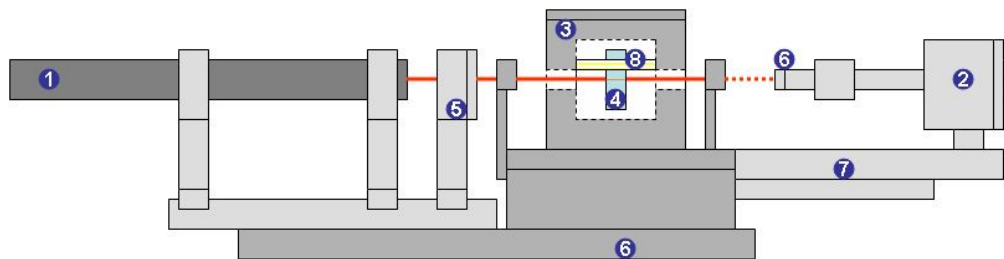


(a)



(b)

Figure 2.19. General correlation function plot (a) and corresponding R_h distribution analysis (b) from the DLS measurement of unirradiated PVP aqueous solution ($c = 9 \times 10^{-2} \text{ mol L}^{-1}$) at 25°C .



1. He-Ne Laser generator, 2. Photon counting system,
 3. Thermostat, 4. Sample, 5. Focusing optics,
 6. Optical bench base, 7. Rotating arm of turn table
 8. Sample cell holder

Figure 2.20. Schematic of DLS apparatus at the UMCP.

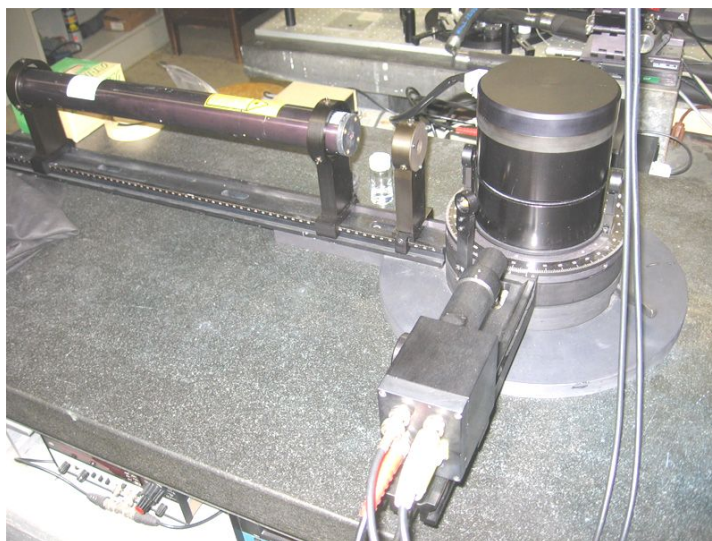


Figure 2.21. DLS apparatus: Photocor Complex system.

2.5.2 Asymmetric flow field flow fractionation (AFFFF)

chromatography

Asymmetric flow field flow fractionation (AFFFF) chromatography equipment at the National Institute of Standards and Technology (NIST) was used to determine the size and molecular weight of the irradiated PVP samples (nanohydrogels). AFFFF chromatography, also called asymmetric forced field fractionation (AFFF) chromatography, is a single-phase liquid chromatography technique in which high-resolution separation takes place in a field force applied laminar flow [48]. This technique does not require any column media, so the process is rapid and non-destructive without a stationary phase which may interact with or alter the sample. The range of separation used in this method is 0.001 – 50 μm [49] and the particle size distribution can be attained in various sample systems, such as polymers [50, 51], proteins [52], and viruses [53]. Within the flow channel, a parabolic laminar flow profile is created initially and the analytes are driven towards the boundary layer of the channel as a perpendicular force field is applied. Diffusion by Brownian motion generates a counteraction motion [54]. Smaller particles with higher diffusivity reach an equilibrium position higher up in the channel, where the longitudinal flow rate is higher and are transported more rapidly along the channel [54]. However, larger particles with lower diffusivity are positioned lower in the channel and move more slowly along it. Particles of different size can be separated by this velocity gradient flowing inside the channel [55]. Smaller particles elute earlier than larger ones, which is the opposite of Gel Permeation Chromatography (GPC) separation in which the larger molecules elute first [56].

The separation process is executed in three steps [54]: injection, focusing, and Elution. During the first two steps, the main input flow is split, introduced to the channel from both ends, and balanced to meet under the injection port. The flow which moves down and permeates through the membrane is then focused in a thin band and permeates through the membrane. After transfer of the sample, the injection flow is stopped and the flow pattern is switched to the elution mode. The separated sample is eluted from the outlet and then transported to an array of detectors to be analyzed. A schematic of AFFFF is shown in following Figure 2.22.

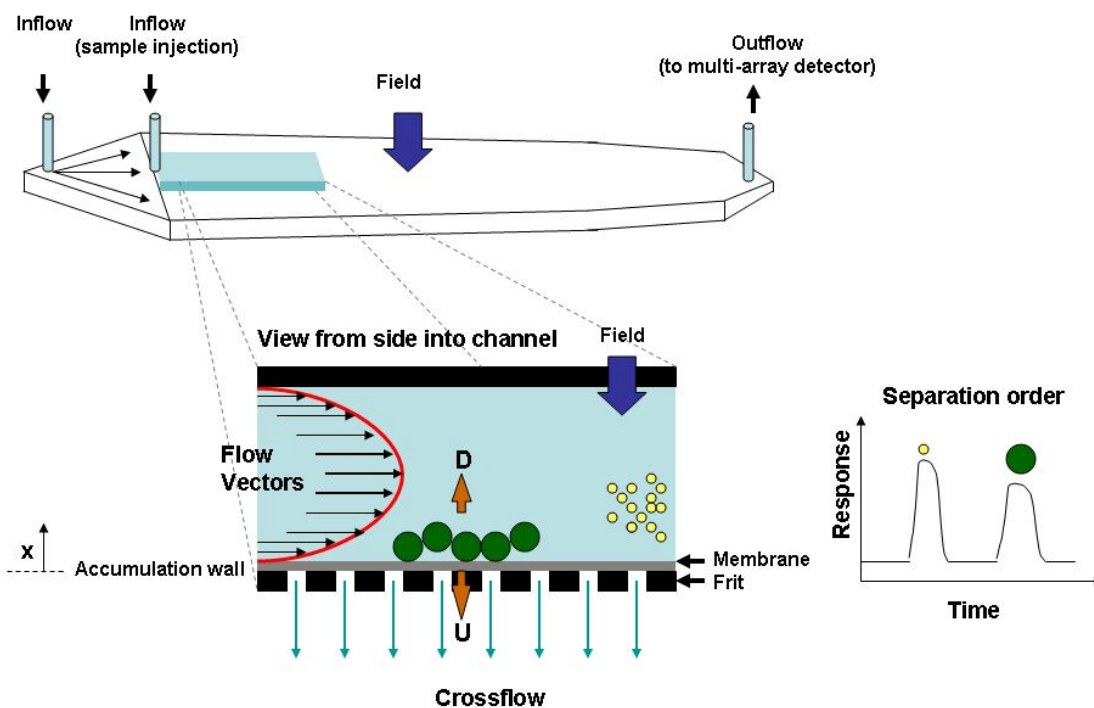


Figure 2.22. Schematic of separation mechanism of AFFFF chromatography.

A retention equation is used to describe the concentration distribution (i.e., height of the molecule over the accumulation wall) and parabolic flow profile (i.e., flow rate of the carrier at specific height over the accumulation wall).

The concentration distribution is a function of down speed U and up speed D , and is described as follows [48]:

$$c(x) = c_0 e^{-\frac{xU}{D}} = c_0 e^{-\frac{x}{L}} \quad \text{with} \quad L = \frac{D}{U} \quad (2.40)$$

where c is the concentration of the solute, c_0 is the concentration at height zero, x is the distance to the accumulation wall, U is the drift velocity, D is the diffusion coefficient, and L is the mean layer thickness.

The mean layer thickness L of the solute over the accumulation wall is established by the equilibrium between the drift velocity U and diffusivity D . The drift velocity U is defined as the force F on the solute divided by the friction coefficient f : $U = F/f$. The friction coefficient is described by the Nernst-Einstein equation: $f = kT/D$, where k is Boltzmann's constant and T is temperature. If the species have different mean thickness layers L over the accumulation wall, then separation will take place.

The parabolic flow profile in the transportation stream can be modeled by following equation with the assumptions of: (1) velocity = 0 at the accumulation wall ($x = 0$), (2) constant flow profile along the separation axis [48].

$$v(x) = 6 \cdot \langle v \rangle \cdot \left(\frac{x}{w} - \frac{x^2}{w^2} \right) \quad (2.41)$$

where v is the flow velocity of the carrier liquid, $\langle v \rangle$ is the average velocity of the carrier liquid, x is the distance to the accumulation wall, and w is the channel thickness.

The retention parameter R is defined as the average velocity of a particular species with respect to the average carrier $\langle v \rangle$ velocity. The average velocity V is the sum of the product of all the different flow rates in the channel and the corresponding sample concentration $c(x) \cdot v(x)$ divided by the sum of all concentrations $c(x)$.

$$R = \frac{V}{\langle v \rangle} = \frac{t_0}{t_r} = \frac{V_0}{V_r} = \frac{\langle c(x) \cdot v(x) \rangle}{\langle c(x) \rangle \langle v \rangle} \quad (2.42)$$

From the above three equations, the retention parameter R can be expressed as follows [55]:

$$R = 6 \cdot \lambda \cdot \left[\coth\left(\frac{1}{2 \cdot \lambda}\right) - 2 \cdot \lambda \right] \quad (2.43)$$

$$\lambda = \frac{L}{w} = \frac{1}{w} \cdot \frac{D}{U} = \frac{1}{w} \cdot \frac{k_B T}{F} \quad (2.44)$$

where λ is the dimensionless cloud thickness or reduced layer thickness, L is the mean layer thickness, w is the channel thickness, U is the drift velocity, D is the diffusion coefficient, T is the temperature, k_B is the Boltzmann's Constant, and F is the force acting on solute.

In the flow FFF, solutes are transported against the accumulation wall with velocity U by the cross flow stream V_x . The velocity U can be expressed as follows:

$$\dot{U} = \frac{\dot{V}_x}{A} = \frac{\dot{V}_x \cdot w}{V_0} \quad (2.45)$$

where \dot{V}_x is the volumetric cross flow rate, A is the surface area of the accumulation wall, V_0 is the channel volume, and w is the channel thickness.

The force F acting on the solute is defined as below [54]:

$$F = \frac{\dot{V}_x \cdot w}{V_0} \cdot f \quad (2.46)$$

The retention parameter R for asymmetrical flow FFF is described by following equation:

$$R = \frac{t_0}{t_r} \approx 6\lambda \quad \text{with} \quad \lambda = \frac{k_B \cdot T}{w \cdot F} \quad (2.47)$$

where t_0 is the void time, t_r is the retention time, λ is the reduced layer thickness, w is the channel thickness, T is the temperature, k_B is the Boltzmann's Constant, and F is the force acting on solute.

The hydrodynamic radius R_h is calculated from Stokes-Einstein relationship and the diffusion coefficient D in this experiment is calculated from retention equation as follows [57]:

$$R_h = \frac{k_B \cdot T}{6 \cdot \pi \cdot \eta \cdot D} \quad (2.48)$$

$$D = \frac{t_0 \cdot w^2 \cdot \dot{V}_x}{6 \cdot t_r \cdot V_0} \quad (2.49)$$

In these experiments, the particle size (R_h) distribution and molar mass (g mol^{-1}) of PVP nanohydrogels was measured by AFFFF chromatography (Eclipse separation system with DAWN EOS, Wyatt Technology) with auxiliary spectroscopy (LINEAR

UVIS 204, Linear Instruments) for the detection of UV absorbance of the PVP samples at 225 nm. The equipment setup is shown in Figure 2.23. The molar mass (g mol^{-1}) distribution was determined from the scattered light signal and the corresponding UV absorbance peak. The molar extinction coefficient of PVP at 225 nm was measured as $1.0 \times 10^3 \text{ mL g}^{-1} \text{ cm}^{-1}$ (Figure 2.24) by UV-VIS spectrophotometer (Lambda 900, Perkin Elmer) at the NIST.

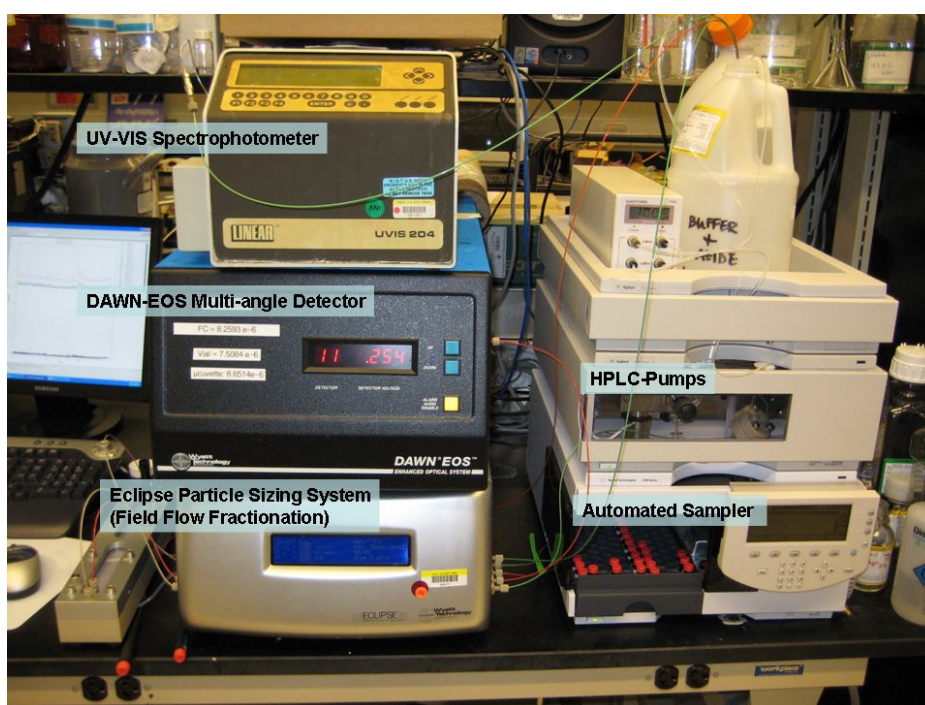


Figure 2.23. AFFF equipments for the measurements of R_h and molar mass.

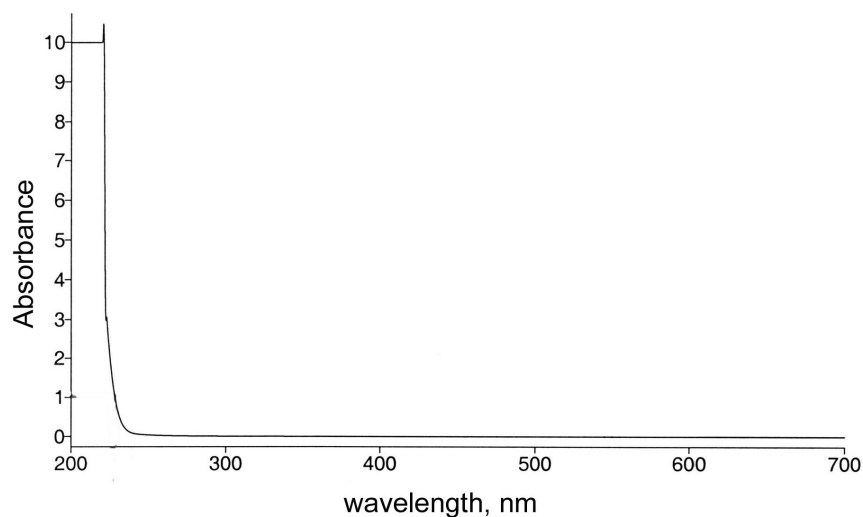


Figure 2.24. UV-VIS absorbance spectra of PVP aqueous solution.

2.5.3 Atomic force microscopy (AFM)

AFM is a powerful nanoscopic analytical tool which gives information regarding the surface morphology and phase through the production of a 3D map of the sample surface with high resolution (i.e., 1×10^{-10} m) [58]. Sample preparation is relatively simple compared to the other conventional electron microscopy techniques, in which staining or coating of sample is required [59]. A schematic of AFM operation is shown in Figure 2.25. A cantilever with a very fine-pointed tip which is mounted perpendicular to the longitudinal direction of the cantilever is placed on the sample. A laser is reflected from the back of the cantilever into a position sensitive quadrant photodiode sensor which records any deflections of the cantilever induced by Van der Waals force between the tip and the sample [60]. These signals are further processed to give the topographical information of the surface.

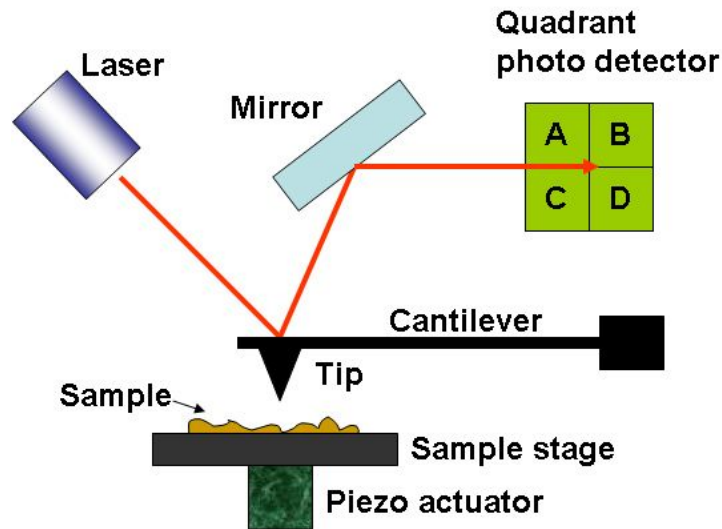


Figure 2.25. Schematic of atomic force microscope.

In this work, the visualization of the nanohydrogels is performed by a Digital Instruments Inc., Nanoscope II, with the anisotropically shaped silicon tip in tapping mode. The cantilever oscillates with a specific resonant frequency by a small piezoelectric actuator mounted in the AFM tip in this mode. The oscillation amplitude of cantilever is reduced as the tip gets closer to the sample surface. The electronic servo adjusts the height of the cantilever above the sample to maintain the oscillation amplitude while the cantilever scans over the sample. For the topographic analysis of the PVP sample surface, a film was prepared by casting a solution of the sample onto a freshly cleaved mica (1×1 inch) substrate with consecutive drying.

2.5.4 Environmental scanning electron microscopy (ESEM)

The size and shape the nanohydrogels synthesized by template-assisted ionizing radiation was observed using a Philips E-3 environmental scanning electron

microscope (ESEM). ESEM can be operated under controlled environmental conditions [61], and can be employed at relatively higher pressures (50 Torr) and higher temperatures (1500 °C) than those of conventional SEM. Non-conducting specimens (e.g., polymers in general) can be analyzed without surface charging because of the design of the secondary electron detector which uses the gas ionization to amplify the secondary electron signal. The positive ions which are generated are attached to the nonconductive sample surface as charge accumulates from the electron beam and the ions effectively suppress charging artifacts by charge neutralization [61].

Chapter 3:

RADIATION-INDUCED SYNTHESIS OF NANOHYDROGELS

3.1 Introduction and previous works

This chapter is dedicated to the studies of the nonionic polymer nanohydrogels synthesized from poly(vinyl pyrrolidone) (PVP) aqueous solutions by pulsed electron beam and steady-state γ -ray radiolysis. PVP is a biocompatible hydrophilic material which has been extensively applied in pharmaceuticals, biomedical sciences, food, cosmetics, etc [62]. However, previous researches on PVP hydrogels using ionizing radiation have focused on the synthesis of macroscopic (inter-molecularly crosslinked) gel systems [63-65]. The synthesis mechanism of intra-molecularly crosslinked PVP nanohydrogel with high energy electron beam was proposed rather recently and showed a decrease in the radius of gyration (R_g) while maintaining the weight averaged molecular weight (M_w) of the irradiated PVP (Figure 3.1) [17]. This result represents a pure intra-molecularly crosslinked PVP structure.

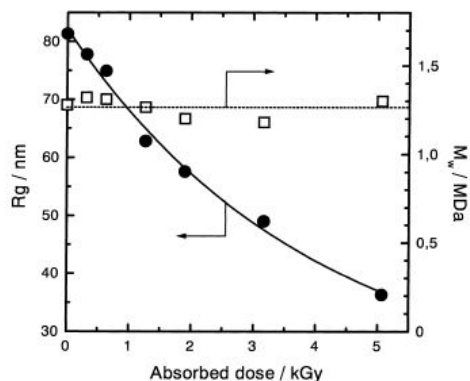


Figure 3.1. Properties of PVP in aqueous solution as a function of an average absorbed dose; M_w of PVP = $1.3 \times 10^6 \text{ g mol}^{-1}$, dose/pulse = 0.32 kGy, pulse frequency = 0.5 Hz, pulse duration (width) = $2 \mu\text{s}$ [17].

However, the effects of dynamic properties (e.g., translational diffusion) or chain conformation of PVP in aqueous solution on the inter-molecular crosslinking reaction were not considered. A combination of intra- and inter-molecular crosslinking reactions may take place even in dilute polymer solutions (i.e., below overlap concentration). A study by Wang *et al.* [66, 67] reported the observation of branched polymer formation induced by inter-molecular crosslinking in the initial stages of ionizing radiation (Figure 3.2).

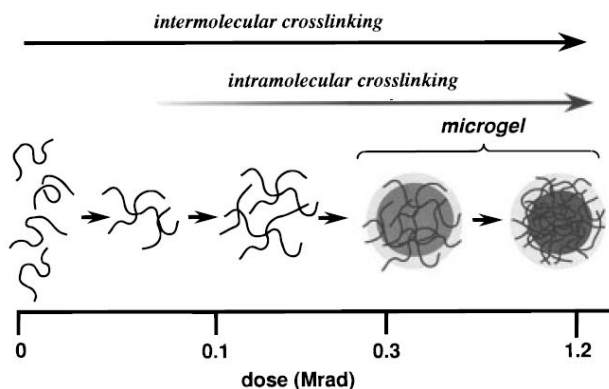


Figure 3.2. Schematic illustration of the formation process of PVA microgels during γ -ray irradiation [66].

In PVP aqueous solutions, temperature affects the translational diffusivity (D_t), which is described by the Einstein-Stokes formula: $D_t = k_B T / 6\pi\eta R_h$, where k_B is the Boltzmann constant, T is the absolute temperature, and η is the viscosity of the solvent (water). The inter-overlapping of the pervaded volume of PVP chains is expected to be governed by D_t and related to the inter-molecular crosslinking reaction.

The conformation of PVP chains in aqueous solution is sensitive to temperature. As temperature increases, polymer-water hydrogen bonds (e.g., between hydrogen atoms from water and the oxygen atoms of the carbonyl groups of PVP) are destroyed, thereby leading to collapsed chains with greater stiffness [68, 69]. This phenomenon can be understood by the following explanations [70]. In a binary mixture of polymer and solvent, each polymer chain is assumed to carry f identical functional groups which are able to form physical bonds with water molecules by pairwise association (i.e., hydrogen bond). A bonding-unbonding equilibrium is established by thermal activation, in which each polymer chain is associated with a certain number of water molecules. When m groups among f on a chain are bonded with water, it is known as m cluster. The free energy can be expressed as the sum of the two terms:

$$F = F_{rea} + \Delta F_{mix} \quad (3.1)$$

where F_{rea} is the free energy of the quasireference state where the clusters and the unbound free water are prepared separately. In terms of the chemical potential $\mu_{m+1,0}$ of a single isolated m cluster, F_{rea} is given by:

$$F_{rea} = N_0 \mu_{0,0} + \sum N_{m+1} \mu_{m+1,0} \quad (3.2)$$

where N_{m+1} is the number of m clusters and N_0 the unbound free water molecules. The second term ΔF_{mix} represents the free energy change needed in the mixing the thus constructed clusters with the free water molecules. According to the lattice theory of Flory-Huggins [71], the free energy ΔF_{mix} is expressed by:

$$\beta \Delta F_{mix} = N_t \left[\phi_0 \ln \phi_0 + \sum_{m=0}^f \frac{\phi_{m+1}}{n+m} \ln \phi_{m+1} + \chi \phi (1 - \phi) \right] \quad (3.3)$$

where ϕ_0 is the volume fraction of the free water molecules, ϕ_1 is the volume fraction of the unbound polymer, ϕ_{m+1} is the volume fraction of the m clusters, N_t is the total number of lattice cells in the system, n is the number of segments on a polymer, $\beta \equiv 1 / k_B T$, and χ is the solvent (water)-solute (polymer) interaction parameter which decreases with temperature increases [71]. The total volume fraction ϕ of the polymer is expressed by $\phi = \sum [n / (n+m)] \phi_{m+1}$. For a binary system, $\phi_0 + \sum \phi_{m+1} = 1$. When the system is in a thermal equilibrium state, each molecule is in chemical equilibrium through bonding and unbonding process. The volume fraction of m clusters ϕ_{m+1} can be expressed by $\phi_{m+1} = K_m \phi_1 \phi_{0,m}$, where K_m is an association constant given as $K_m = \exp(m - \Delta_m)$ in terms of the free energy difference Δ_m . K_m is a function of the $\lambda(T)$ as given by following equation [70]:

$$K_m = \frac{n+m}{n} \left[\frac{f!}{m!(f-m)!} \right] \lambda(T)^m \quad (3.4)$$

where $\lambda(T)$ is expressed by $\lambda(T) \equiv \lambda_0 \exp(\Delta \epsilon / k_B T)$ and $\Delta \epsilon$ is the energy required for a water-polymer bond formation. The average cluster size $\langle m \rangle$, also known as the average number of water molecules bonded on the polymer and is given by:

$$\langle m \rangle = \frac{\sum m N_{m+1}}{\sum N_{m+1}} = \frac{fx}{(1+x)} \quad (3.5)$$

where x is defined as $x \equiv \lambda \phi_o$.

These expressions show that x decreases and $\langle m \rangle$ decreases with increasing temperature. As the hydrogen bonds break at higher temperatures, water becomes less compatible solvent for the polymer [72].

Besides the changes in physical conformation with variation in temperature, PVP forms a unique chemical structure in water which is known as a Zwitterion [73]. The structure may influence the intra- and inter-molecular interactions between polar groups through electrostatic forces (Figure 3.3).

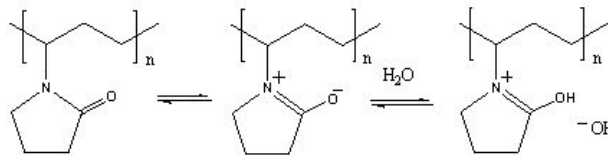


Figure 3.3. Keto-enol tautomerism in the pyrrolidone ring of PVP [73].

The Zwitterion structure and the temperature-dependent physical properties (e.g., chain conformation and diffusivity) of PVP are expected to determine the size and the molecular weight of the irradiated product through inter-molecular interactions. In this study, the radiation-induced intra- and inter-crosslinking mechanism of thermally collapsed and stiff PVP chains at high temperature are investigated and a novel synthesis method of PVP nanohydrogels is presented. Dilute PVP polymer aqueous solutions were prepared and irradiated by a tunable pulsed electron beam. The effects of the temperature, dose, and pulse repetition rate on the size and the molecular weight of the PVP products were examined.

3.2 Materials and sample preparations

PVP (Aldrich, $M_w = (3.94 \pm 0.12) \times 10^5 \text{ g mol}^{-1}$, determined by asymmetric flow field flow fractionation (AFFFF) chromatography) was used as received without further purification. Solutions of PVP were prepared by overnight stirring with 0.1 wt% (equivalent to $0.9 \times 10^{-2} \text{ mol}$ of monomer unit per liter) concentration followed by filtrations with $0.45 \mu\text{m}$ pore size syringe filter (MicroLiter analytical supplies, Inc.). The pH of the solutions were measured approximately 7 – 7.5. Water purified by Millipore Direct Q system having a specific resistivity of $18.2 \text{ M}\Omega$ and passed through a $0.2 \mu\text{m}$ pore size filter was used in all experiments. Each solution was transferred to a 5 mL glass serum vial and sealed with a rubber septum and an aluminum cap. N_2O gas was then used to convert e_{aq}^- to $\bullet\text{OH}$ as described in reaction (2.14). Dissolved oxygen is replaced by N_2O during the saturation process and doubles the concentration of $\bullet\text{OH}$ from radiolysis as described above.

The pulse repetition rate was varied from 20 to 300 pulses per second (Hz), and the range of total dose used was 5 to 10 kGy (1Gy is equivalent to 1 J kg^{-1}) in most experiments. A homogeneous dose distribution on the surface of the sample container was maintained by the beam mapping technique using FWT film dosimetry and the absorbed dose in the sample solutions was measured by Fricke dosimetry. For the dynamic light scattering measurements, all samples were passed through a $0.45 \mu\text{m}$ pore size syringe filter and put into a 20 mL clean glass vial prior to analysis.

3.3 Results

3.3.1 Processing parameter effects in electron beam irradiation

The collapses of the PVP molecules at high temperature.

The change in the average hydrodynamic radius (R_h) and the translational diffusion coefficient (D_t) of unirradiated PVP as a function of temperature is shown in Figure 3.4. The R_h of PVP is substantially constant within 20-50 °C temperature range, but decreased with further increases in temperature. At higher temperatures (above 50°C), the interactions between repeat units of the same polymer chain become more favorable due to the disruption of water-polymer hydrogen bonds, thereby leading to a more coiled or contracted conformation [68]. This effect can reduce the average distance of PVP radicals generated within a single chain and subsequently lead to the formation of more compact nanohydrogels which are crosslinked by intra-molecular radical recombination.

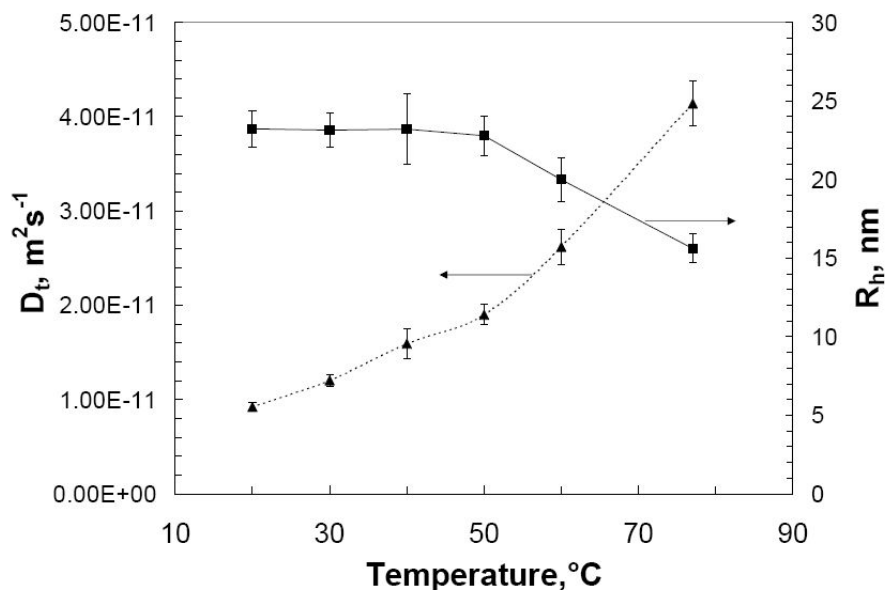


Figure 3.4. D_t and R_h of PVP polymer chains ($M_w = (3.94 \pm 0.12) \times 10^5 \text{ g mol}^{-1}$) as a function of temperature.

Nanogel formation by mixed intra- and inter-molecular crosslinking.

The weight averaged molecular weights (M_w) of the samples are shown in Table 3.1. The M_w of all of the samples increased after irradiation. The presence of inter-crosslinking reactions was identified by an increase in the M_w from $(3.94 \pm 0.12) \times 10^5$ to $(8.10 \pm 0.08) \times 10^5 \text{ g mol}^{-1}$ for the sample ($c = 0.9 \times 10^{-2} \text{ mol L}^{-1}$) irradiated even at high pulse repetition rate (300 Hz) and temperature (77 °C); 5 kGy as a total dose. The differential molar mass distribution curves of irradiated samples are shown in Figure 3.5 to 3.8. All irradiated samples show increased molecular mass due to the inter-molecular crosslinking reactions. In these figures, the samples synthesized at the highest temperature (77 °C) exhibited the lowest molar mass among the samples irradiated at the same dose and pulse repetition rate. The samples irradiated at high repetition rate (300 Hz) also displayed smaller molar masses than those of samples prepared at low repetition rate (20 Hz). Even when the concentration of the system (0.

$9 \times 10^{-2} \text{ mol L}^{-1}$) is below its overlap concentration (ca. $3 \times 10^{-2} \text{ mol L}^{-1}$), the inter-molecular crosslinking reaction is still present and contributes to the increased molecular weight of the product. However, when the concentration of sample was further reduced to 0.05 wt% ($0.45 \times 10^{-2} \text{ mol L}^{-1}$), the molecular weight of the irradiated samples became comparable to that of unirradiated PVP (Figure 3.8). The inter-molecular PVP radical-radical recombination reactions were suppressed at this low concentration.

Table 3.1. Weight averaged molecular weights (M_w , g mol^{-1}) of the PVP samples ($c = 0.9 \times 10^{-2} \text{ mol L}^{-1}$) synthesized at various temperatures.

Irradiation temperature ($^{\circ}\text{C}$)		20	60	77
Dose (kGy) / Pulse repetition rate (Hz)	0 / 0	$(3.94 \pm 0.12) \times 10^5$	-	-
	5 / 20	$(9.53 \pm 0.02) \times 10^6$	$(4.13 \pm 0.08) \times 10^6$	$(1.02 \pm 0.01) \times 10^6$
	5 / 300	$(8.81 \pm 0.18) \times 10^6$	$(3.06 \pm 0.06) \times 10^6$	$(8.10 \pm 0.08) \times 10^5$
	10 / 20	$(1.90 \pm 0.11) \times 10^7$	$(5.61 \pm 0.06) \times 10^6$	$(1.08 \pm 0.01) \times 10^6$
	10 / 300	$(9.54 \pm 0.02) \times 10^6$	$(4.47 \pm 0.18) \times 10^6$	$(9.90 \pm 0.10) \times 10^5$

Table 3.2. Weight averaged molecular weights (M_w , g mol^{-1}) of the PVP samples ($c = 0.45 \times 10^{-2} \text{ mol L}^{-1}$) synthesized at 77°C .

		M_w , g mol^{-1}
Dose (kGy) / Pulse repetition rate (Hz)	0 / 0	$(3.94 \pm 0.12) \times 10^5$
	5 / 20	$(5.18 \pm 0.10) \times 10^5$
	5 / 300	$(4.96 \pm 0.10) \times 10^5$
	10 / 20	$(6.49 \pm 0.13) \times 10^5$
	10 / 300	$(5.77 \pm 0.11) \times 10^5$

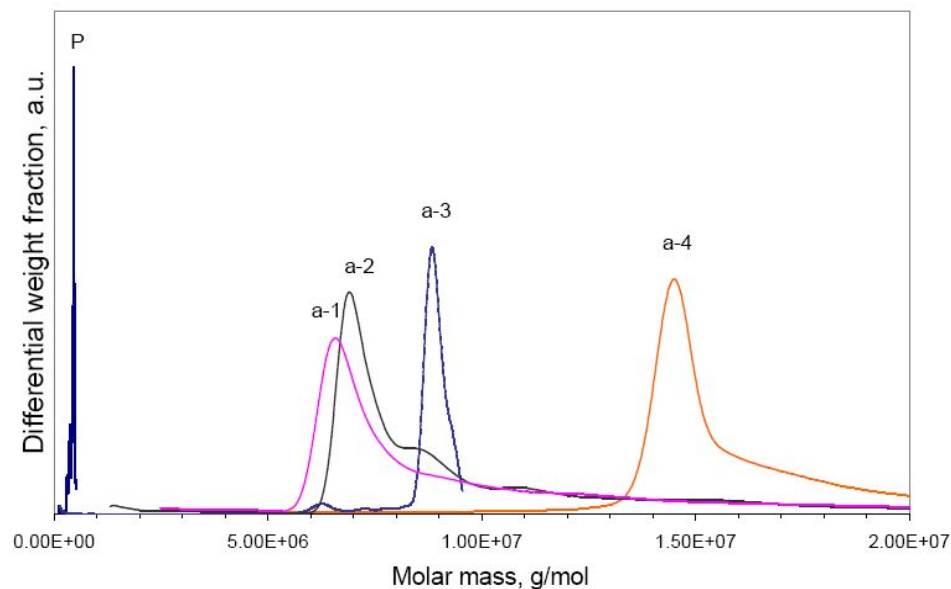


Figure 3.5. Differential molar mass distribution of the PVP samples ($c = 0.9 \times 10^{-2} \text{ mol L}^{-1}$) synthesized at $20 \text{ }^\circ\text{C}$ with the irradiation conditions: 5 kGy at 300 Hz (a-1), 5 kGy at 20 Hz (a-2), 10 kGy at 300 Hz (a-3), 10 kGy at 20 Hz (a-4). P is unirradiated PVP.

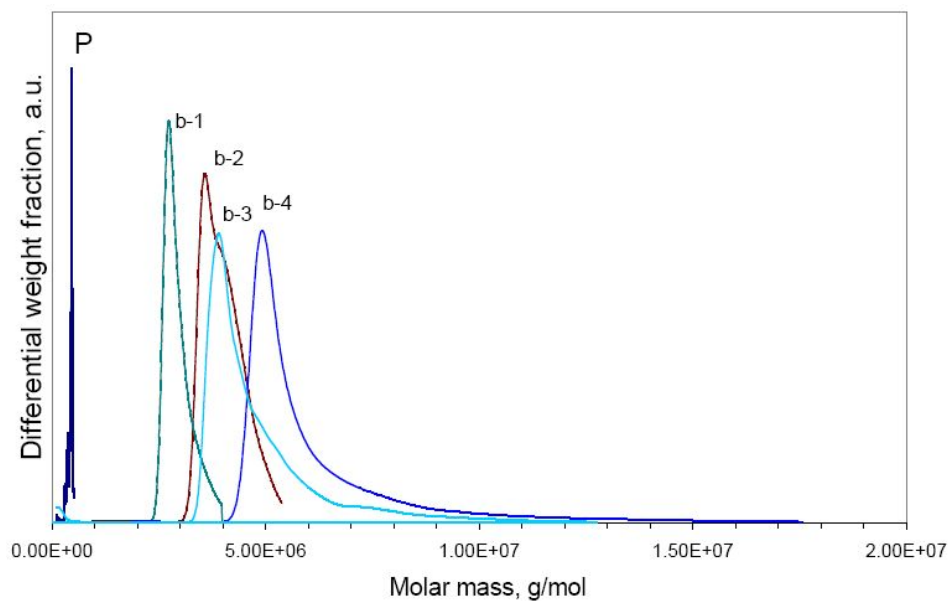


Figure 3.6. Differential molar mass distribution of the PVP samples ($c = 0.9 \times 10^{-2} \text{ mol L}^{-1}$) synthesized at $60 \text{ }^\circ\text{C}$ with the irradiation conditions: 5 kGy at 300 Hz (b-1), 5 kGy at 20 Hz (b-2), 10 kGy at 300 Hz (b-3), 10 kGy at 20 Hz (b-4). P is unirradiated PVP.

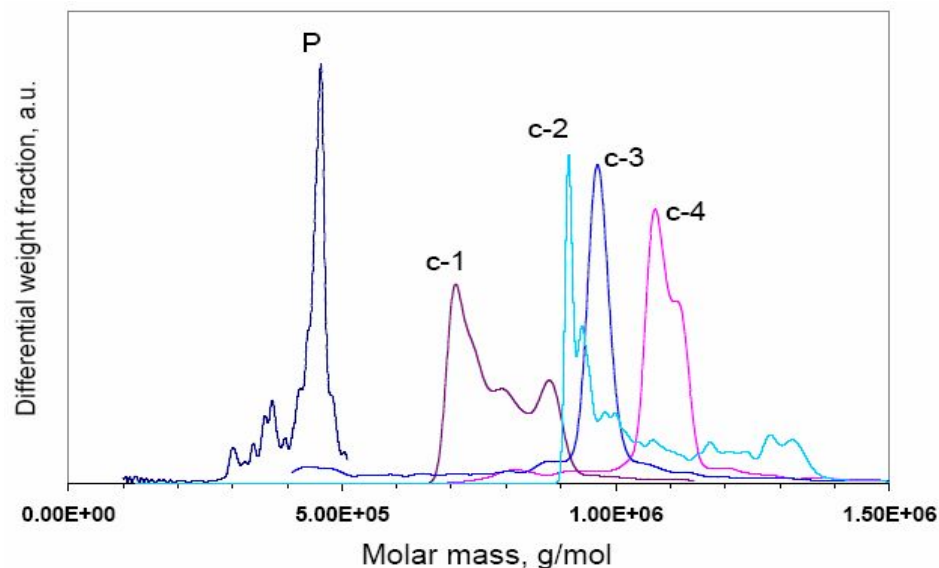


Figure 3.7. Differential molar mass distribution of the PVP samples ($c = 0.9 \times 10^{-2} \text{ mol L}^{-1}$) synthesized at $77 \text{ }^\circ\text{C}$ with the irradiation conditions: 5 kGy at 300 Hz (c-1), 5 kGy at 20 Hz (c-2), 10 kGy at 300 Hz (c-3), 10 kGy at 20 Hz (c-4). P is unirradiated PVP.

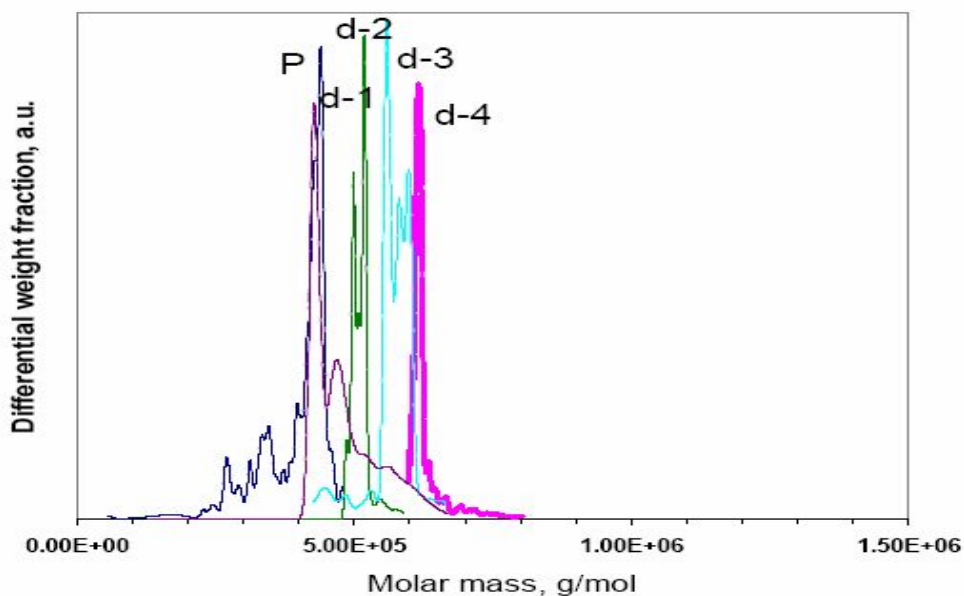


Figure 3.8. Differential molar mass distribution of the PVP samples ($c = 0.45 \times 10^{-2} \text{ mol L}^{-1}$) synthesized at $77 \text{ }^\circ\text{C}$ with the irradiation conditions: 5 kGy at 300 Hz (d-1), 5 kGy at 20 Hz (d-2), 10 kGy at 300 Hz (d-3), 10 kGy at 20 Hz (d-4). P is unirradiated PVP.

The number of inter-molecular crosslinks (c_x) formed in the irradiated product can be estimated in terms of the average molecular weight changes according to following equation [74]:

$$4c_x - c_s = 2c \left(\frac{1}{M_{w,0}} - \frac{1}{M_w} \right) \quad (3.6)$$

where c_x is the concentration of inter-molecular crosslinks (mol L^{-1}), c_s is the concentration of inter-molecular scission of the polymer bonds (mol L^{-1}), c is the concentration of the polymer solution (g L^{-1}), M_w is weight averaged molecular weight (g mol^{-1}) of irradiated polymer and subscript 0 denotes the initial weight of polymer before irradiation. Major scission reactions are only observed when the lifetime of polymer radicals is very long [7]. In this experiment, the carbon-centered polymer free radical half life is short (about $5 \mu\text{s}$ at $25 \text{ }^\circ\text{C}$ from the decay profile in Figure 4.6) and system is deoxygenated/saturated with N_2O . Therefore, the scission process in this work can be regarded as very minimal ($c_s \approx 0$) and Eq. (3.6) changes into Eq. (3.7) as follows:

$$c_x = \frac{c}{2} \left(\frac{1}{M_{w,0}} - \frac{1}{M_w} \right) \quad (3.7)$$

By converting c_x to radiation yield of crosslinking G_x (mol J^{-1}), Eq. (3.7) can be expressed as follows:

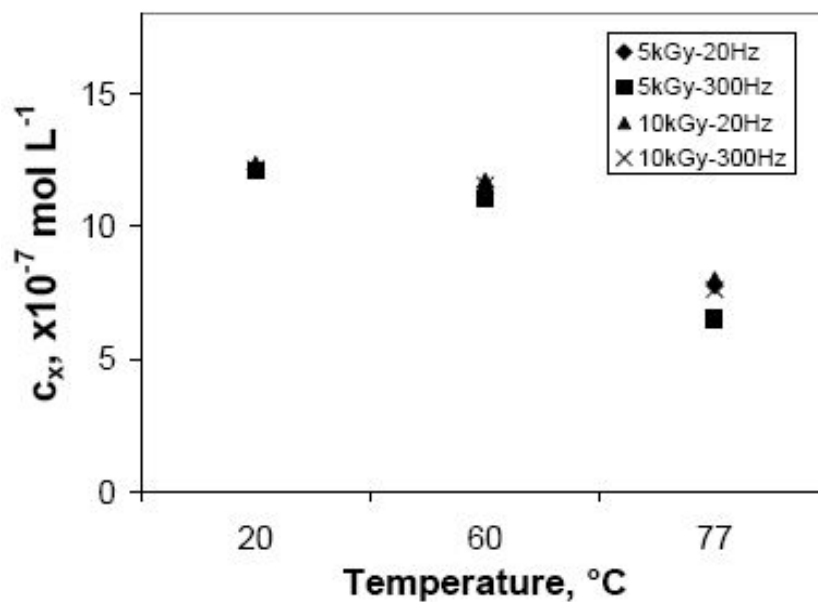
$$G_x = \frac{c}{2Dd} \left(\frac{1}{M_{w,0}} - \frac{1}{M_w} \right) \quad (3.8)$$

where D is the absorbed dose (Gy) and d is the solution density (kg L^{-1}).

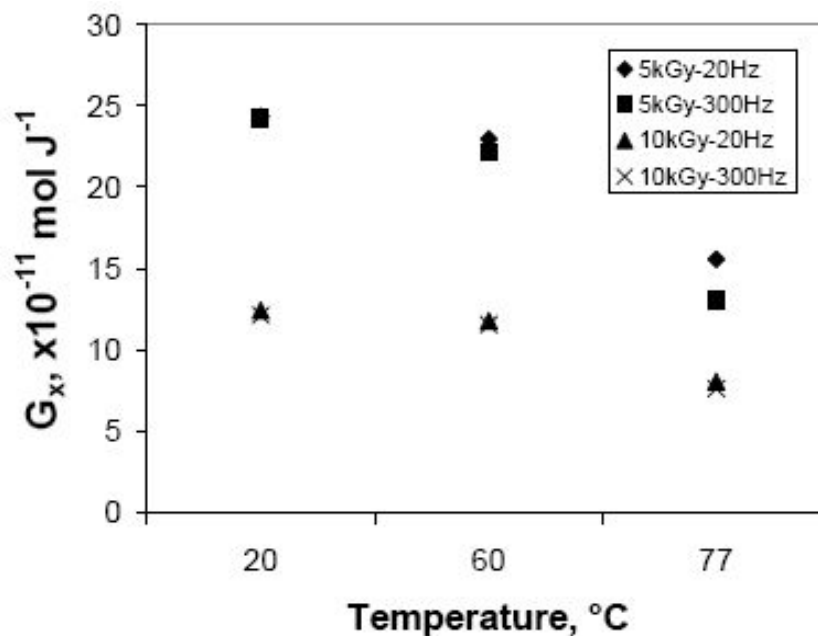
Figure 3.9 shows the changes in c_x and G_x as a function of temperature at different dose and pulse repetition rates. The c_x and G_x values decrease as temperature increases (Figure 3.9(a)) and clearly demonstrate the promotion of the intra-molecular crosslinking reaction. A high pulse repetition rate (300 Hz) is shown to be effective in reducing inter-molecular crosslinking reaction, particularly at the highest temperature (77 °C) employed. Table 3.3 compares the c_x and G_x of the PVP samples irradiated at 77 °C at two different concentrations (i.e., 0.45×10^{-2} and 0.9×10^{-2} mol L⁻¹). The number of inter-molecular crosslinking bonds in unit volume of sample is much less at 0.45×10^{-2} than that at 0.9×10^{-2} mol L⁻¹ thereby yielding lower molecular weight (Figure 3.7 and 3.8). This can be explained by a low radiation yield of inter-molecular crosslinking, G_x value as calculated in Table 3.3.

Table 3.3. Crosslinking parameters (c_x , G_x) of the synthesized PVP products at different concentrations; irradiation temperature = 77 °C.

		c_x ($\times 10^{-7}$ mol L ⁻¹)		G_x ($\times 10^{-11}$ mol J ⁻¹)	
Concentration (mol L ⁻¹)		0.0045	0.009	0.0045	0.009
Dose (kGy) / Pulse repetition rate (Hz)	5 / 20	1.52	7.79	3.04	15.58
	5 / 300	1.30	6.52	2.61	13.04
	10 / 20	2.49	8.06	2.49	8.06
	10 / 300	2.01	7.64	2.01	7.64



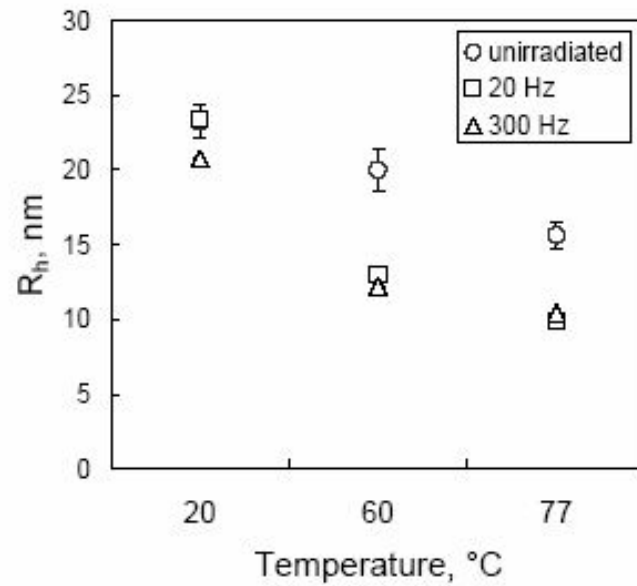
(a)



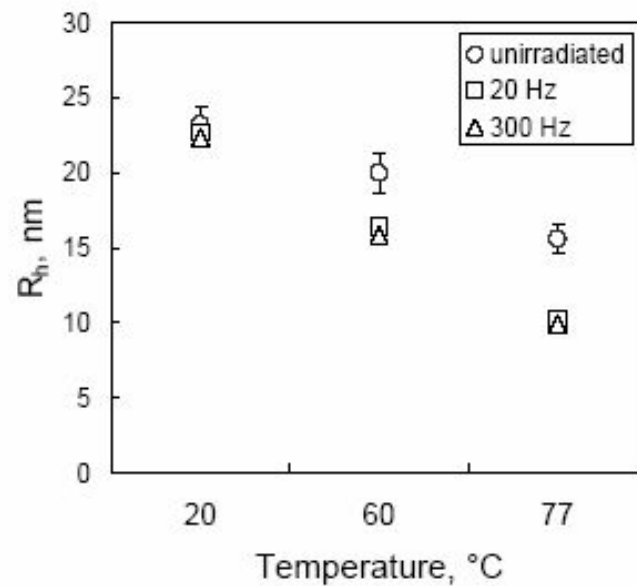
(b)

Figure 3.9. c_x (a) and G_x (b) of the synthesized PVP nanohydrogels ($c = 0.9 \times 10^{-2} \text{ mol L}^{-1}$) as a function of irradiation temperature at different doses and pulse repetition rates.

Figure 3.10 shows that nanohydrogels synthesized at higher temperature have smaller R_h compared to products formed at 20 °C under both dose conditions (5 and 10 kGy) investigated. The average R_h of PVP nanohydrogels synthesized at 77 °C with 300 Hz is 9.9 ± 0.1 nm (at 5 kGy) and 10.4 ± 0.1 nm (at 10 kGy). Samples synthesized at 20°C with same pulse repetition rate show a larger average R_h , 20.7 ± 0.2 and 22.3 ± 0.1 nm at 5 and 10 kGy respectively. Irradiation at a high pulse repetition rate (300 Hz) also contributes to reductions in the R_h of the synthesized products than at a low pulse repetition rate (20 Hz). The greater time-averaged number of $\bullet\text{OH}$ generated by water radiolysis at high pulse repetition rates can generate more carbon-centered free radicals on the same PVP chain than that of low pulse repetition rates since it increases the number of coexisting carbon-centered radicals in the same chain per unit time. This promotes intra-molecular radical-radical recombination rather than diffusion-driven inter-molecular radical reaction. For the more dilute system ($c = 0.45 \times 10^{-2} \text{ mol L}^{-1}$), the average R_h of the PVP nanohydrogels synthesized at 77 °C with 300 Hz is 8.9 ± 0.5 nm (at 5 kGy) and 7.6 ± 0.3 nm (at 10 kGy) (Figure 3.11). At a lower pulse repetition rate of 20 Hz, the measured average R_h is 9.3 ± 0.3 nm (at 5 kGy) and 8.3 ± 0.5 nm (at 10 kGy). The higher pulse repetition rate produces smaller R_h of samples at lower concentrations ($c = 0.45 \times 10^{-2} \text{ mol L}^{-1}$) than under more highly concentrated solutions ($c = 0.9 \times 10^{-2} \text{ mol L}^{-1}$). The R_h results show that lower concentrations lead to the formation of smaller dimensions of the nanohydrogels synthesized compared to those of higher concentration.

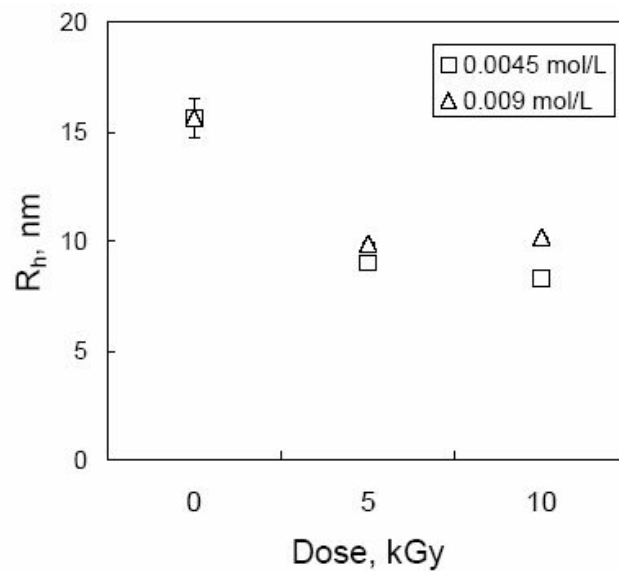


(a)

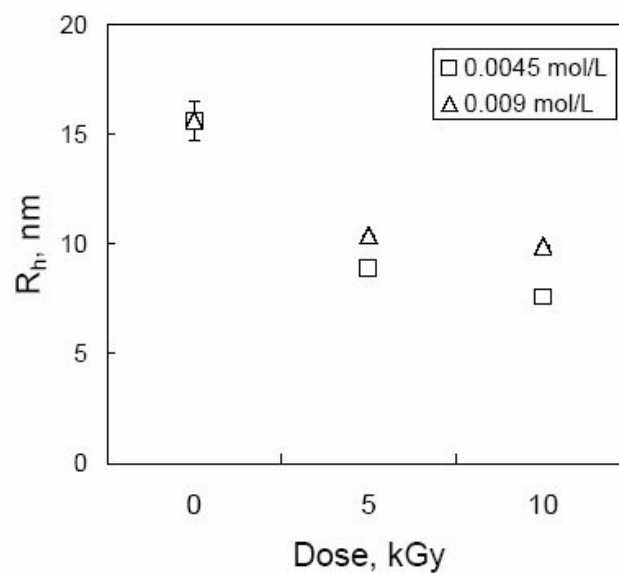


(b)

Figure 3.10. Change of R_h of the synthesized PVP nanohydrogels ($c = 0.9 \times 10^{-2} \text{ mol L}^{-1}$) as a function of irradiation temperature at different pulse repetition rates; 5 kGy (a) and 10 kGy (b) as used total dose.



(a)



(b)

Figure 3.11. R_h of the synthesized PVP nanohydrogels with different concentrations ($c = 0.9 \times 10^{-2}$ and $0.45 \times 10^{-2} \text{ mol L}^{-1}$) at identical irradiation temperature ($77 \text{ }^\circ\text{C}$); 20 Hz (a) and 300 Hz (b) as used pulse repetition rate.

3.3.2 Topographical observations of nanohydrogels by AFM

The surface morphology of the PVP nanohydrogels was characterized by AFM and compared by that of the linear polymer (unirradiated and non-crosslinked PVP). The scanned images of each PVP sample are shown in Figure 3.12. To investigate the real conformation of the polymer in water, AFM analysis under liquid environment is more appropriate to understand the sample's real physical conformation and shape as our group recently studied with short strands of DNA in a buffer solution (on a GaAs substrate) [75]. However, the PVP sample cast on mica tended to detach from the substrate in water due to the absence of stable covalent bonding between polymer and the substrate. For this reason, analysis was performed in the dry state instead. Linear PVP film samples were prepared by casting 5 wt% PVP aqueous solutions on freshly cleaved mica surfaces followed by overnight air-drying at ambient temperature. The following synthesizing conditions were applied for the PVP nanohydrogel samples: a total irradiation dose of 5 kGy, a pulse repetition rate of 300 Hz and an initial solution concentration of 0.1 wt% ($0.9 \times 10^{-2} \text{ mol L}^{-1}$). The same sample preparation steps were applied as were used for the linear PVP samples. The spherical contours of the nanohydrogels are distinctively observed on the surface of the film, while the linear PVP film shows a flat surface profile which was previously observed on poly(acrylic acid) nanohydrogels [76]. The actual PVP nanohydrogel conformation in water is expected to be much less agglomerated and less collapsed form due to the increased pervaded volume in good solvent (i.e., water for PVP).

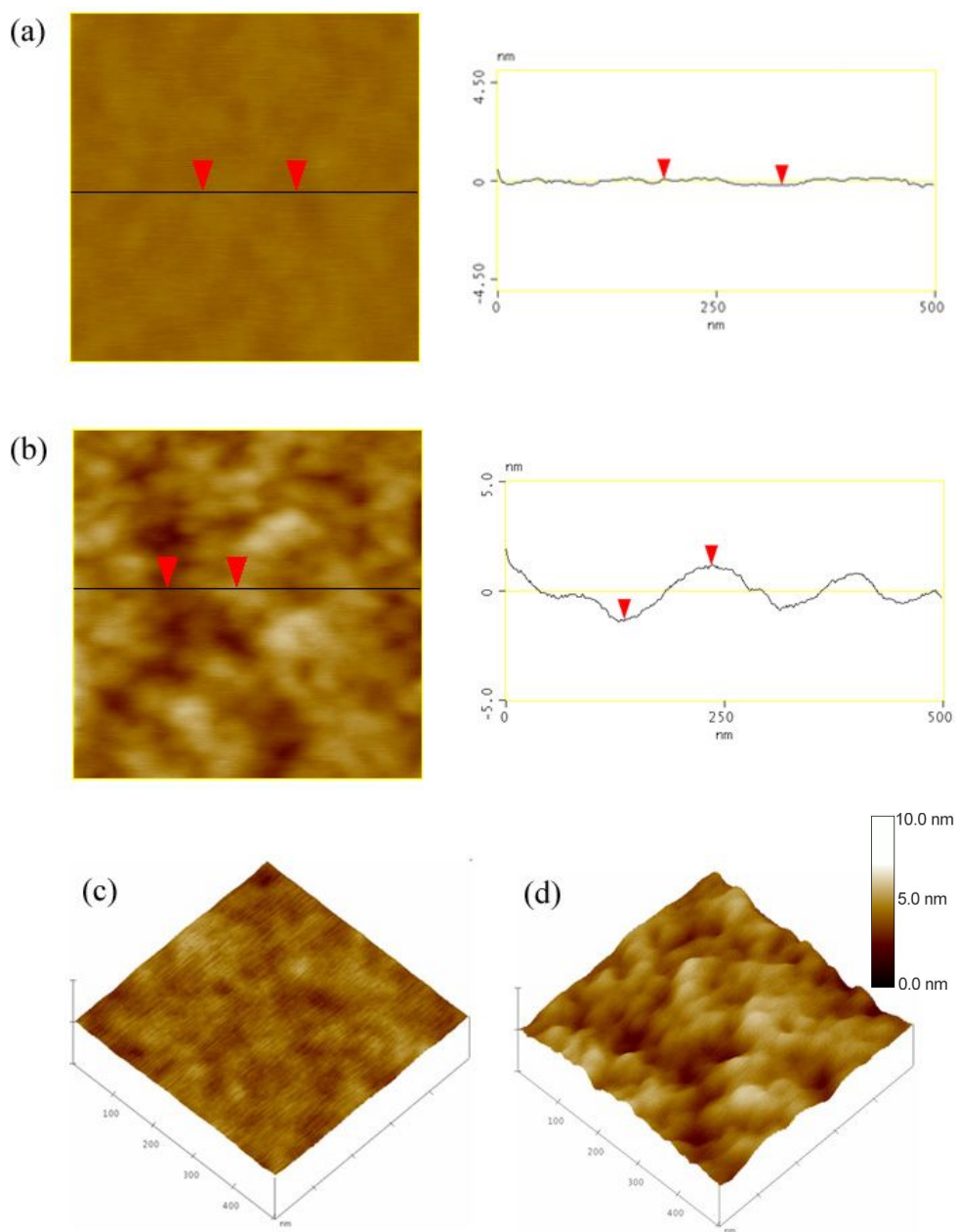


Figure 3.12. Atomic force microscopy images of the dried films of the cast aqueous PVP solutions: a planar view and a cross-sectional profile of the linear PVP (a) and the nanohydrogels of PVP (b), 3D views of the linear PVP (c) and the nanohydrogels of PVP (d).

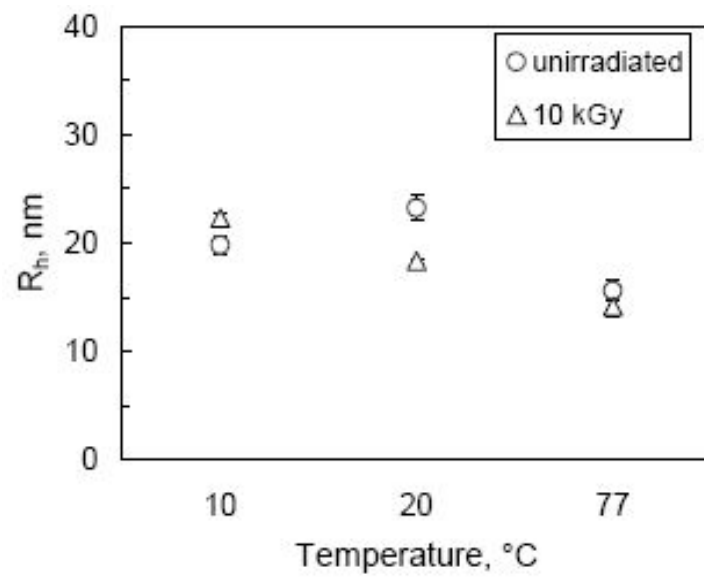
3.3.3. Thermal and dose-rate effects in steady-state radiolysis of PVP aqueous solutions

To study the time-averaged dose rate effect on the nanohydrogels synthesized, steady-state radiolysis (γ -ray radiation) was used and compared to the results from pulsed electron beam irradiation. The time-averaged dose rate of the electron beam radiation used in this work was $9 \times 10^3 \text{ Gy s}^{-1}$ (based on 30 Gy/pulse as a dose rate and 300 Hz as a pulse repetition rate). The time-averaged dose rate used for γ -ray irradiations was 0.97 Gy s^{-1} .

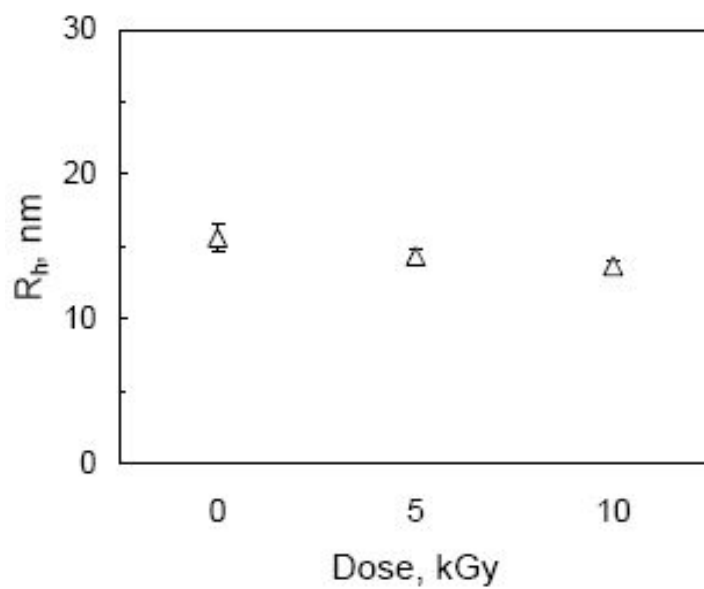
An investigation of the effects of temperature and total dose on R_h was performed on nanohydrogels synthesized by γ -ray irradiation. This work involved analysis of aqueous solutions containing 0.1 wt% ($0.9 \times 10^{-2} \text{ mol L}^{-1}$) PVP. High temperature (77°C) irradiation experiments yielded the smallest R_h ($13.9 \pm 0.9 \text{ nm}$) among the samples irradiated with a total dose of 10 kGy, as was observed in the electron beam irradiated samples (Figure 3.13). However, the R_h and M_w of the γ -irradiated samples were larger than those of the samples irradiated at the same total dose by electron beam (Table 3.4, Figure 3.14). The difference in R_h and M_w of the PVP samples irradiated with different types of radiation (i.e., electron beam and γ -ray) can be explained by the difference in dose rate associated with each of these sources. Under conditions of low dose rate (such as γ -ray irradiation), the inter-molecular crosslinking reaction dominates the system, due to the fewer radical generations within the same PVP chain. The number of PVP radicals formed after single pulse of electron beam irradiation (the dose per $3 \mu\text{s}$ pulse = 30 Gy) is calculated as approximately 6 per each chain. γ -ray irradiation, however, the number

of PVP radicals formed during same time span (3 μ s) by γ -ray irradiation is estimated to be 5.9×10^{-7} per chain. The number of radicals generated in PVP is equal to that of \bullet OH radicals formed from the radiolysis of N_2O -saturated water. The greater number of the PVP radicals within single chain generated by electron beam irradiation therefore enhances the likelihood of intra-molecular radical-radical crosslinking reactions, thereby yielding smaller values of the M_w and R_h .

Figure 3.15 shows PVP solutions of different concentrations after a 10 kGy dose of γ -ray irradiation at 20 $^{\circ}$ C. All samples were saturated with N_2O prior to irradiations and were initially in a transparent form. The 0.1 wt% (0.9×10^{-2} mol L^{-1}) PVP sample retained its original transparent liquid state after irradiation. The 0.3 wt% (2.7×10^{-2} mol L^{-1}) sample transformed into an opaque liquid after irradiation, which is due to increased scattering produced by the greater amount of inter-molecularly crosslinked PVP particles with larger R_h (Figure 3.16). The samples containing concentrations of 0.5 wt% and above yielded an apparent macroscopic gel phase separated from the original liquid phase. 0.3 wt% PVP sample irradiated at high temperature (77 $^{\circ}$ C) yielded a smaller R_h (55.4 ± 0.7 nm) than those prepared at 20 $^{\circ}$ C ($R_h = 136.8 \pm 15.6$ nm). This behavior is believed to originate from the collapsed conformation which is produced at high temperatures which then leads to the formation of more densely crosslinked structure.



(a)



(b)

Figure 3.13. Change of R_h of the PVP polymer nanohydrogels synthesized by γ -ray irradiation as a function of temperature (a) and dose at 77 °C (b).

Table 3.4. Weight averaged molecular weights (M_w , g mol^{-1}) of the PVP samples synthesized by γ -ray irradiation at 77°C .

Dose (kGy)	M_w , g mol^{-1}
0	$(3.94 \pm 0.12) \times 10^5$
5	$(5.25 \pm 0.11) \times 10^6$
10	$(4.08 \pm 0.8) \times 10^6$

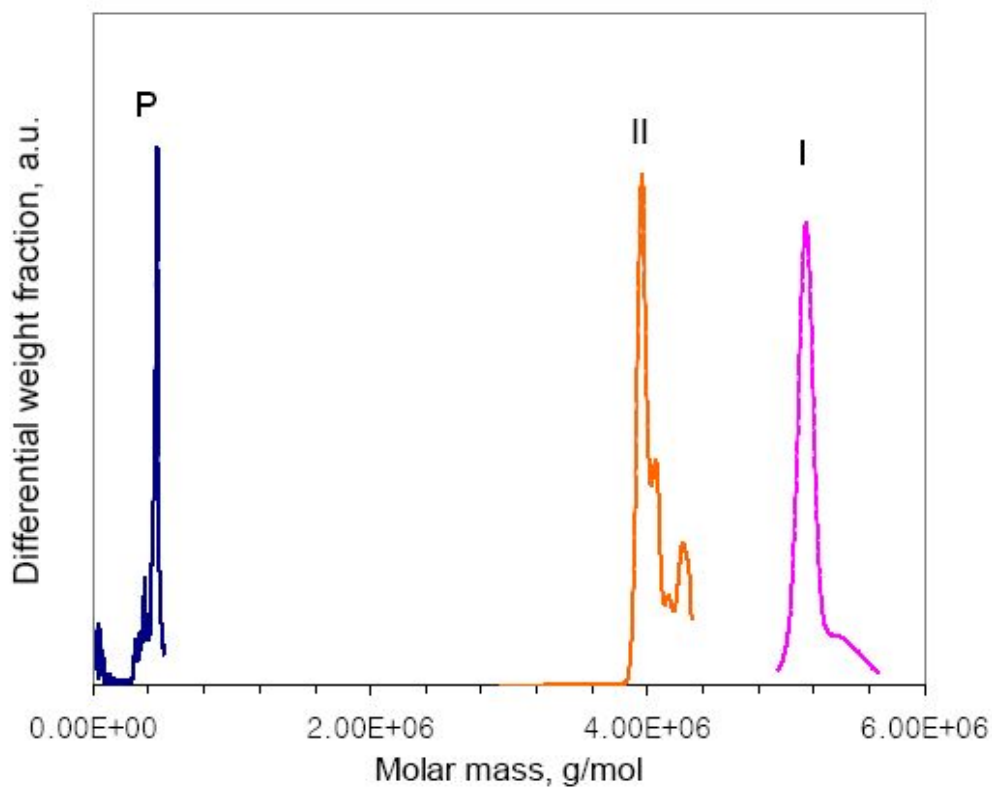


Figure 3.14. Differential molar mass distribution of the PVP samples ($c = 0.9 \times 10^{-2} \text{ mol L}^{-1}$) synthesized by γ -ray irradiation at 77°C with the irradiation conditions: 5 kGy (I) and 10 kGy (II). P is unirradiated PVP.

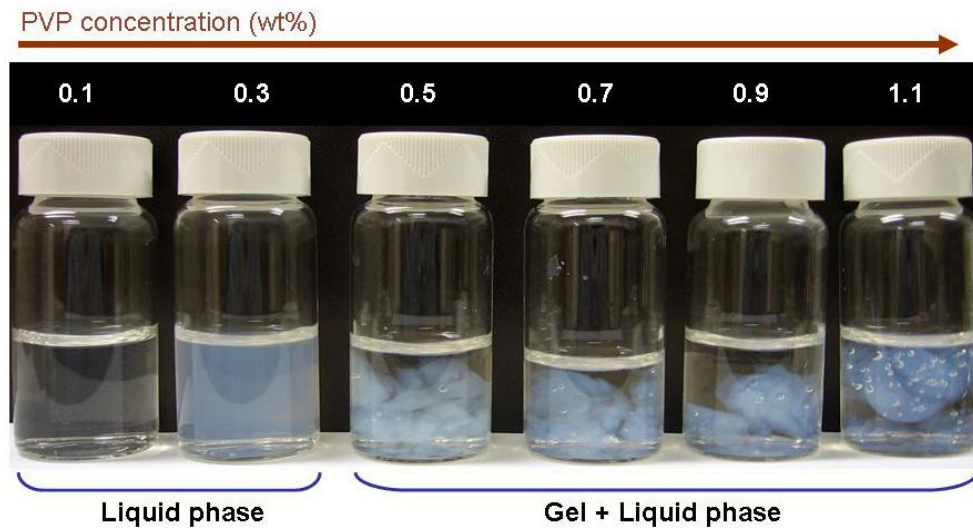


Figure 3.15. PVP samples prepared by γ -ray irradiation at 20 °C with the solution concentrations from 0.1 wt% ($0.9 \times 10^{-2} \text{ mol L}^{-1}$) to 1.1 wt% ($9.9 \times 10^{-2} \text{ mol L}^{-1}$).

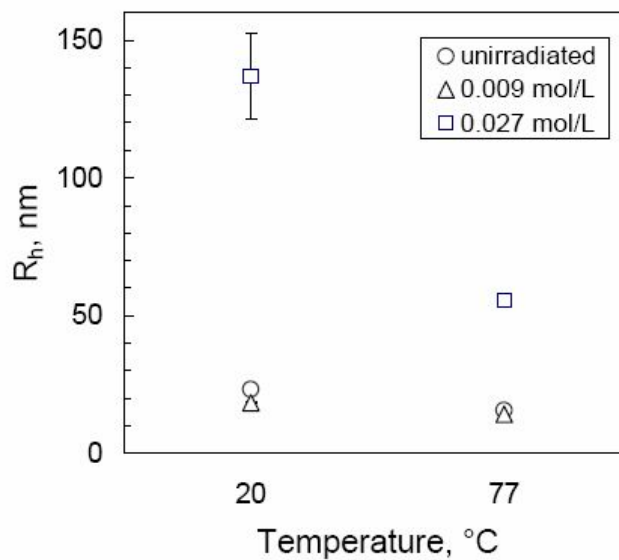


Figure 3.16. Average R_h of the PVP nanohydrogels synthesized by γ -ray irradiation at different temperatures and concentrations.

3.4 Discussion and conclusions.

A mixture of intra- and inter-molecular crosslinking reactions was observed to take place during irradiation of PVP in both its random coil (at room temperature) and thermally collapsed form (at high temperature) at concentrations of $0.9 \times 10^{-2} \text{ mol L}^{-1}$. The center-of-mass diffusion of PVP chains causes the pervaded volume of these coils to be interpenetrated and become entangled with one another. The Zwitterion structure of PVP in water (by keto-enol tautomerization as shown in Figure 3.3) is also expected to introduce a combination of intra- and inter-molecular interactions among the polar groups of PVP through electrostatic forces [68]. By these reasons, the molecular weights of the produced PVP nanohydrogels are therefore expected to increase due to inter-molecular interactions (i.e., bimolecular recombination of carbon-centered radicals) of neighboring PVP chains. D_t (measured by DLS) and the concentration ($0.9 \times 10^{-2} \text{ mol L}^{-1}$) of the polymer can be used to estimate the average time period (t) required for the centers of these molecules to encounter each other. This time was found to be $1.3 \times 10^{-4} \text{ s}$ at $20 \text{ }^\circ\text{C}$ and $0.3 \times 10^{-4} \text{ s}$ at $77 \text{ }^\circ\text{C}$ (calculated using $t = x^2 / 6D$, where t is time interval between molecular collision, x is average distance between molecules in solution, D is translational diffusivity) [77]. If only the translational diffusive motion of the polymer chains is taken into consideration, high temperature conditions are favorable for the enhancement of the frequency of the chain interactions which yield inter-molecular crosslinked product. However, the smaller molecular weight obtained from samples irradiated at higher temperatures implies that another parameter may be affecting the crosslinking reactions, such as

the chain conformation. The shrunken form of PVP produced at high temperature (77 °C), shown in Figure 3.4, is favorable for the intra-molecular crosslinking reaction since it generates shorter inter-radical distances on the same PVP backbone. Therefore, even under the faster diffusive motion of PVP at high temperature, the growth of the molecular weight through inter-radical crosslinking reaction is not as prominent as in samples synthesized at low temperature (20 °C) for solutions containing 0.1 wt% ($0.9 \times 10^{-2} \text{ mol L}^{-1}$) PVP. However, the larger pervaded volumes in random coil (i.e., non-collapsed) conformation at lower temperatures is expected to promote inter-molecular radical-radical crosslinking reaction.

At high pulse repetition rates of electron beam irradiation, a greater number of carbon-centered PVP free radicals is produced than at low pulse rates, thereby preferentially yields the smaller intra-molecularly crosslinked nanohydrogel. Pulse radiolysis of N_2O -saturated PVP solutions at high dose rates and pulse repetition rates is an effective method of enhancing the yield of nanohydrogels. However, even though the dimensions of nanohydrogels are smaller by virtue of the shrinkage associated with internal crosslinks, the weight average molecular weight (M_w) is greater than that of the unirradiated PVP. This means that the inter-molecular crosslinking reactions were not completely excluded and that a fraction of the crosslinked PVP chains become entangled with the intra-linked gel even when they are synthesized in dilute solution ($c = 0.9 \times 10^{-2} \text{ mol L}^{-1}$). A proposed reaction model based on these observations is shown in Figure 3.17.

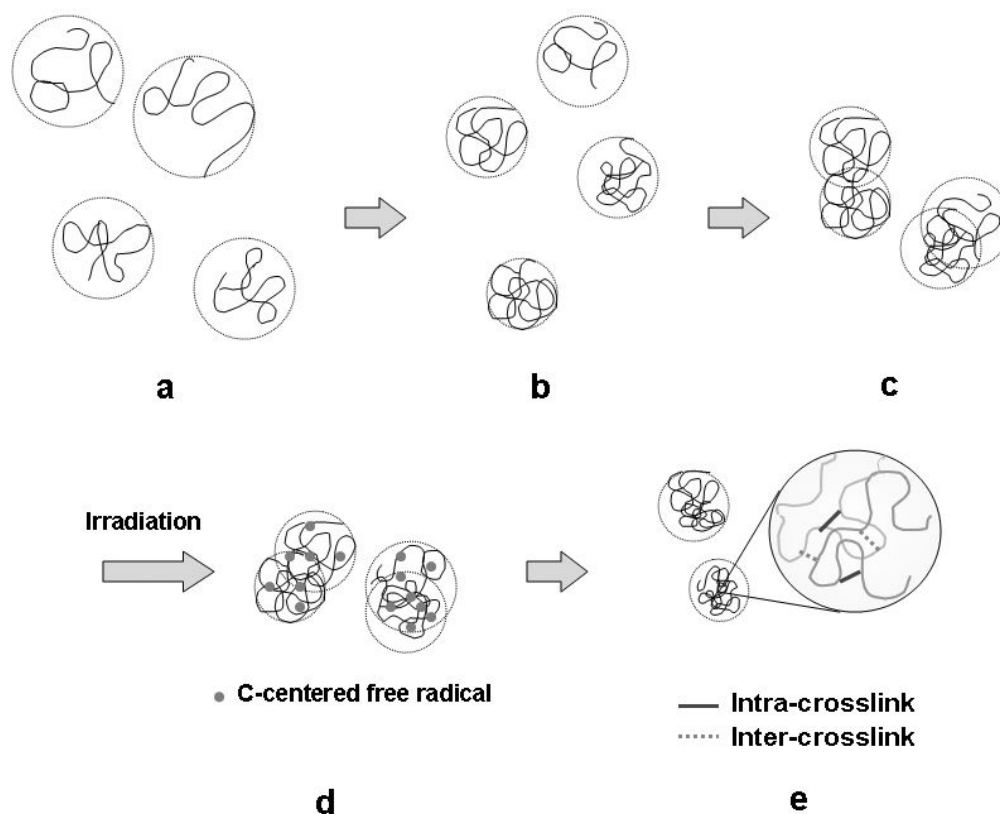


Figure 3.17. Schematic diagram of the mixed crosslinked PVP nanohydrogels formation; dilute solution of PVP ($c = 0.9 \times 10^{-2} \text{ mol L}^{-1}$) (a), collapsed coils at high temperature (b), diffusive interaction of coils (c), C-centered radical formation upon ionizing radiation (d), intra- and inter-crosslinks formation of PVP chains (e).

As the solution concentration is further reduced ($c = 0.45 \times 10^{-2} \text{ mol L}^{-1}$), the inter-molecular PVP radical interaction is inhibited and the molecular weight of the product prepared at high temperature ($77 \text{ }^\circ\text{C}$) is very similar to that of the unirradiated PVP. Sample prepared at higher pulse repetition rates (300 Hz) yielded smaller M_w and R_h than those of the samples prepared at lower pulse repetition rates (20 Hz).

Different time-averaged dose rates (Gy s^{-1}) in electron beam and γ -ray irradiation affect the molecular weight and R_h of the PVP nanohydrogels. A greater number of the coexisting PVP radicals within a single chain generated by electron

beam irradiation increases the likelihood of intra-molecular radical-radical reactions. The pulsed electron beam irradiation at high dose rates is therefore an efficient means of producing compact and densely crosslinked nanohydrogels.

Chapter 4:

KINETICS OF FREE RADICAL REACTIONS

This chapter presents an investigation of the kinetics of intra- and inter-molecular crosslinking reactions of the carbon-centered PVP free radicals at various temperatures by pulse radiolysis; the activation energies of the intra- and inter-molecular radical reactions were determined from the Arrhenius plot of the reaction rate constant as a function of temperature.

4.1 Introduction and previous works

The optical spectroscopic method employed in pulse radiolysis involves the use of a photomultiplier to measure the light transmitted by a sample which has been irradiated by an electron pulse. Pulse radiolysis studies on the reaction kinetics of radiolytically generated transient species have been investigated for various hydrophilic polymers, including poly(acrylic acid) [7, 78-81], poly(ethylene oxide)[82], and poly(N-isopropyl acrylamide) [83, 84]. The dilute ($c = 0.01 \text{ mol L}^{-1}$) aqueous solutions of PVP ($M_n = 1.6 \times 10^4 \text{ g mol}^{-1}$) and its corresponding monomer N-vinylpyrrolidone (VP) were studied by the pulse radiolysis combined with optical spectroscopic technique [43]. In N_2O -saturated solutions, $\bullet\text{OH}$ from the radiolysis of water is the major species which abstracts H from the polymer backbone thereby yielding carbon-centered PVP radicals. The absorption spectra of the PVP radicals showed maximum at 390 nm and the corresponding decay constant ($2k_2$) was reported

as $(1.5 \pm 0.2) \times 10^8 \text{ L mol}^{-1} \text{ s}^{-1}$ at $25 \text{ }^\circ\text{C}$ [43]. However, the decay kinetics of PVP radicals as a function of temperature and the corresponding activation energies at different chain conformations have not been reported yet within my knowledge. At high temperature, PVP chains with thermally collapsed conformation and enhanced diffusivity are expected to show different radical-radical crosslinking behaviors compared to those at room temperature. To prove this, pulse radiolysis experiments at wide temperature range ($28 - 77 \text{ }^\circ\text{C}$) were performed using N_2O -saturated dilute PVP aqueous solutions ($M_w = (3.94 \pm 0.12) \times 10^5 \text{ g mol}^{-1}$, $c = 0.9 \times 10^{-2} \text{ mol L}^{-1}$).

4.2 Experiments and results

4.2.1 Absorption spectra of transient species

Prior to the irradiations, N_2O was purged into each solution for 30 min to double the yield of OH^\bullet generation (G-value from 0.28 to $0.56 \text{ } \mu\text{mol J}^{-1}$). To confirm this N_2O effect, pulse radiolysis results at 480 nm using air- and N_2O -saturated KSCN solutions are represented in Figure 4.1. The absorbance of N_2O -saturated KSCN solution (460×10^{-3}) upon pulse is approximately twice that of air saturated sample (235×10^{-3}). The number of generated $(\text{CNS})_2^-$ was doubled due to the reaction with additional $^\bullet\text{OH}$ converted from e_{aq}^- by N_2O . The calculated doses for air- (using G-value of $0.28 \text{ } \mu\text{mol J}^{-1}$) and N_2O -saturated solutions (using G-value of $0.56 \text{ } \mu\text{mol J}^{-1}$) were 102.2 and $101.1 \text{ Gy pulse}^{-1}$, respectively.

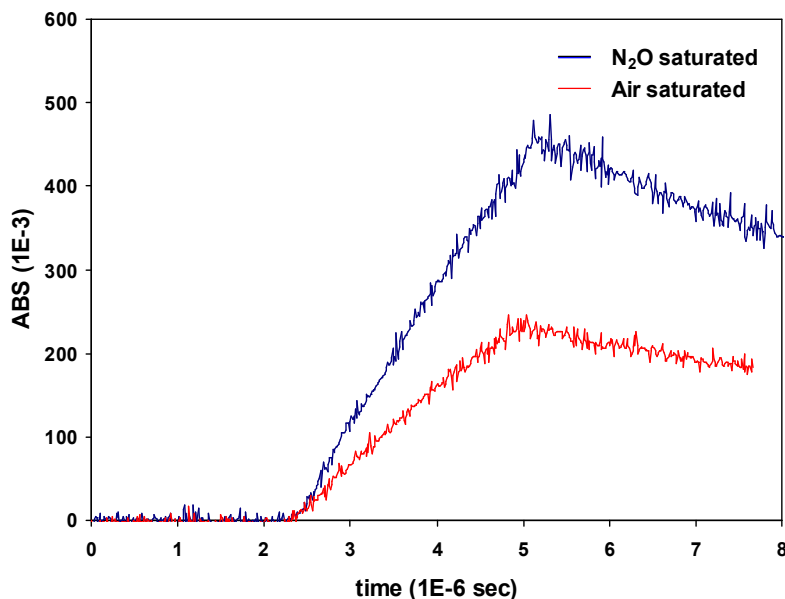


Figure 4.1. The comparison of build up between N₂O- and air-saturated KSCN solutions monitored at 480 nm.

The absorption spectrum of H-abstracted transient (PVP-H)[•] formed during pulse radiolysis of N₂O-saturated PVP aqueous solutions ($c = 0.9 \times 10^{-2} \text{ mol L}^{-1}$) is shown in Figure 4.2. Broad absorption over the wavelength range 320 - 460 nm was observed with a maximum at 390 nm as previous work using PVP of different molecular weight ($M_n = 1.6 \times 10^4 \text{ g mol}^{-1}$) [43]. The molar absorption coefficient at 390 nm ($\epsilon_{390 \text{ nm}}$) was calculated using following expression:

$$\epsilon_{390 \text{ nm}} = \frac{\Delta A \times N_A}{D \times G \times l} \quad (4.2)$$

where D is dose (Gy), ΔA is absorbance difference, N_A is Avogadro's number, G is G-value of (PVP-H)[•] formed during pulse radiolysis (i.e., $0.62 \mu\text{mol J}^{-1}$) and l is optical path length of the cell (1 cm).

From Eq. (4.2), $\epsilon_{390 \text{ nm}}$ was measured as $510 \pm 30 \text{ L mol}^{-1} \text{ cm}^{-1}$ at $25 \text{ }^\circ\text{C}$. This value is smaller than that of the previous work ($\epsilon_{390 \text{ nm}} = 1200 \pm 200 \text{ L mol}^{-1} \text{ cm}^{-1}$ at $25 \text{ }^\circ\text{C}$) performed with lower molecular weight of $1.6 \times 10^4 \text{ g mol}^{-1}$ [43].

For comparison, the absorption spectrum and $\epsilon_{390 \text{ nm}}$ of PVP solution with similar molecular weight range ($M_w = 4 \times 10^4 \text{ g mol}^{-1}$) were measured and represented in Figure 4.3. A similar broad absorption spectrum at $330 - 430 \text{ nm}$ (with a maximum at 390 nm) was observed as in previous result [43] and Figure 4.2. The $\epsilon_{390 \text{ nm}}$ determined by our pulse radiolysis system was found to be $522 \pm 16 \text{ L mol}^{-1} \text{ cm}^{-1}$ at $25 \text{ }^\circ\text{C}$. It is very similar to $\epsilon_{390 \text{ nm}}$ of high molecular weight PVP ($\epsilon_{390 \text{ nm}} = 510 \pm 30 \text{ L mol}^{-1} \text{ cm}^{-1}$ at $25 \text{ }^\circ\text{C}$). This demonstrates that $\epsilon_{390 \text{ nm}}$ does not depend on polymer molecular weight because the chemical structures of carbon-centered free radicals in both low ($M_w = 4 \times 10^4 \text{ g mol}^{-1}$) and high ($M_w = 3.94 \times 10^5 \text{ g mol}^{-1}$) molecular weight are identical.

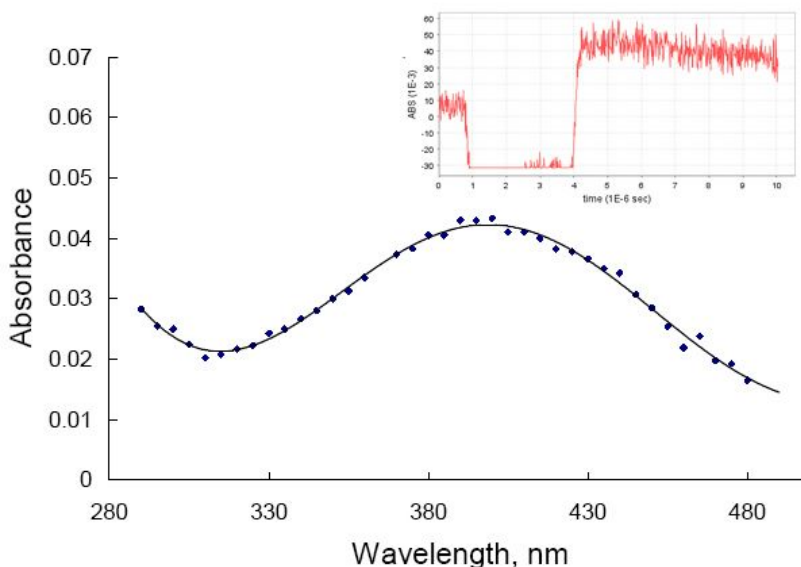


Figure 4.2. Absorption spectrum of the transient species formed (measured at $2 \mu\text{s}$ after $3 \mu\text{s}$ width pulse) by pulse radiolysis of N_2O -saturated $0.9 \times 10^{-2} \text{ mol L}^{-1}$ PVP ($M_w = (3.94 \pm 0.12) \times 10^5 \text{ g mol}^{-1}$) aqueous solution at $25 \text{ }^\circ\text{C}$. Inset is the buildup profile of the transient species at 390 nm .

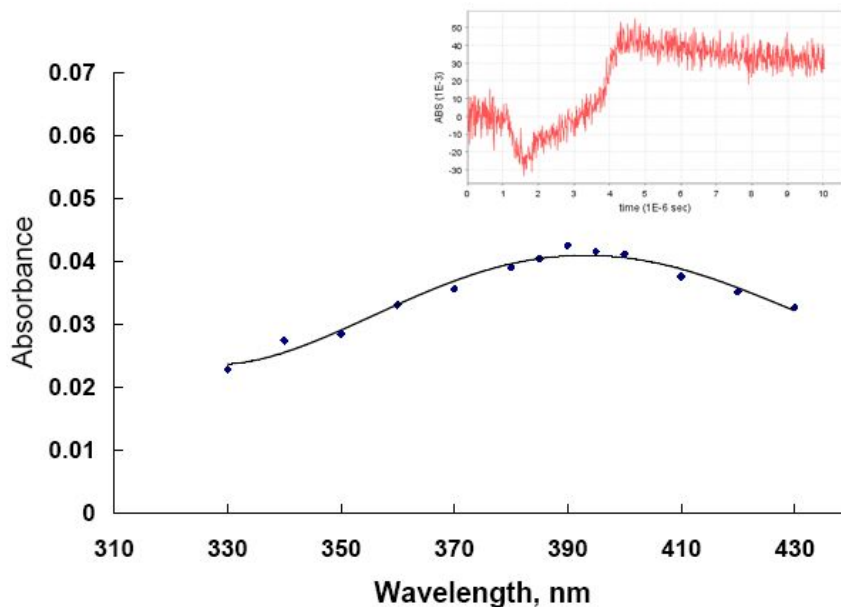


Figure 4.3. Absorption spectrum of the transient species of N_2O -saturated PVP aqueous solution (measured at $2 \mu s$ after $3 \mu s$ width pulse) at $25 \text{ }^\circ\text{C}$; concentration of PVP solution is $0.9 \times 10^{-2} \text{ mol L}^{-1}$ and molecular weight of PVP is $4 \times 10^4 \text{ g mol}^{-1}$. Inset is the buildup profile of the transient species at 390 nm .

It should be noted, however, that monomer form, N-vinyl pyrrolidone (VP) shows a different ϵ and an absorption spectrum (Figure 4.5). The chemical structures of VP and PVP are compared in Figure 4.4.

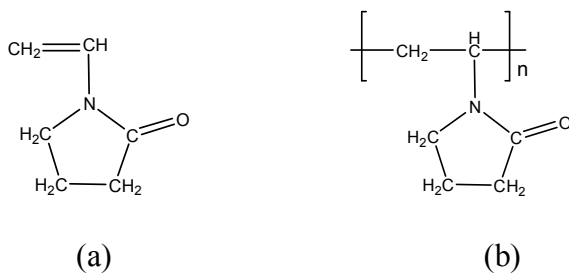


Figure 4.4. Chemical structures of N-vinyl pyrrolidone (VP) (a) and Poly(vinyl pyrrolidone) (PVP).

The absorption spectrum of the transient species (VP-H) \bullet of N-vinyl pyrrolidone (VP) is characterized by a broad absorption in the region 300 – 400 nm with the maximum absorption centered on about 350 nm as found in previous reports [43, 85]. The molar absorption coefficient at a maximum absorbing wavelength 350 nm ($\epsilon_{350\text{nm}}$) was measured as $1338 \pm 85 \text{ L mol}^{-1}\text{cm}^{-1}$ (Figure 4.5). However, previously published values of $\epsilon_{350\text{nm}}$ [43, 85] are not in accordance with each other (i.e., $2200 \pm 200 \text{ L mol}^{-1}\text{cm}^{-1}$ [43] vs. $1300 \text{ L mol}^{-1}\text{cm}^{-1}$ approximately [85]). The $\epsilon_{350\text{nm}}$ determined from my work agrees with the later result [85].

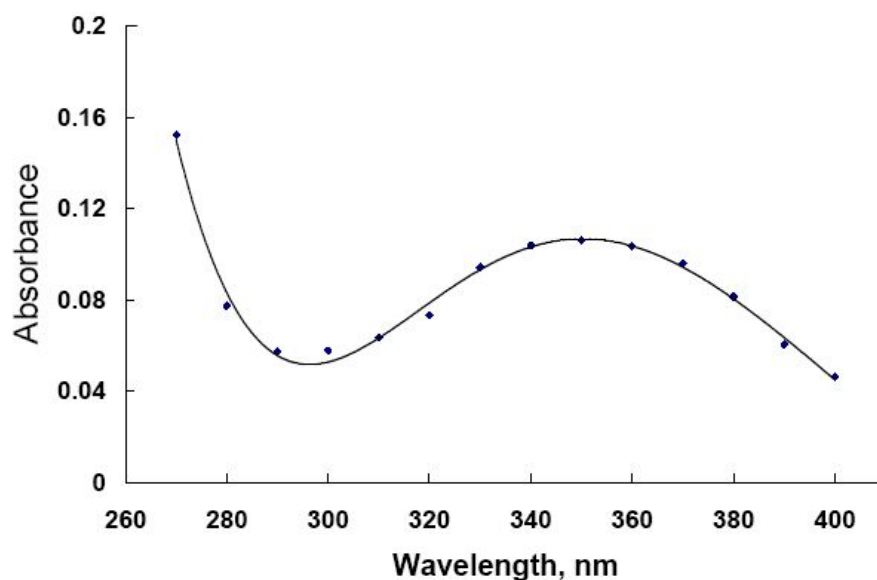


Figure 4.5. Absorption spectrum of the transient species of N₂O-saturated VP aqueous solution (measured at 1 μs after 3 μs width pulse) at 25 $^{\circ}\text{C}$; concentration of VP solution is $0.5 \times 10^{-2} \text{ mol L}^{-1}$.

4.2.2 Reaction rate constant for polymer radical reaction

The measured molar absorption coefficient ($\epsilon_{390 \text{ nm}}$) of PVP ($M_w = (3.94 \pm 0.12) \times 10^5 \text{ g mol}^{-1}$) aqueous solutions decreases as temperature increases as shown in Figure 4.6.

It may be explained by the reduced radiation chemical yield of $\bullet\text{OH}$ at high temperature because the solubility of N_2O decreases as temperature increases [86].

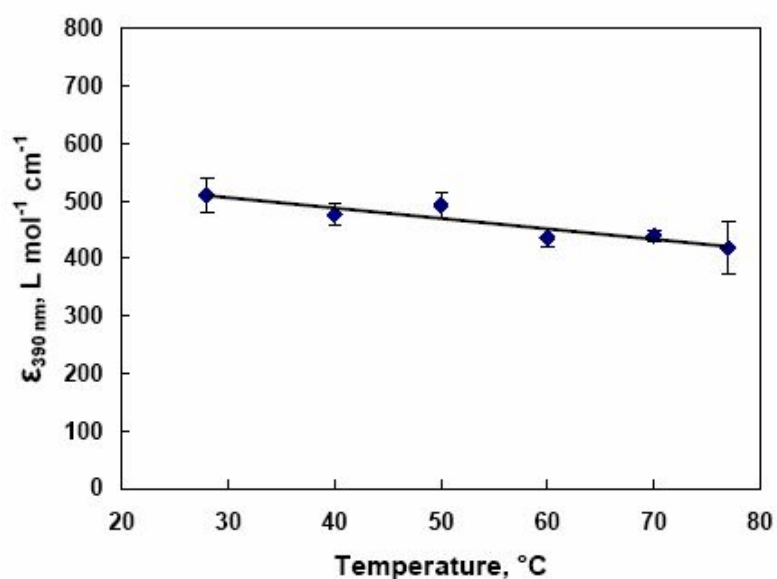


Figure 4.6. Change of molar absorption coefficient ($\epsilon_{390 \text{ nm}}$) as a function of temperature in N_2O -saturated PVP aqueous solutions ($c = 0.9 \times 10^{-2} \text{ mol L}^{-1}$).

The typical decay profile of the transient species of PVP at 390 nm shows second order radical decay characteristics as shown in Figure 4.7.

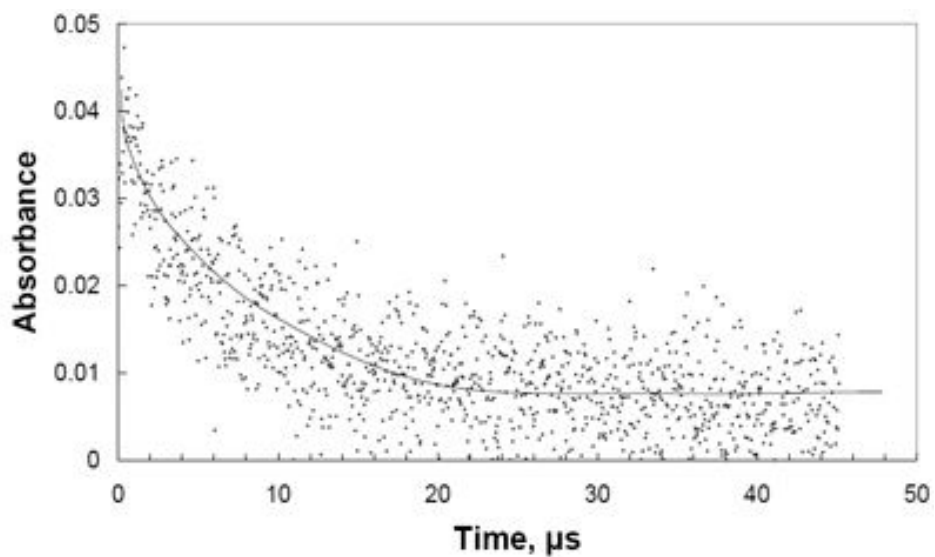


Figure 4.7. Second order decay profile of the transient species at 390 nm in N₂O-saturated PVP aqueous solutions ($c = 0.9 \times 10^{-2} \text{ mol L}^{-1}$) at 25 °C.

The decay profiles at different temperatures in the range of 28 – 77 °C are presented in Figure 4.8.1 to 4.8.9 and the correspondingly calculated second order reaction rate constants ($2k_2$) are shown in Figure 4.9.

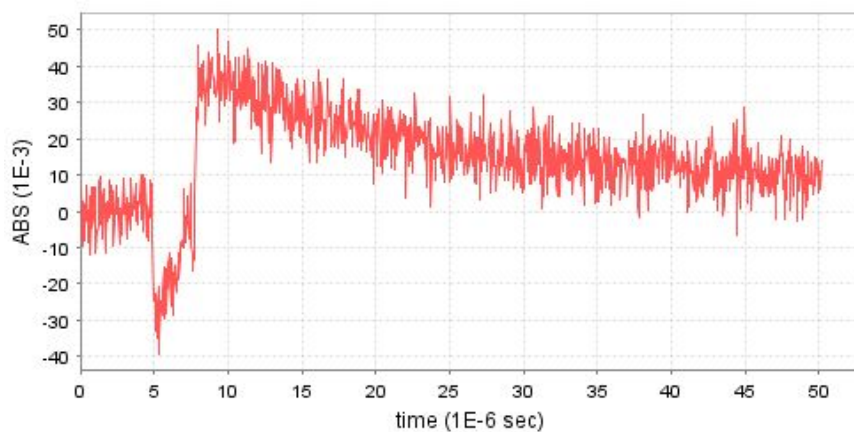


Figure 4.8.1. Decay of (PVP-H)[•] radicals monitored at 390 nm in N₂O-saturated PVP aqueous solution ($c = 0.9 \times 10^{-2} \text{ mol L}^{-1}$) at 28 °C.

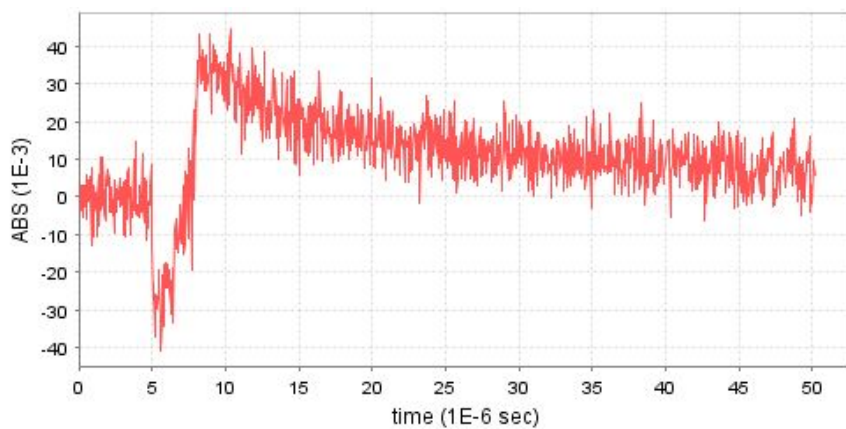


Figure 4.8.2. Decay of (PVP-H)[•] radicals monitored at 390 nm in N₂O-saturated PVP aqueous solution ($c = 0.9 \times 10^{-2} \text{ mol L}^{-1}$) at 40 °C.

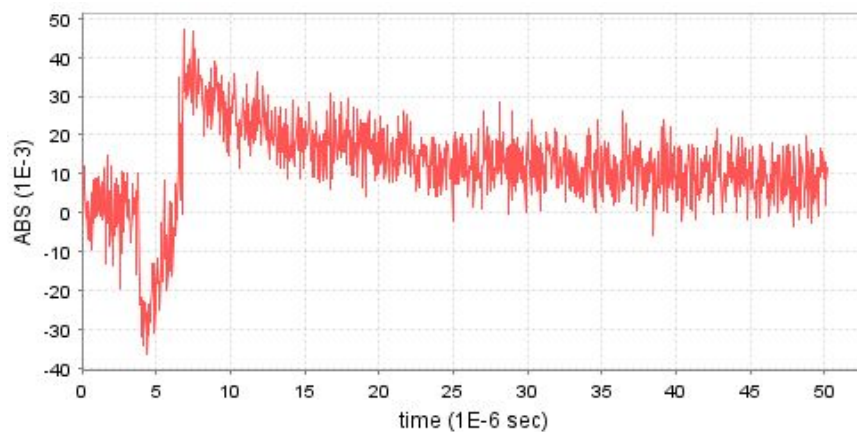


Figure 4.8.3. Decay of (PVP-H)[•] radicals monitored at 390 nm in N₂O-saturated PVP aqueous solution ($c = 0.9 \times 10^{-2} \text{ mol L}^{-1}$) at 50 °C.

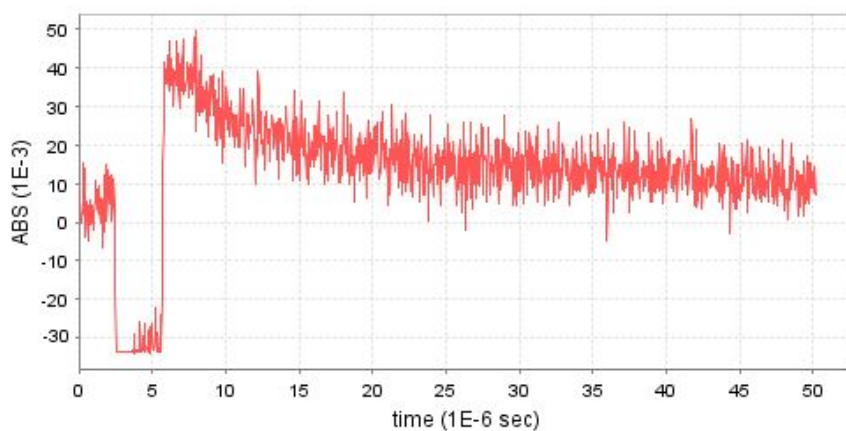


Figure 4.8.4. Decay of (PVP-H)[•] radicals monitored at 390 nm in N₂O-saturated PVP aqueous solution ($c = 0.9 \times 10^{-2} \text{ mol L}^{-1}$) at 55 °C.

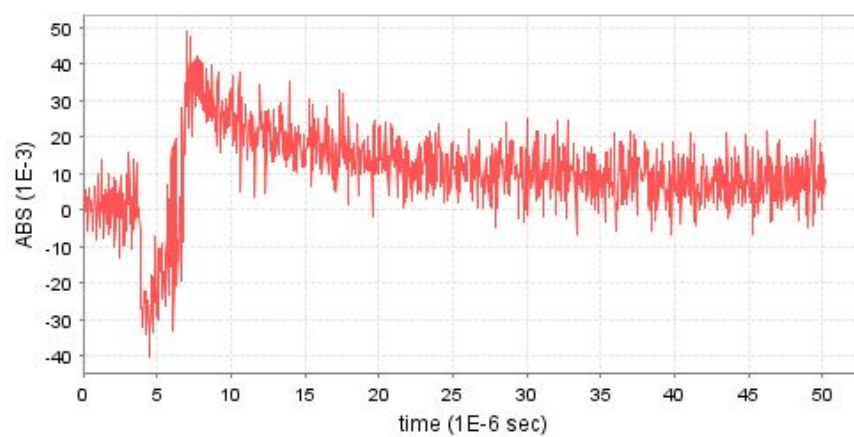


Figure 4.8.5. Decay of (PVP-H)[•] radicals monitored at 390 nm in N₂O-saturated PVP aqueous solution ($c = 0.9 \times 10^{-2} \text{ mol L}^{-1}$) at 60 °C.

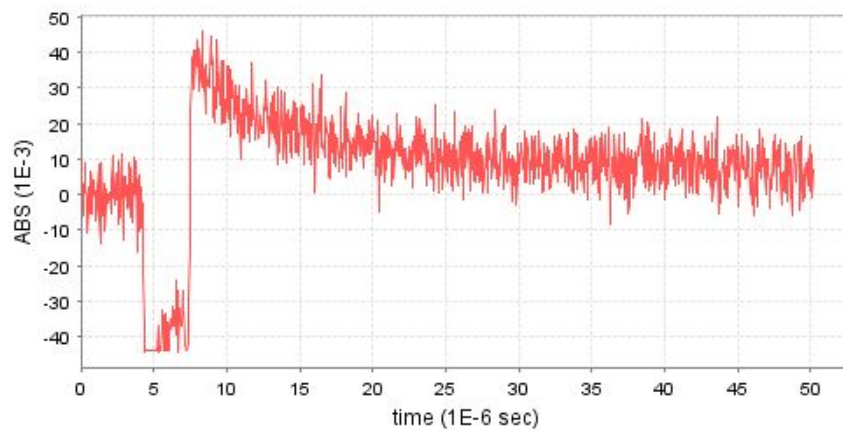


Figure 4.8.6. Decay of (PVP-H)[•] radicals monitored at 390 nm in N₂O-saturated PVP aqueous solution ($c = 0.9 \times 10^{-2} \text{ mol L}^{-1}$) at 65 °C.

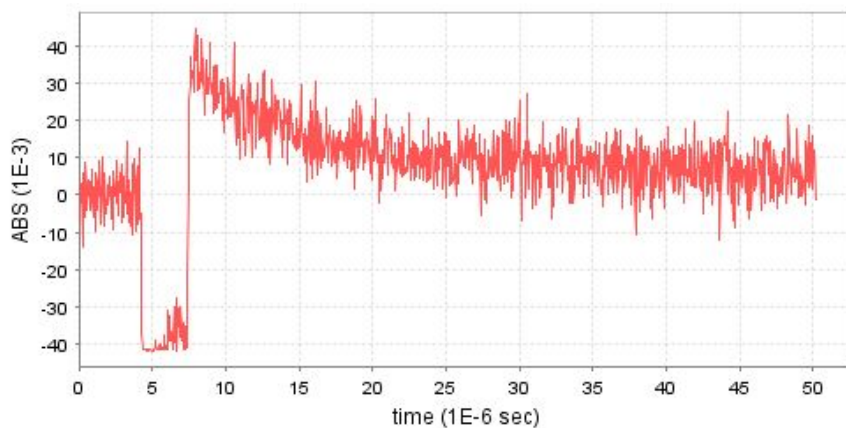


Figure 4.8.7. Decay of (PVP-H)[•] radicals monitored at 390 nm in N₂O-saturated PVP aqueous solution ($c = 0.9 \times 10^{-2} \text{ mol L}^{-1}$) at 70 °C.

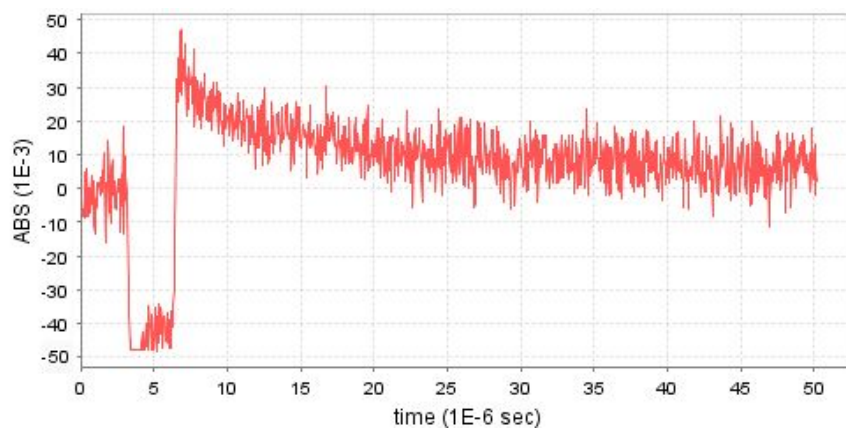


Figure 4.8.8. Decay of (PVP-H)[•] radicals monitored at 390 nm in N₂O-saturated PVP aqueous solution ($c = 0.9 \times 10^{-2} \text{ mol L}^{-1}$) at 75 °C.

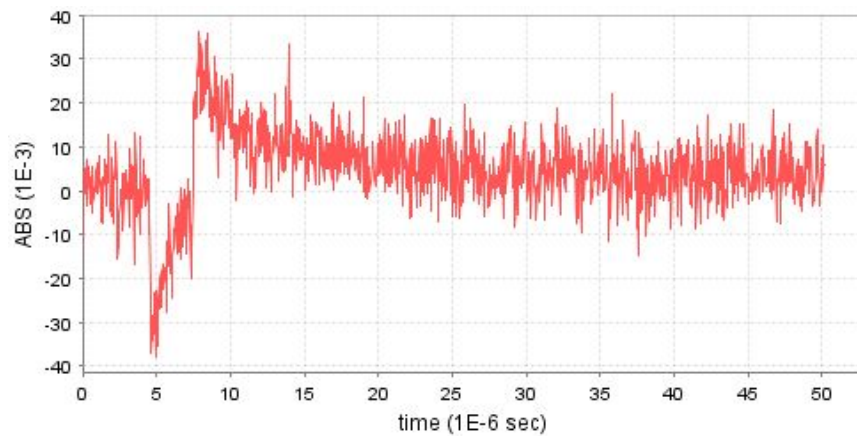


Figure 4.8.9. Decay of (PVP-H)[•] radicals monitored at 390 nm in N₂O-saturated PVP aqueous solution ($c = 0.9 \times 10^{-2} \text{ mol L}^{-1}$) at 77 °C.

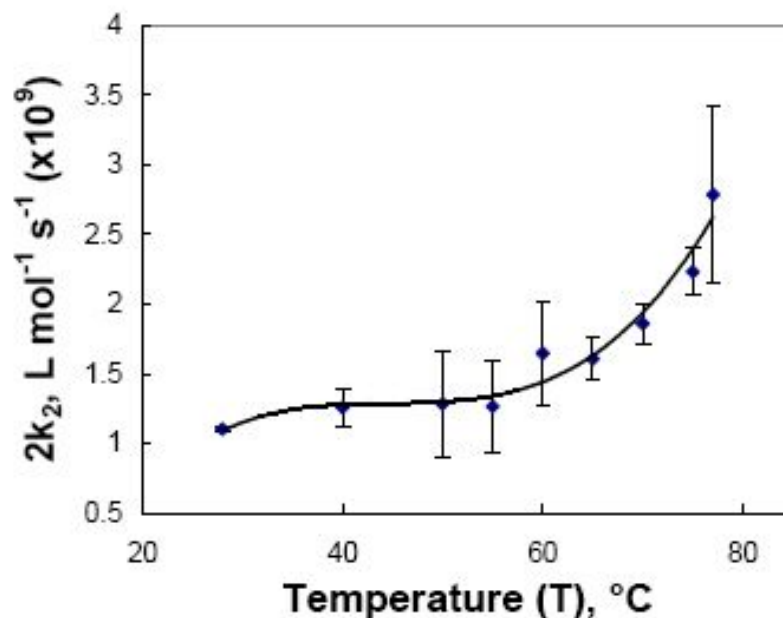


Figure 4.9. Change of the second order reaction (decay) rate constant ($2k_2$) as a function of temperature in N_2O -saturated PVP aqueous solutions ($c = 0.9 \times 10^{-2} \text{ mol L}^{-1}$).

4.2.3 Activation energy of polymer radical decay

The activation energy (E_a) of inter- and intra-molecular PVP radical decay reactions is determined from an Arrhenius plot. When the logarithm of $2k_2$ is plotted as a function of the reciprocal of temperature ($1/T$), a straight line with a negative slope (exothermic process) is obtained with two distinctive slopes (Figure 4.10). The slope corresponds to $-E_a/R$, where R is the gas constant. The E_a in the temperature range of 28 to 50 °C was determined as $1.0 \pm 0.4 \text{ kcal mol}^{-1}$. In the high temperature range (55 - 77 °C), greater E_a ($6.8 \pm 1.9 \text{ kcal mol}^{-1}$) was observed with steeper slope.

This may be explained by the different rate-determining mechanism of polymer radical-radical recombination reaction caused by the changes of chain conformation upon temperature. Low E_a reflects the diffusion-controlled polymer radical-radical reactions in good solvent, thereby inter-molecular crosslinking reactions are expected to be predominant reaction at the temperature range of below 50°C. However, at the higher temperature range of 55 - 77 °C, polymer chains are segregated from aqueous solution by phase separation and collapse by themselves because of the disruption of hydrogen bonds between water and PVP molecules. The mobility of polymer segments having less hydrogen bond with water is expected to reduce; thereby the E_a for polymer radical-radical recombination reactions is increased.

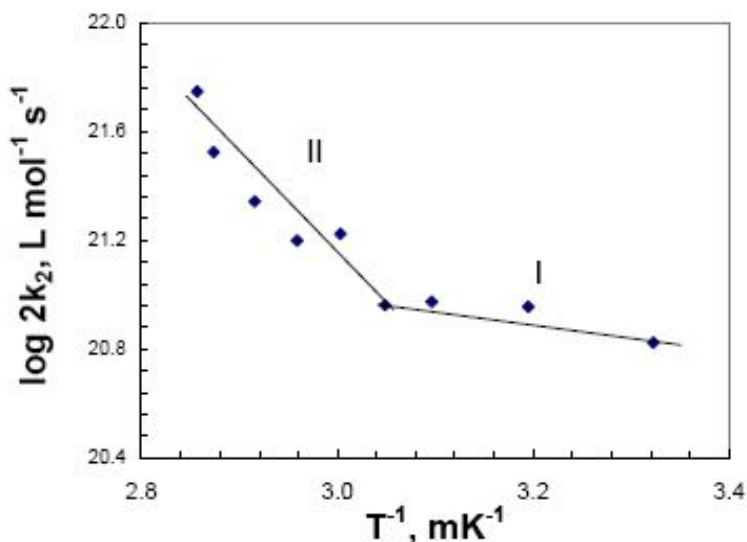


Figure 4.10. Arrhenius plot of the PVP radical decay rate constant from which average activation energies: $E_a = 1.0 \pm 0.4$ kcal mol $^{-1}$ (I) and 6.8 ± 1.9 kcal mol $^{-1}$ (II) were derived for two different temperature regions in N₂O-saturated PVP aqueous solutions ($c = 0.9 \times 10^{-2}$ mol L $^{-1}$).

4.3 Discussion and conclusions

The second order decays observed in pulse radiolysis experiments are attributed to the mixture of intra- and inter-crosslinking reactions between PVP carbon-centered free radicals. The temperature-dependent conformation and translational diffusivity of PVP in water are expected to affect the behavior of polymer radical-radical recombination. At high temperatures (55 – 77 °C), inter-distances of the radiolytically generated carbon-centered free radicals on a same chain is expected to decrease (i.e., more concentrated radicals in unit pervaded volume of polymer strand) than those at low temperatures (28 - 50 °C) because of the collapsed chain conformation. Therefore faster $2k_2$ was observed in the high temperature region. However, conformation of polymer chains becomes a random coil (i.e., non-collapsed) at low temperatures with longer polymer radical-radical distance on a same chain upon irradiation, thereby $2k_2$ is lower than the observed values at high temperatures.

The movement of carbon-centered free radicals is restricted by the mobility of the polymer segments (i.e., inter-connected monomers) and is expected to decrease in the collapsed chain conformation. In water depleted (i.e., hydrogen bond disrupted) PVP strand at high temperature, the motion of the individual polymer segment requires more energy to overcome the increased friction. However, at low temperatures, water-PVP hydrogen bonds make segmental motion of polymer chain easier by hydrodynamic interactions [77]. The collapsed conformation at high temperature, however, is expected to introduce more entangled and interpenetrated

form restricting free movement of polymer strand. Thereby the activation energy required for the radical-radical recombination reaction is expected to be higher in the collapsed conformation.

Chapter 5:

TEMPLATE-ASSISTED SYNTHESIS OF NANOHYDROGELS

5.1 Introduction and previous works

The template synthesis became very popular for its efficiency and convenience to produce one-dimensionally structured nanomaterials [59, 87, 88]. Anodized alumina membrane possesses the uniform and straight cylindrical holes with controlled aspect ratio. After filling the desired materials into the holes of membrane, homogeneously ordered nanostructures can be easily produced by dissolving the membrane in alkali solutions (e.g., sodium hydroxide solution) [87]. The shape and dimension of nanoscopic polymer materials prepared by this method is easily controlled by treated time, surface chemistry of membrane, temperature, etc. [59, 88]. The polymer solution can be introduced into the inner nano-capillary holes by a natural capillary force or a pressurized injection.

The behavior of confined polymer chains in a cylindrical pore is generally explained by the biaxial compression model as follows [89]. A polymeric chain is squeezed into a cylindrical pore of diameter D , where D defines a natural compression blob size. If the chain length scale is smaller than D , the chain follows the statistics of an undeformed chain. For the real chain, the number of monomers g in a compression blob of size D is shown as:

$$g \approx \left(\frac{D}{b}\right)^{5/3} \quad (5.1)$$

where b is the size of monomer. In the case of confinement of a real chain in a cylinder, the length of a tube R_{\parallel} occupied by an real chain can be estimated as the compression blobs which repel each other and fill the pore in a sequential array and given by:

$$R_{\parallel} \approx D \left(\frac{N}{g}\right) \approx \left(\frac{b}{D}\right)^{2/3} Nb \quad (5.2)$$

where N is the number of monomers. The occupied length R_{\parallel} increases as the tube diameter D decreases. The real chain confined in a cylinder of diameter D is shown schematically in Figure 5.1.

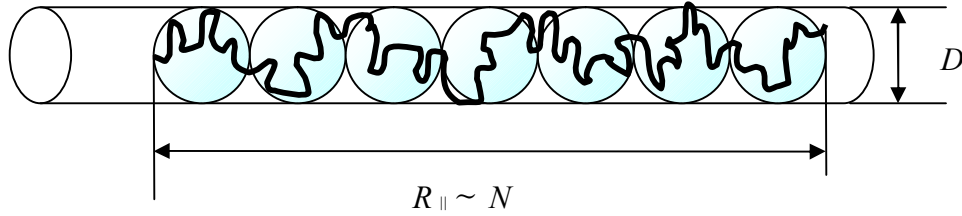


Figure 5.1. Schematic of a real chain confined in a cylinder of diameter D [89].

The free energy of confinement for real chain is of the order of $k_B T$ per compression blob for chain as following equation [89]:

$$F_{conf} \approx k_B T \frac{N}{g} \approx k_B T N \left(\frac{b}{D}\right)^{5/3} \approx k_B T \left(\frac{R_F}{D}\right)^{5/3} \quad (5.3)$$

where k_B is Boltzmann constant, T is temperature, R_F is the end-to-end distance of unconfined real chain. From Eq. (5.2), the $R_{||}$ of the PVP molecule is calculated as approximately 45 nm by using 6.4×10^{-10} nm as the size of the monomer b [90].

The produced shape and dimension are strongly affected by the surface chemistry of inner capillary pores and the physical conformation of polymer chains. The PVP nanostructure synthesis with an alumina porous membrane were reported previously [88]. PVP aqueous solutions were injected into the membrane and the self assembled arrays were attained. Depending on the chemical characteristics (i.e. hydrophilic or hydrophobic) of the inner capillary pore surface, the morphology-controlled one-dimensional nanostructured PVP arrays were produced in either nanotube or wire structure [88]. However, no chemical crosslinking process was applied for these samples.

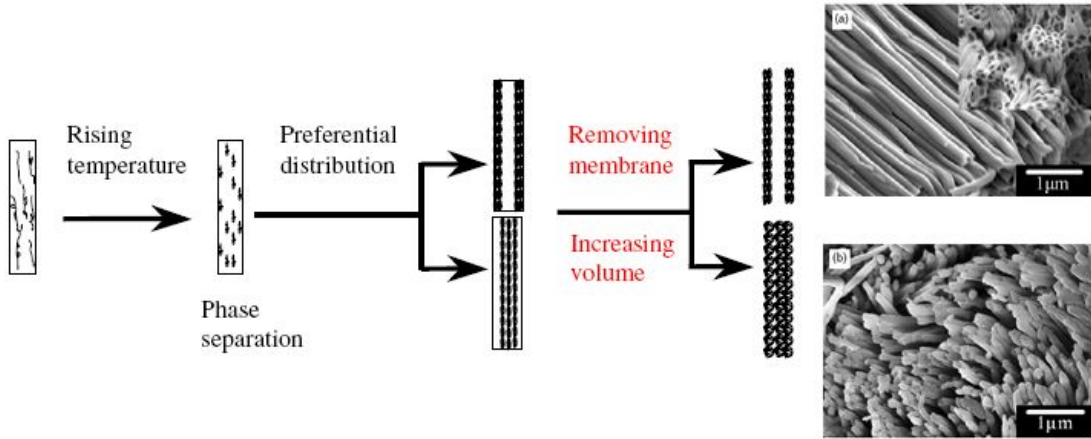


Figure 5.2. Schematic illustration of the formation of PVP nanostructures and the FESEM images of PVP nanotubes (a) and PVP nanowires (b) [88].

In this work, unlike the previous approach, the crosslinked PVP nanohydrogel particles were prepared within the nanoporous membrane by ionizing radiation. Each

capillary pore in the nanoporous membrane is expected to provide a physical isolation of polymer chains, reducing the likelihood of inter-molecular polymer radical-radical crosslinking reactions upon irradiation. Nanohydrogels synthesis by template-assisted ionizing radiation is expected to be an effective preparation method for the nanostructured polymer gels. AFM and ESEM were used to investigate the surface morphology and size of the products.

5.2 Experiments and results

2.5 g of PVP (Aldrich, $M_w = (3.94 \pm 0.12) \times 10^5 \text{ g mol}^{-1}$, determined by asymmetric flow field flow fractionation (AF4) chromatography) was dissolved in 250 mL of deionized water (concentration = $9 \times 10^{-2} \text{ mol L}^{-1}$) and allowed to stir for overnight. The alumina (Al_2O_3) nanoporous membrane disc (Whatman, Anopore™) with 200 nm mean capillary pore diameter (Figure 5.3) was used as a nanotemplate without surface modification. The membrane was placed on PVP aqueous solution for 12 h to introduce solution into the cylindrical pores by capillary force.

The maximum height (h_{max}) to which the PVP aqueous solution can be lifted within the capillary pore can be calculated by following expression [91]:

$$h_{\text{max}} = \frac{2T}{\rho g r} \quad (5.4)$$

where h_{max} is the maximum height (m), T is the surface tension (J m^{-2}), ρ is density of the PVP aqueous solution (kg m^{-3}), g is the gravitational constant ($6.673 \times 10^{-11} \text{ m}^3 \text{ kg}^{-1} \text{ s}^{-2}$) and r is the capillary pore radius ($2 \times 10^{-7} \text{ m}$) of the nanoporous membrane. The surface tension (T) of PVP was determined as $6.3 \times 10^{-2} \text{ J m}^{-2}$ in previous work [92], thereby calculated h_{max} is approximately 128.6 m. Considering the height of the membrane ($6 \times 10^{-5} \text{ m}$), the capillary pore in the membrane can be filled up with dilute PVP solutions very easily. The number of introduced PVP molecules is estimated as 3.15×10^4 in each single capillary pore from the geometry of pore structure and concentration of PVP aqueous solution.

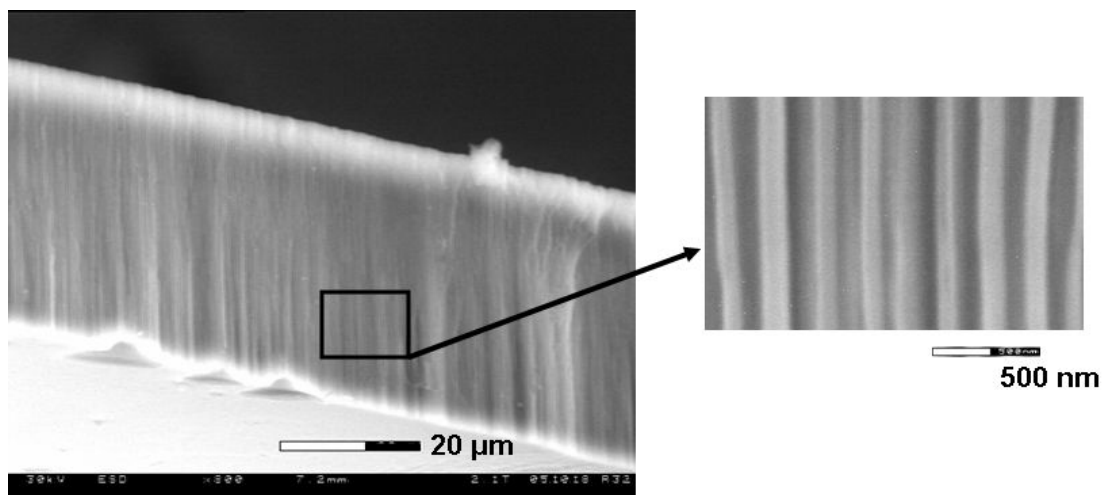


Figure 5.3. ESEM image of the cross section of alumina nanoporous membrane used in this experiment; The highly ordered open pore and capillary structure found with the average diameter of 200 nm and the height of 60 μm .

The PVP solution-trapped nanoporous membrane was transferred into the deionized water-filled container. Then, it was purged with N_2O for 30 min followed by γ -ray irradiation with a total dose of 10 kGy at 25 $^\circ\text{C}$. N_2O was used to double the radiolytic $\bullet\text{OH}$ yield (0.28 to 0.56 $\mu\text{mol J}^{-1}$) by converting e_{aq}^- into $\bullet\text{OH}$ as in the most of this work. Dissolution of the alumina membrane in 10 wt% sodium hydroxide aqueous solutions and consecutive pH adjustment to neutral by washing with excessive deionized water were followed [59]. The schematic representation of experimental procedures is shown in Figure 5.4.

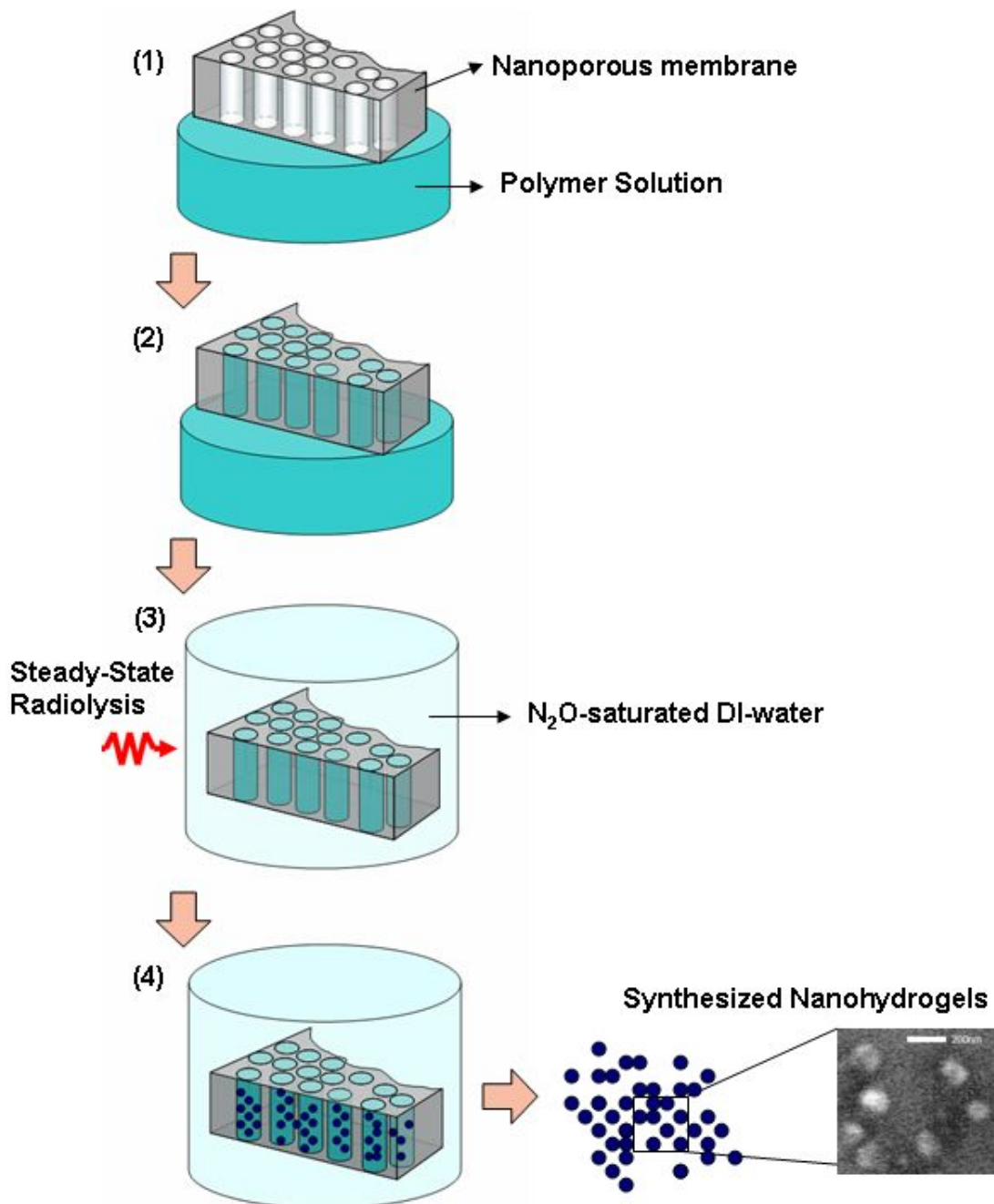
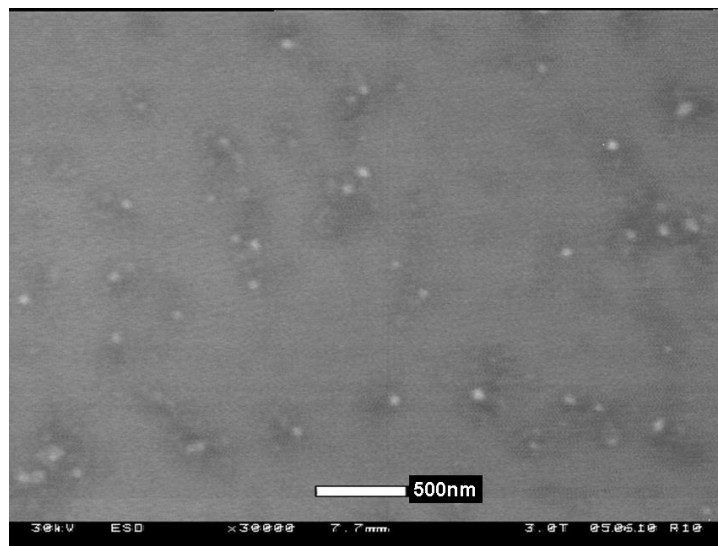


Figure 5.4. Schematic procedure of the template-assisted γ -ray irradiation; contact the nanoporous membrane on PVP aqueous solution (1), introduce solution into the capillaries of the membrane (2), steady-state ionizing radiation (γ -ray) to produce the crosslinked gel structure in trapped PVP within the capillaries of the membrane (3), separate PVP nanohydrogels from membrane by dissolving it in a sodium hydroxide solution (4).

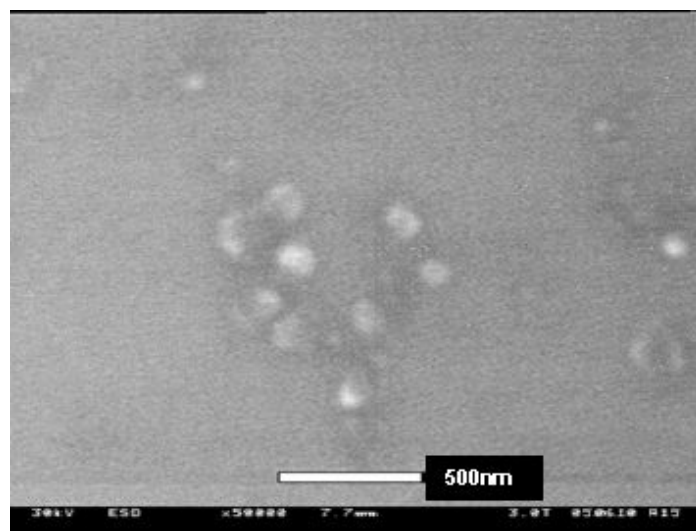
The synthesized PVP sample solution was dropped on the clean glass plate and dried for ESEM analysis. For AFM study, prepared PVP sample was cast on mica substrate and dried at ambient temperature.

Figure 5.5 shows the ESEM images of the prepared PVP gel particles. Due to the limited image contrast and resolution, the particle shape could not be clearly determined as either an individual particle or its agglomerate. However, diameters of the most particles were measured as 90 – 190 nm, which is less than the average diameter of the capillaries of nanoporous membrane. Similar results (particle diameters of 95 – 180 nm) were observed by AFM analysis (Figure 5.6 and 5.7).

To verify the chemical composition and identification of the prepared gel particles, FTIR analyses were performed on both unirradiated and irradiated PVP samples. The results are compared in Figure 5.8. Over all scanned wave number ranges (i.e. 4000 – 400 cm^{-1}), characteristic absorption peaks matched each other confirming that both samples are chemically identical. The spectrum of PVP for both unirradiated and irradiated samples presents the bands at 3020 – 2820 cm^{-1} and 1690 cm^{-1} and also relevant absorptions at 3690 - 3090 cm^{-1} and 2200 – 1900 cm^{-1} . The absorption at 1690 cm^{-1} and in the 3020 – 2820 cm^{-1} range are, in particular, related to the absorption of the carbonyl present in the $>\text{C}(=\text{O})-\text{N}-$ group and to the symmetrical and asymmetrical stretching of C–H in $-\text{CH}_2-$ [93]. The bands in the 3690 – 3090 cm^{-1} and 2200 – 1900 cm^{-1} regions can be attributed to the presence of bound water which was not completely eliminated in drying process [93].



(a)



(b)

Figure 5.5. ESEM micrographs of the synthesized PVP nanohydrogels from N₂O-saturated PVP aqueous solutions ($c = 9 \times 10^{-2} \text{ mol L}^{-1}$) by the nano-template assisted γ -ray irradiation with a dose of 10 kGy at 25 °C; micrograph magnifications are 30,000x (a) and 50,000x (b).

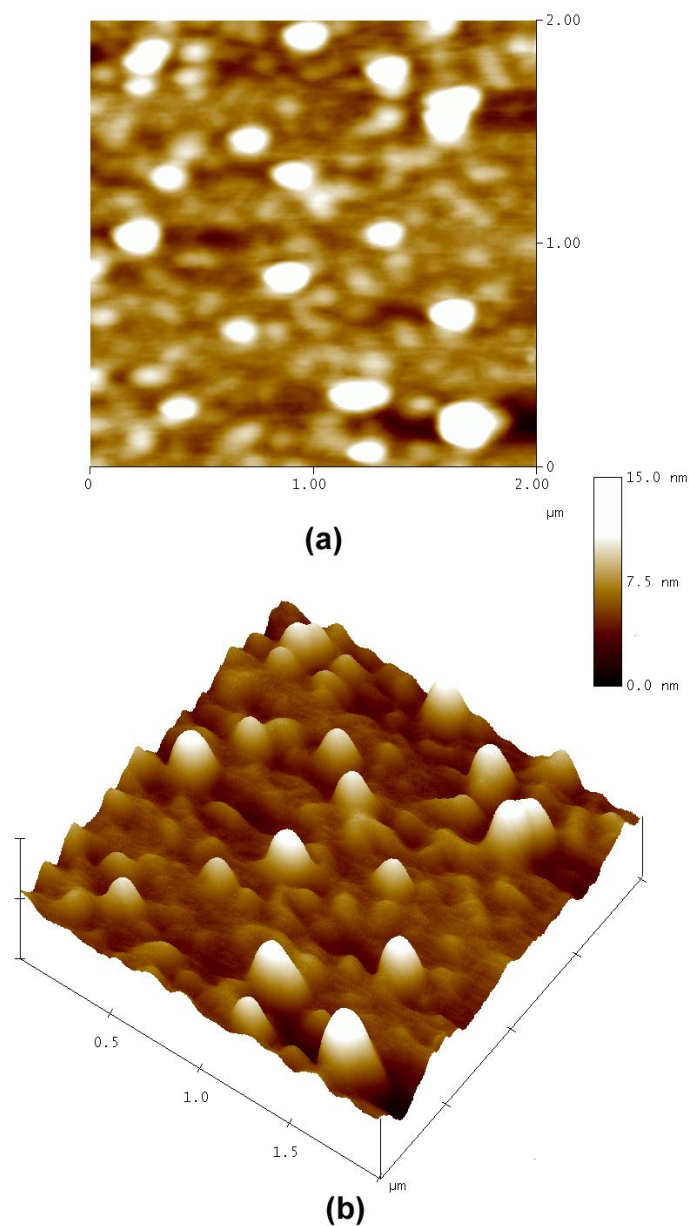


Figure 5.6. AFM micrographs of the synthesized PVP nanohydrogels from N₂O-saturated PVP aqueous solutions ($c = 9 \times 10^{-2} \text{ mol L}^{-1}$) by the nano-template assisted γ -ray irradiation with a dose of 10 kGy at 25 °C: planar view (a) and 3D view (b) (scanned area = 2 x 2 μm for both pictures).

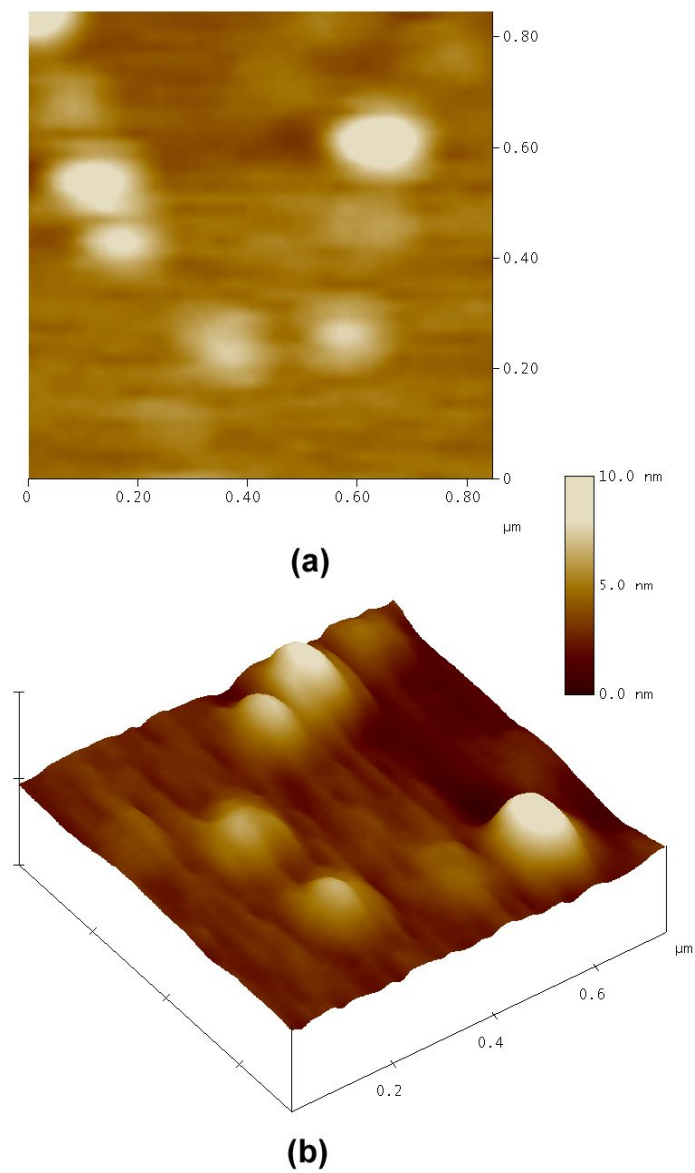


Figure 5.7. AFM micrographs of the synthesized PVP nanohydrogels from N₂O-saturated PVP aqueous solutions ($c = 9 \times 10^{-2} \text{ mol L}^{-1}$) by the nano-template assisted γ -ray irradiation with a dose of 10 kGy at 25 °C: planar view (a) and 3D view (b) (scanned area = 0.85 x 0.85 μm (a), 0.8 x 0.8 μm (b)).

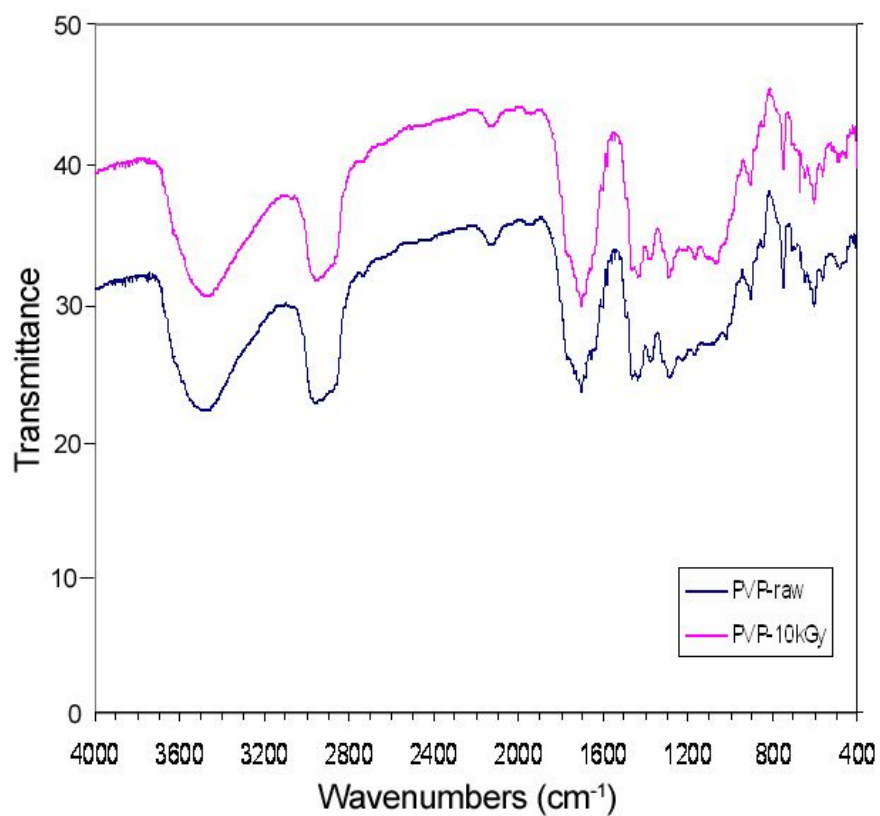


Figure 5.8. FTIR spectra of the unirradiated (PVP-raw) PVP and the synthesized nanohydrogels from N₂O-saturated PVP aqueous solutions ($c = 9 \times 10^{-2} \text{ mol L}^{-1}$) by the nano-template assisted γ -ray irradiation with a dose of 10 kGy at 25 °C (PVP-10kGy).

5.3 Discussion and conclusions

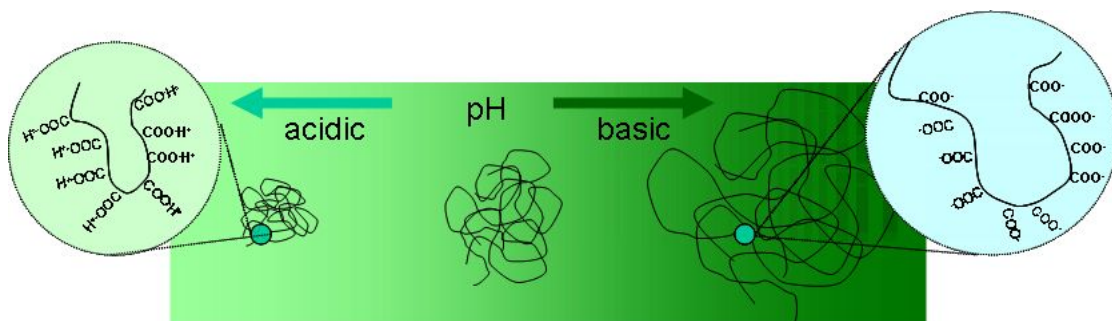
Nanotemplate-assisted ionizing radiation was firstly implemented to synthesize PVP hydrogel nanoparticles. Highly ordered cylindrical capillary pore structure in the nanoporous membrane gives the spatial isolation of polymer chains and promotes PVP radical-radical reactions only within the molecules in the same capillary pore. Size of the synthesized PVP gel particles, therefore, is determined by the physical dimension of nano-capillary pore structure. Depending on the pore diameter, shape, and surface chemistry of the nanoporous template, synthesized gels are expected to have different size, molecular weight, shape, and morphology. Irradiation dose is expected to determine the number of crosslinking bonds formed in the gels. Thereby crosslinking density, molecular weight, and size of product are expected to be varied. Concentration of PVP aqueous solution is also expected to affect the shape of the final gel product. The pervaded volume of each PVP chain starts to overlap one another at higher solution concentration (i.e., above overlap concentration), promoting inter-molecular carbon radical-radical crosslinking reactions upon ionizing radiation. Throughout this reaction, the size and molecular weight of the product are expected to increase if competing reactions (e.g., scission on the polymer backbone) are suppressed. If concentration of solution is high enough, polymer gel tube (or wire) is expected to be produced rather than discrete gel particles. The corresponding physical properties (e.g., porosity, crosslinking density, modulus, etc.) of the synthesized hydrogels are also expected to be varied.

Chapter 6:

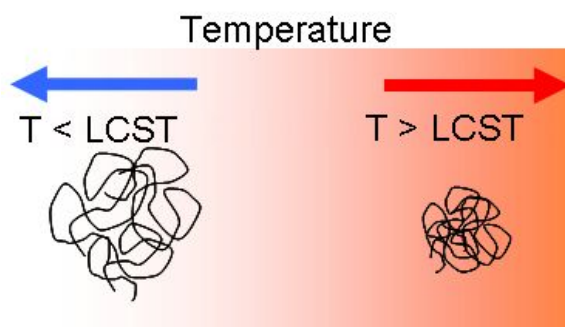
RECOMMENDATION FOR FUTURE WORKS

6.1 Stimuli-responsive nanohydrogels

It has been reported that some chemically composed hydrogels can respond (e.g., shrink or swell) to the change of environments, such as temperature, pH, ionic strength, and magnetic/electric field. Nanohydrogels can respond to the external stimuli much faster than the macroscopic hydrogels due to the smaller relaxation time (e.g., fast diffusion process) derived from their smaller dimensions [10]. pH- and temperature-responsive nanohydrogels will be synthesized by means of pulsed electron beam with different conditions (e.g., pH, temperature, pulse repetition rate, etc.) and their responses to the external stimuli changes will be characterized in terms of particle diameter. The response rate of crosslinked nanohydrogels is probably lower than that of the linear chains due to the restricted conformations caused by internal crosslinks of gel structure. Highly crosslinked nanohydrogels are expected to respond slower than non-or low-crosslinked system. Tests will be carried out in parallel using both linear chains and nanohydrogels. Poly(acrylic acid) (PAA) and poly(N-isopropyl acryl amide) (pNIPAAm) will be studied as the pH- and temperature-sensitive system respectively (Figure 6.1).



(a)



(b)

Figure 6.1. Schematics of the stimuli-responsive nanohydrogels: pH-responsive poly(acrylic acid), PAA (a), temperature-responsive poly(N-isopropyl acrylamide), pNIPAAm (b); LCST stands for lower critical solution temperature.

The kinetics of polymer radical-radical recombination to form inter- and intra-crosslinks in each system will be carried out by pulse radiolysis technique at various pH and temperature conditions. DLS and AFFF chromatography will be used to measure the conformation and the molecular weight of the products.

6.2 Magnetic nanoparticles embedded hydrogels

Polymer hydrogels with the magnetic properties have been developed using non-radiation methods [94, 95]. Magnetic nanohydrogel (i.e., ferrogel) is interesting material because it deforms under magnetic field [94, 96, 97]. This unique property can be applied in the magnetic field driven drug release, artificial muscles, nano actuators, etc. The dimension of polymer macroscopic gels embedded with fine magnetic particles is able to be controlled by magnetic field [98].

For future work, ionizing radiation by pulsed electron beam will be incorporated into the ferrogel synthesis and effect of metal precipitates on the recombination of carbon-centered radicals will be studied. Aqueous solutions of metal salts will be used as the source of magnetic material. Magnetic nanoparticles will be introduced into the nanohydrogel matrix by means of complex formation between metal ions and polymer. Previous FTIR studies showed the complex formation of PVP with metal ion (e.g., Ag^+) [99, 100]; The shift of C=O absorption band at ca. 1660 cm^{-1} was found due to the interactions between metal ions and the carbonyl group in PVP. Fe_3O_4 nanoparticles may be produced from hydrates of FeCl_3 and FeSO_4 mixture with the reaction of potassium hydroxide [98]. The crystalline structure of Fe_3O_4 will be analyzed by X-ray diffraction. The morphology and diameter of synthesized Fe_3O_4 within polymer nanohydrogels will be analyzed by transmission electron microscopy.

6.3 Nanohydrogels prepared by nano-phase separation

Another feasible method to prepare nanoscopic hydrogels is based on the nano-phase separation in the miscible solvents system. Acetone and water mixture is one of the mixed solvent systems which are miscible but rapidly separate the phase at certain mixing ratio. Using this phenomenon, polymer nanogel particles can be synthesized by ionizing radiation-induced crosslinking reactions which only occur to the dissolved hydrophilic polymers in water. Unlike other micro-emulsion process [13, 14], emulsifier or surfactant is not required. By controlling the relative mixing ratio of the solvents, size of the synthesized hydrogel particles is expected to be varied. In a mixture of miscible solvents (e.g., water and acetone), solvent molecules attract one each other at any concentration of molecules and it can be described by Kirkwood-Buff integrals G_{ij} [101] as given by following equation:

$$G_{ij} = \int_0^{\infty} (g_{ij} - 1)4\pi r^2 dr \quad (6.1)$$

where g_{ij} is the radial distribution function which can be described as the change of the density of the molecules j which surrounds a molecule i as a function of the distance. Previous studies shows that water molecules have maximum G_{ij} due to the preferred water-water interaction (G_{11}) [102, 103]. Water tend to self-aggregate with maximum degree at around composition of 0.5 mole fraction in the mixture of acetone and water (Figure 6.2) [102, 103]. By simple changes of the relative ratio of water-acetone mixture, size of water-water aggregates can be varied.

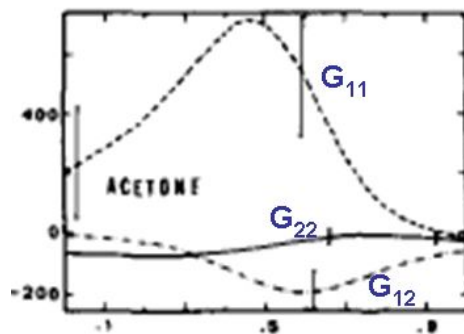


Figure 6.2. G_{ij} functions vs. the mole fraction of water x_1 for water (1) – organic component (2) (i.e., acetone) mixtures at 25 °C [102].

Water soluble (insoluble in acetone) polymers such as PVP can be confined into the water aggregates (due to its selective solubility) and is expected to become gel-structure by ionizing radiation-induced inter- and intra-crosslinking bonds. Size of the synthesized product is expected to be dependent upon water aggregates size.

Based on this idea, a preliminary experiment was carried out with following procedure; 50g of 1 wt% (equivalent to $9 \times 10^{-2} \text{ mol L}^{-1}$) PVP ($M_w = (3.94 \pm 0.12) \times 10^5 \text{ g mol}^{-1}$) aqueous solution was added to 27g of acetone. The x_1 is about 0.85. PVP aqueous solution-acetone mixture was then saturated with N_2O to increase the radiolytic yield of $\bullet\text{OH}$ as shown in reaction (2.14). The mixture was irradiated by γ -ray with 10 kGy dose to produce crosslinked gel structures in PVP. Figure 6.3 shows the distribution of R_h of prepared sample. The average R_h was measured as 98 ± 5 nm and showed mono-disperse distribution of particle size. Despite the relatively high concentration ($9 \times 10^{-2} \text{ mol L}^{-1}$) of PVP aqueous solution, the final product still retained its original liquid phase without forming macroscopic gel structure.

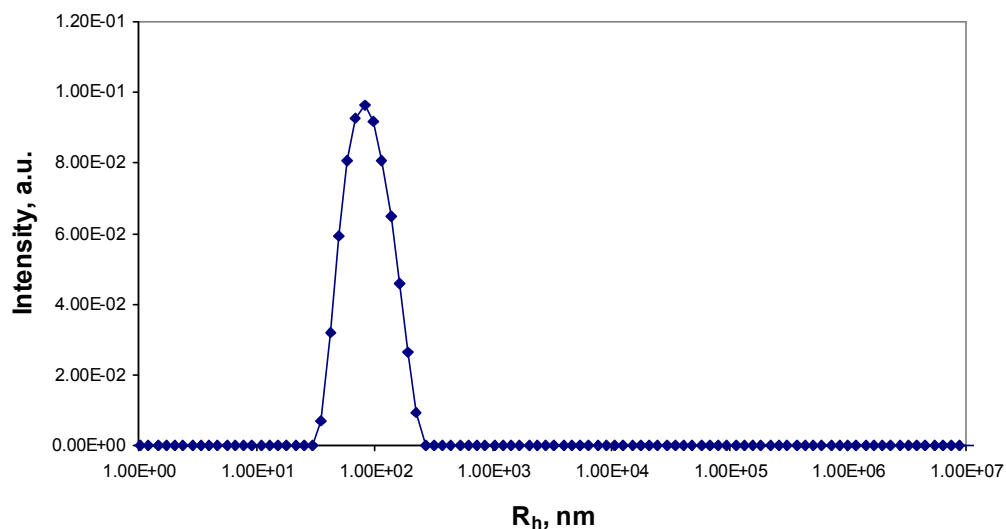


Figure 6.3. R_h distribution (with average $R_h = 98 \pm 5$ nm) of the PVP nanohydrogels synthesized by nano-phase separation technique; total irradiated dose = 10 kGy, 9×10^{-2} mol L⁻¹ PVP in water/acetone mixture.

The further investigations will be carried out based on the preliminary result. Effects of the synthesis parameters (e.g., irradiation temperature, dose, dose rate, etc.) on the molecular weight distributions and surface morphologies of the polymer gel products will be studied.

6.4 Gel nanoparticles network

Macroscopic gel structure made with nanohydrogel particles is expected to be an interesting material for its unique properties including high surface area and the stimuli-tunable heterogeneity which bulk gels do not have. By combining two or more types of stimuli-responsive nanohydrogels into a single macroscopic matrix, multi-functional gel materials may be produced for specific applications [104]. However, previous works are based on the classical crosslinking process using toxic crosslinking agents and requires many auxiliary steps [104]. Ionizing radiation is a good alternative method to interlink different types of nanohydrogel particles into a single macroscopic gel matrix (i.e., gel nanoparticles network) by inter-molecular crosslinking reactions. The hierarchical structure of gel nanoparticle network is shown in Figure 6.4. Various formulations with different types of nanohydrogels (e.g., pH-responsive, temperature-responsive, adhesive, and magnetic nanohydrogels) will be used to produce gel nanoparticle networks and their multi-functional properties will be tested (Figure 6.5).

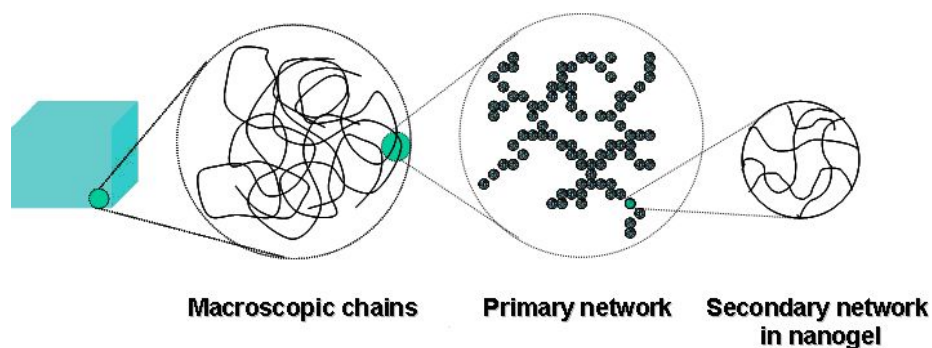


Figure 6.4. The hierarchical structure of the gel nanoparticles network.

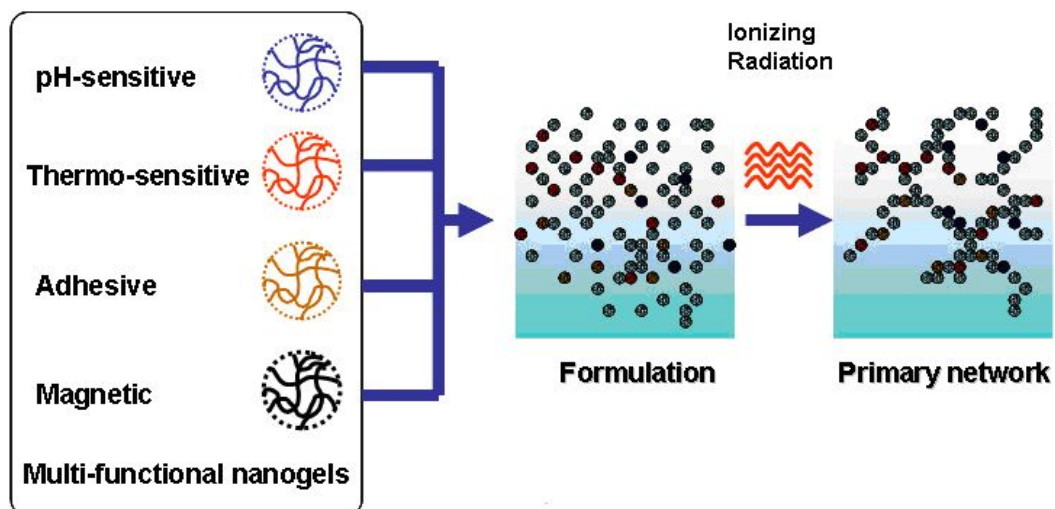


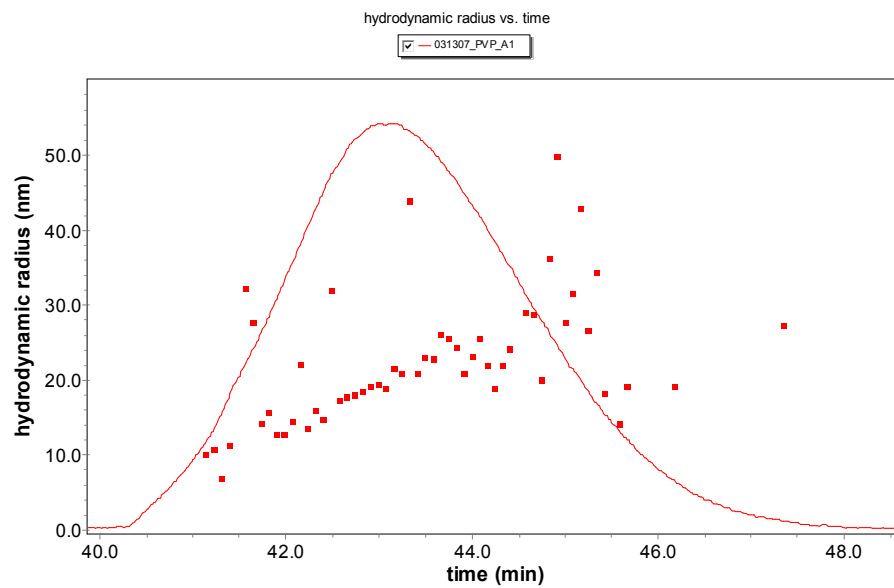
Figure 6.5. The synthesis route for the multi-functional and multi-component gel nanoparticles network.

The physical/chemical properties of the gel nanohydrogel particle network and the conventional macroscopic gel (i.e., crosslinked gel composed of linear polymer chains with a same chemical composition) will be compared. Surface morphology also will be investigated by AFM.

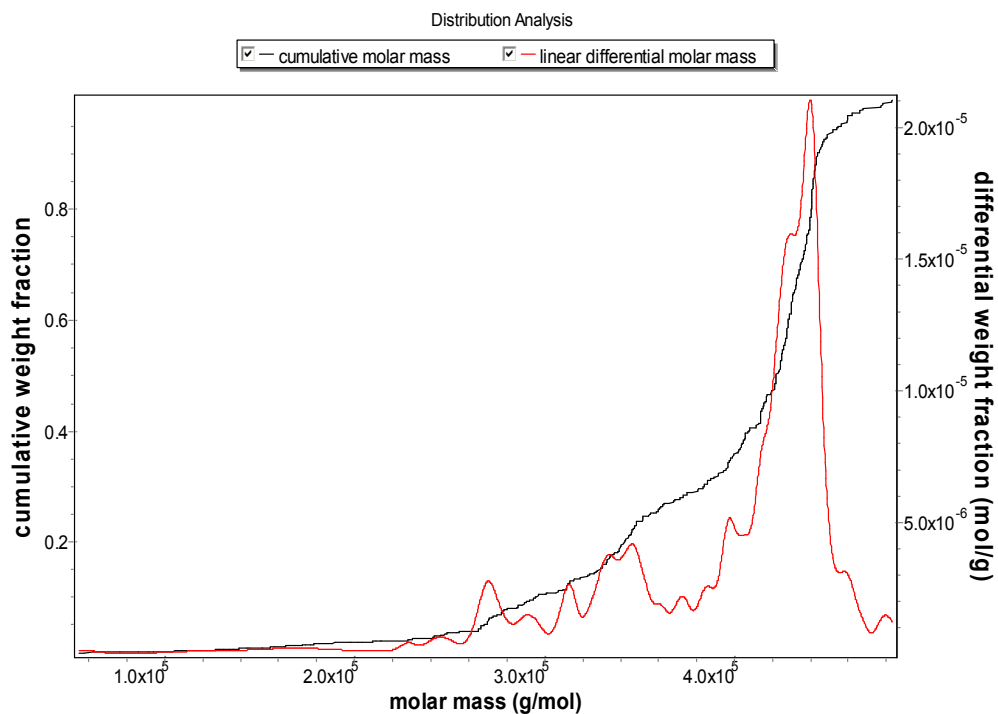
Appendix

AFFFF results of the PVP nanohydrogels

As extended AFFFF analysis works, (1) the plots of the elute time and R_h distribution range and (2) the plots of the cumulative and linear differential molar weight distribution of PVP nanohydrogels prepared at various synthesis conditions are represented.

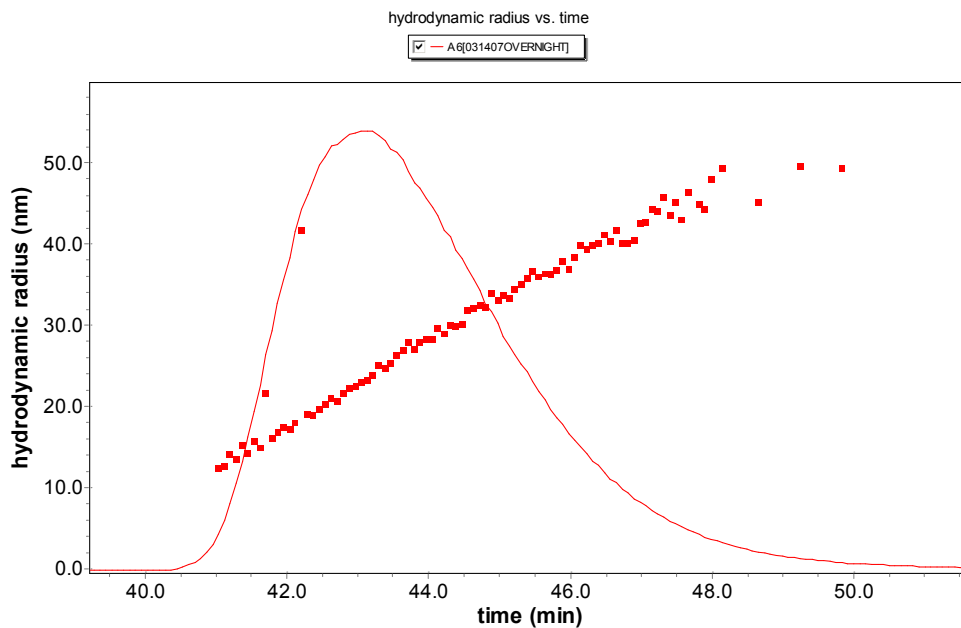


(a)

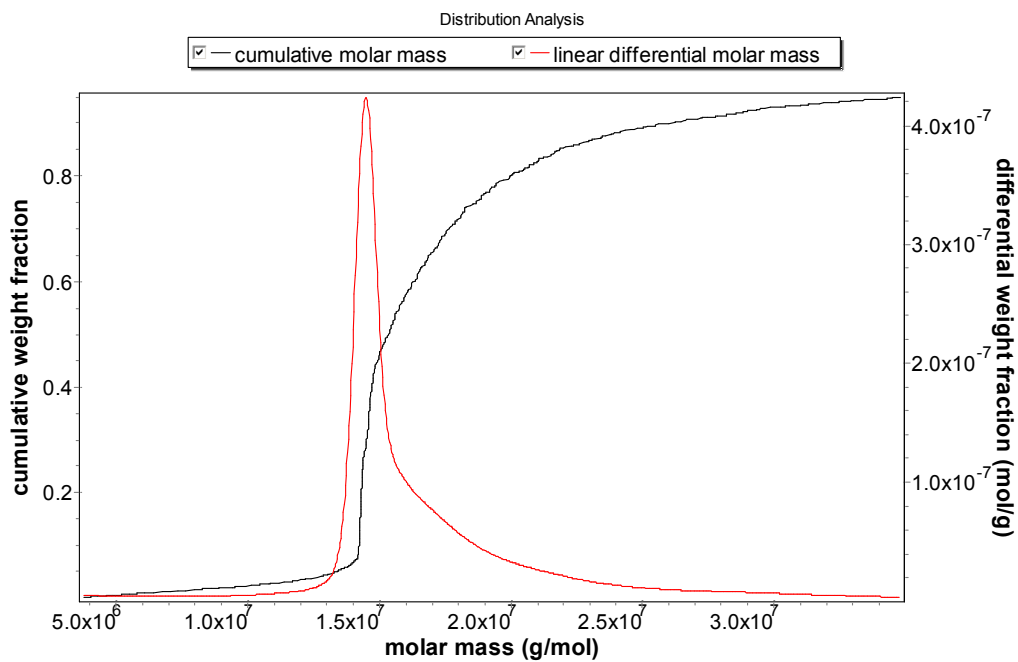


(b)

Figure 1.1. Elution and R_h diagram (a), distribution analysis of the cumulative molar mass and linear differential molar mass (b) of unirradiated PVP aqueous solution ($c = 0.9 \times 10^{-2} \text{ mol L}^{-1}$).

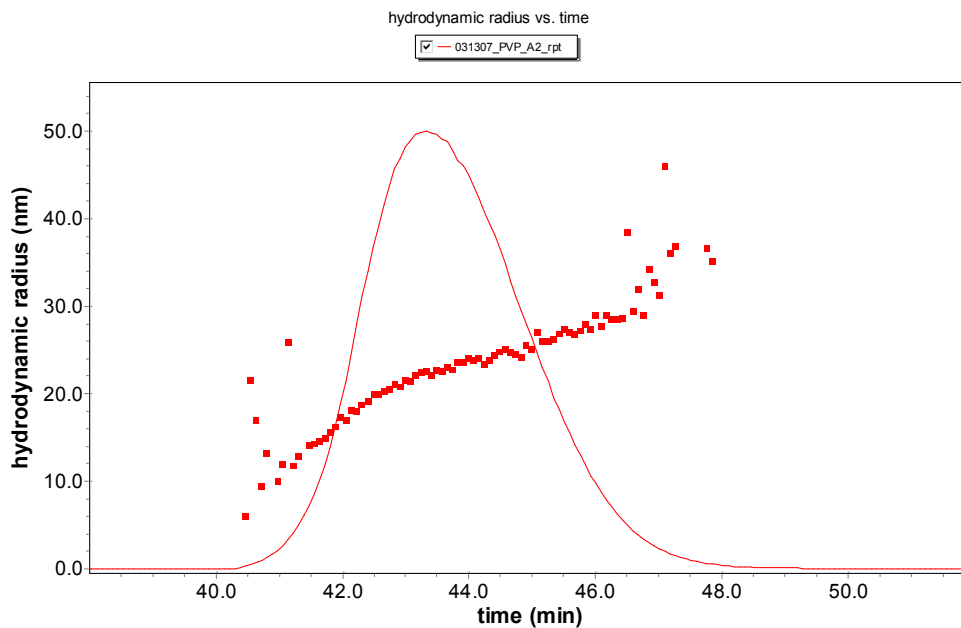


(a)

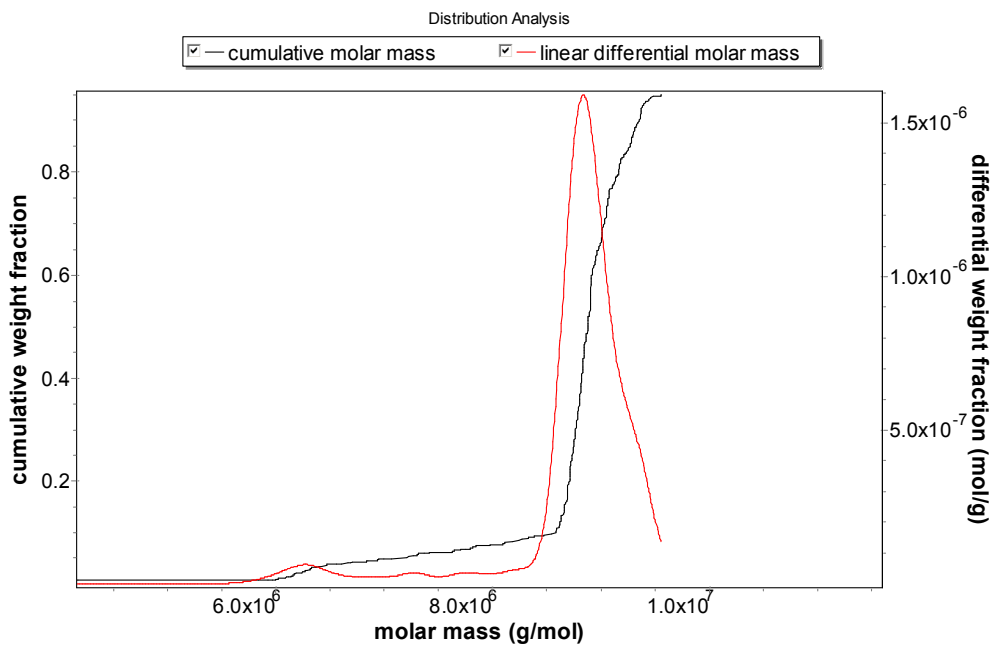


(b)

Figure 1.2. Elution and R_h diagram (a), distribution analysis of the cumulative molar mass and linear differential molar mass (b) of the synthesized PVP nanohydrogels ($c = 0.9 \times 10^{-2} \text{ mol L}^{-1}$) with e-beam irradiation of 10 kGy at 20°C (pulse repetition rate = 20 Hz).



(a)



(b)

Figure 1.3. Elution and R_h diagram (a), distribution analysis of the cumulative molar mass and linear differential molar mass (b) of the synthesized PVP nanohydrogels ($c = 0.9 \times 10^{-2} \text{ mol L}^{-1}$) with e-beam irradiation of 10 kGy at 20°C (pulse repetition rate = 300 Hz).

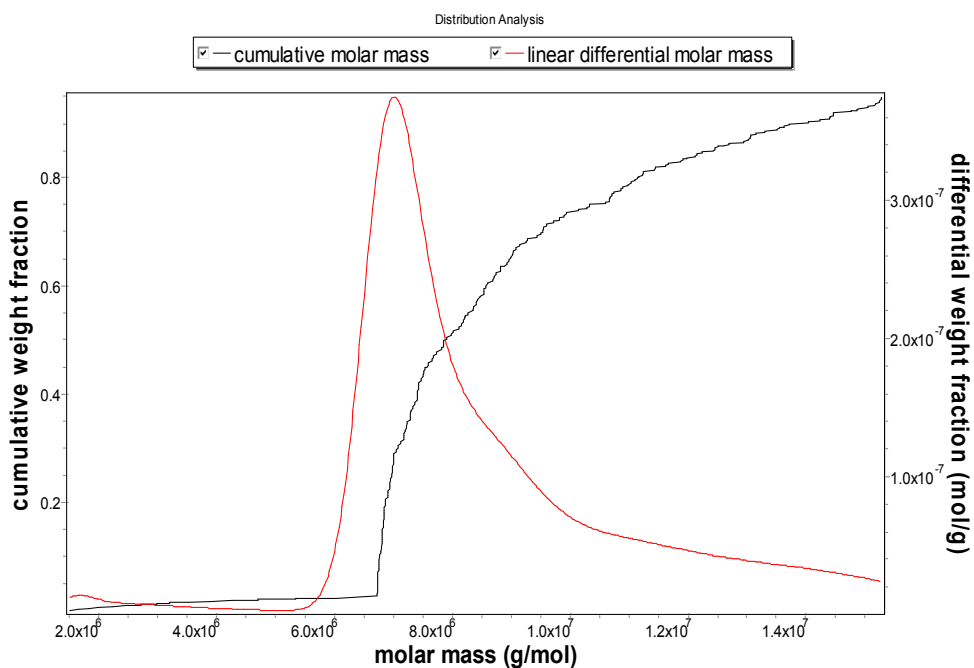
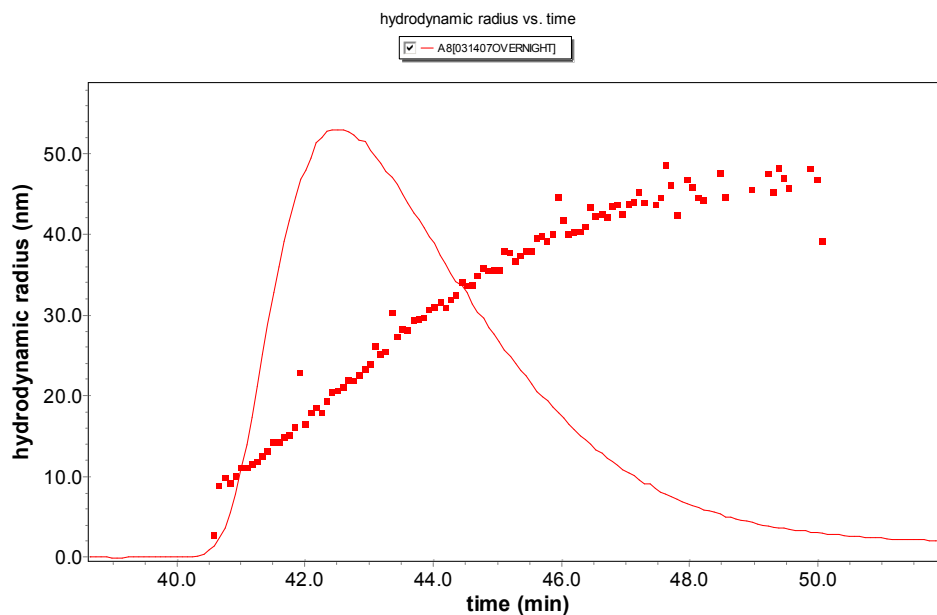
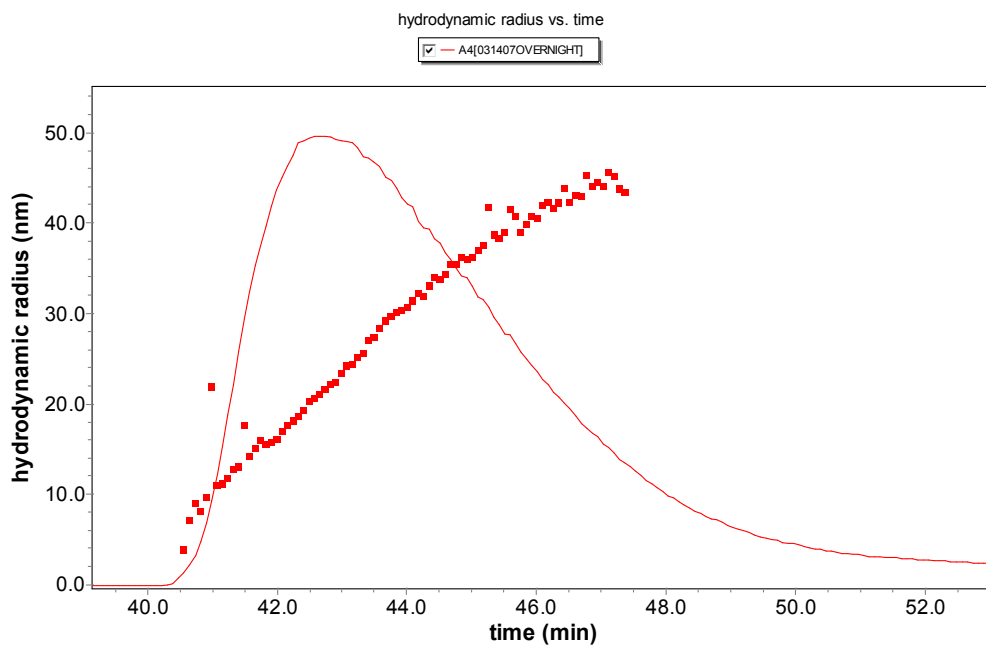
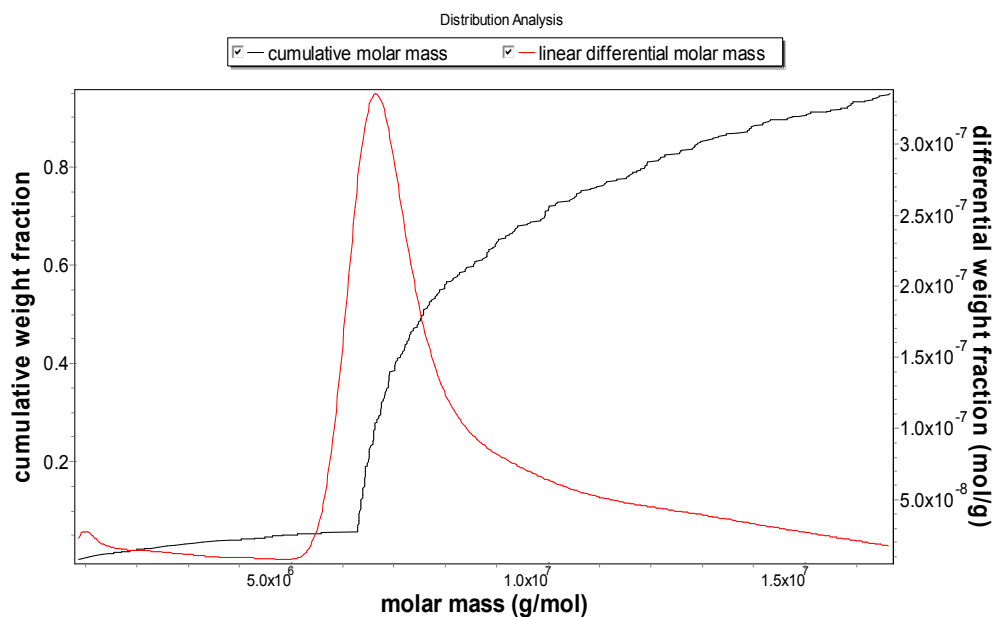


Figure 1.4. Elution and R_h diagram (a), distribution analysis of the cumulative molar mass and linear differential molar mass (b) of the synthesized PVP nanohydrogels ($c = 0.9 \times 10^{-2} \text{ mol L}^{-1}$) with e-beam irradiation of 5 kGy at 20°C (pulse repetition rate = 20 Hz).

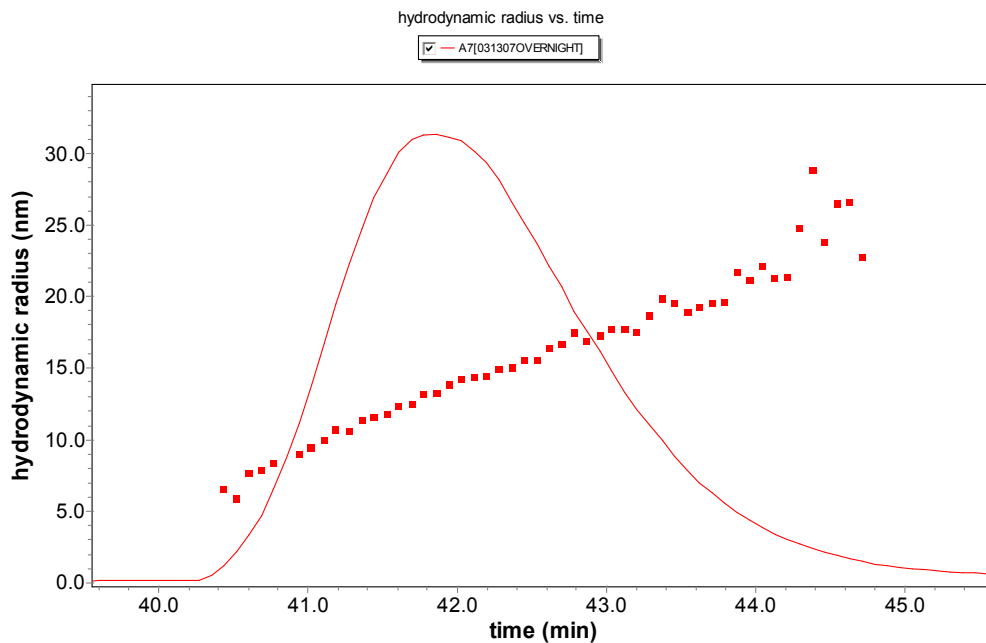


(a)

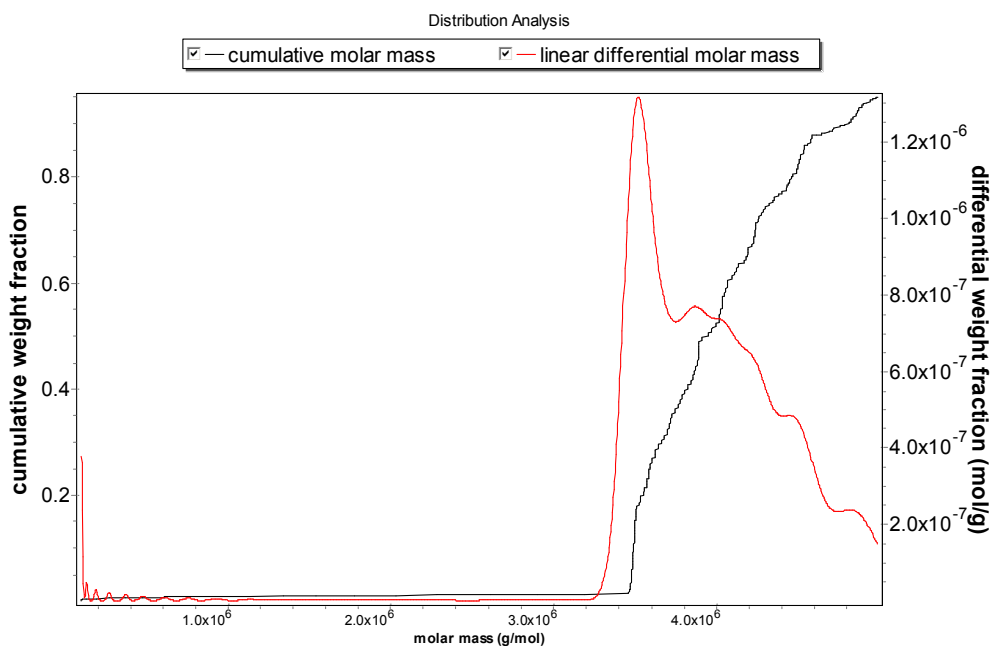


(b)

Figure 1.5. Elution and R_h diagram (a), distribution analysis of the cumulative molar mass and linear differential molar mass (b) of the synthesized PVP nanohydrogels ($c = 0.9 \times 10^{-2} \text{ mol L}^{-1}$) with e-beam irradiation of 10 kGy at 20°C (pulse repetition rate = 300 Hz).

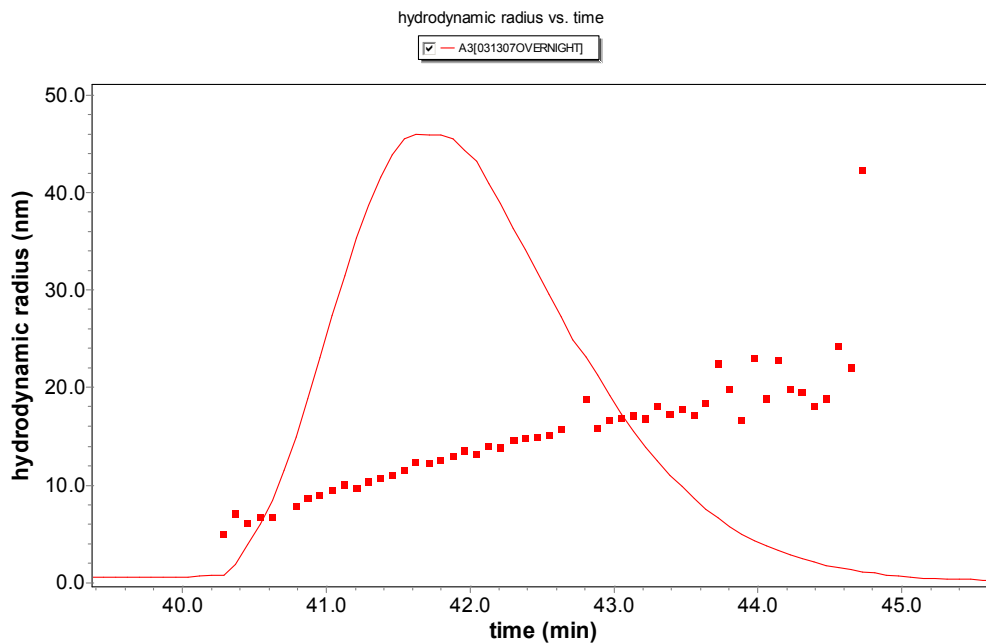


(a)

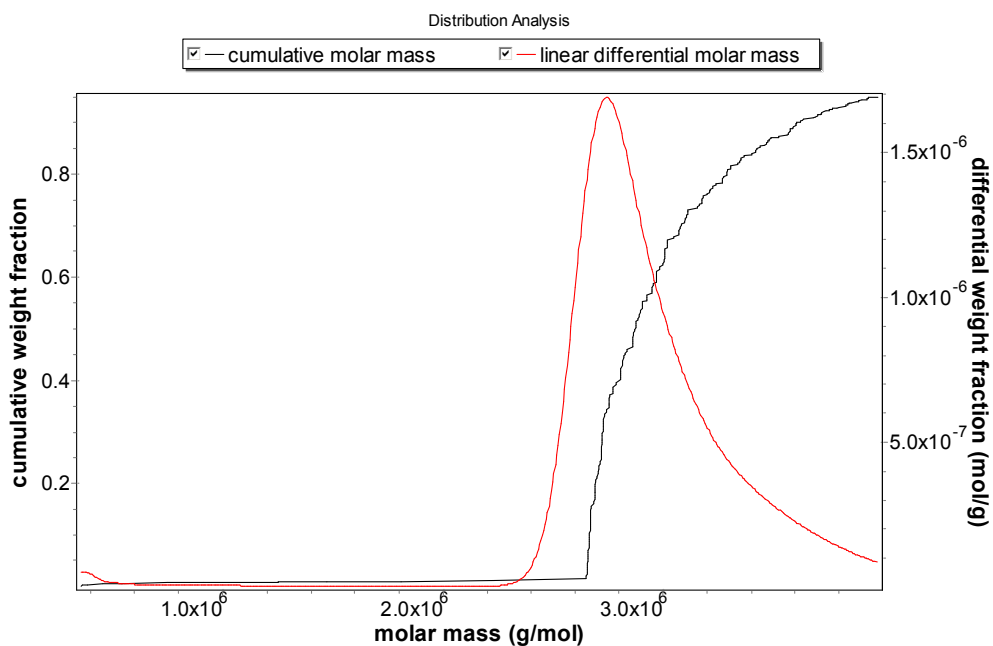


(b)

Figure 1.6. Elution and R_h diagram (a), distribution analysis of the cumulative molar mass and linear differential molar mass (b) of the synthesized PVP nanohydrogels ($c = 0.9 \times 10^{-2} \text{ mol L}^{-1}$) with e-beam irradiation of 5 kGy at 60°C (pulse repetition rate = 20 Hz).

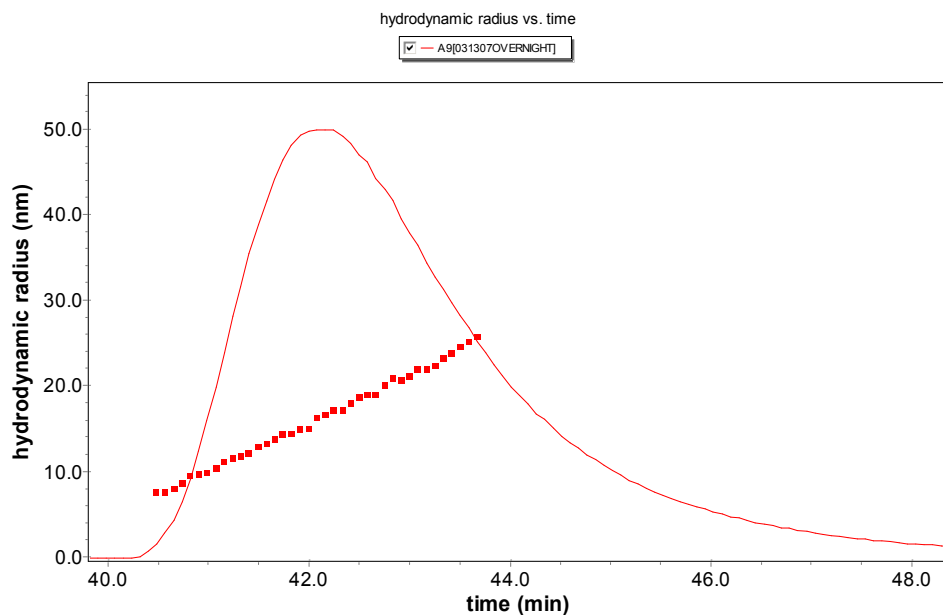


(a)

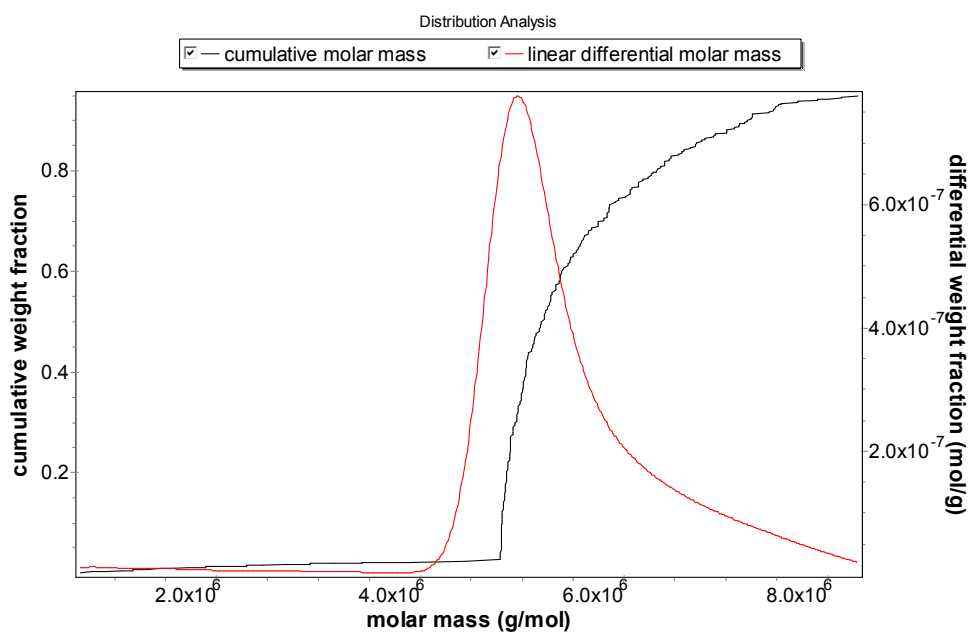


(b)

Figure 1.7. Elution and R_h diagram (a), distribution analysis of the cumulative molar mass and linear differential molar mass (b) of the synthesized PVP nanohydrogels ($c = 0.9 \times 10^{-2} \text{ mol L}^{-1}$) with e-beam irradiation of 5 kGy at 60°C (pulse repetition rate = 300 Hz).

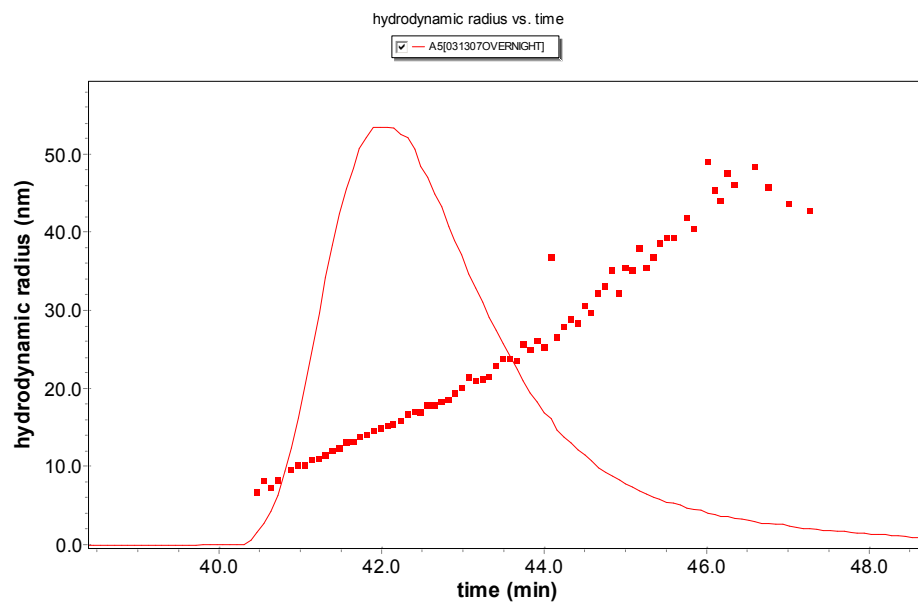


(a)

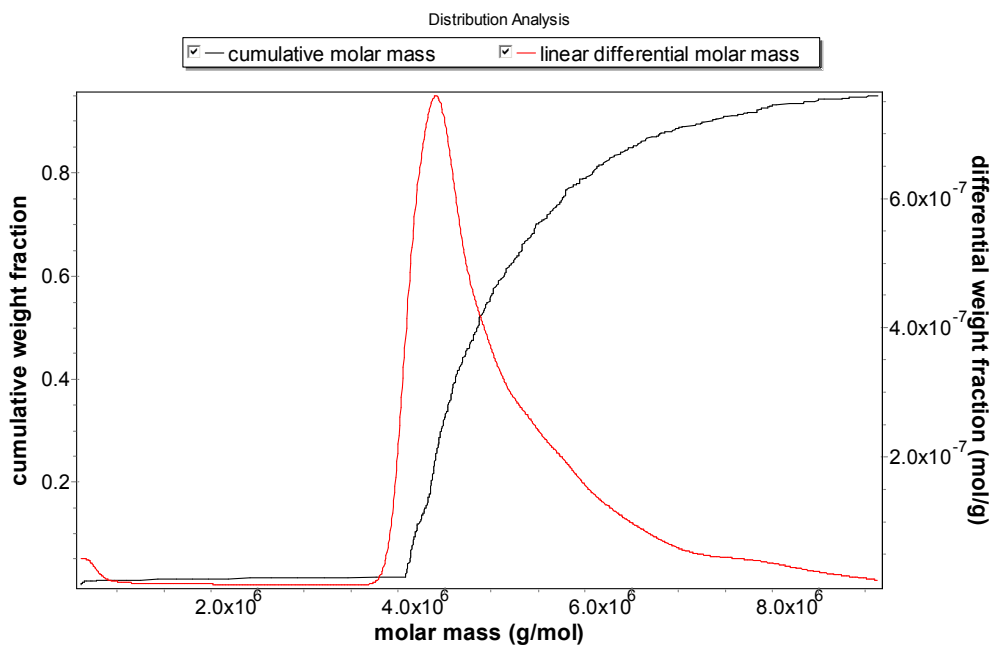


(b)

Figure 1.8. Elution and R_h diagram (a), distribution analysis of the cumulative molar mass and linear differential molar mass (b) of the synthesized PVP nanohydrogels ($c = 0.9 \times 10^{-2} \text{ mol L}^{-1}$) with e-beam irradiation of 10 kGy at 60°C (pulse repetition rate = 20 Hz).

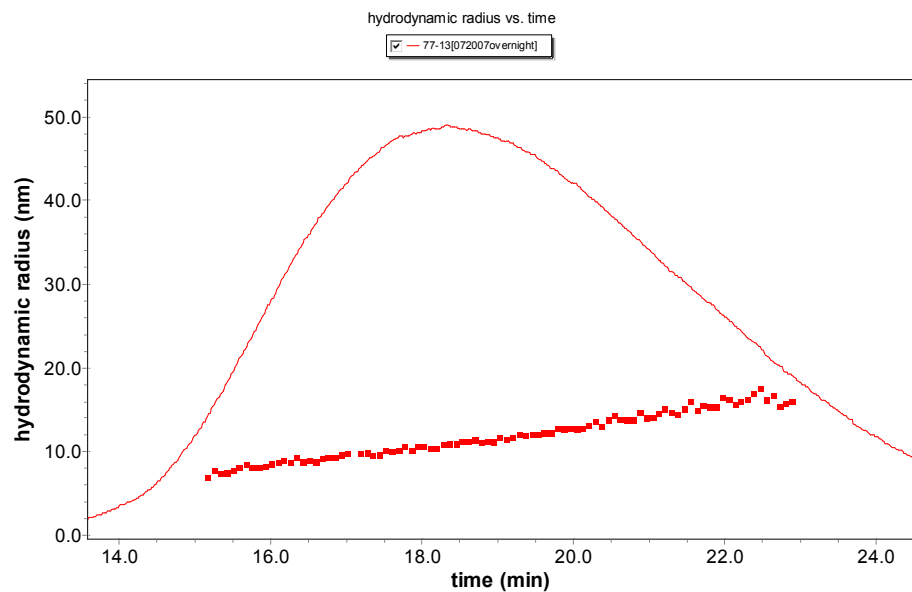


(a)

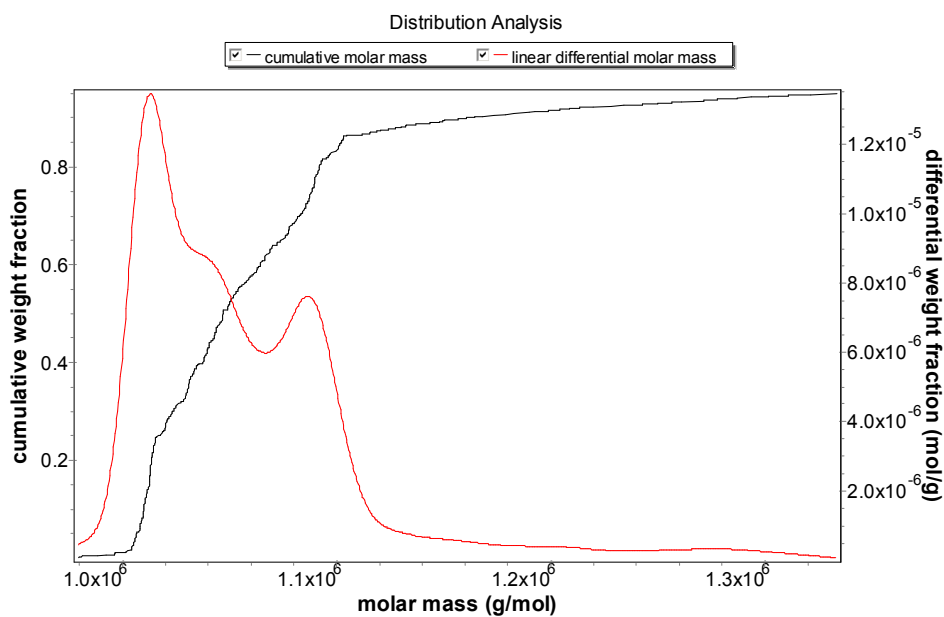


(b)

Figure 1.9. Elution and R_h diagram (a), distribution analysis of the cumulative molar mass and linear differential molar mass (b) of the synthesized PVP nanohydrogels ($c = 0.9 \times 10^{-2} \text{ mol L}^{-1}$) with e-beam irradiation of 10 kGy at 60°C (pulse repetition rate = 300 Hz).

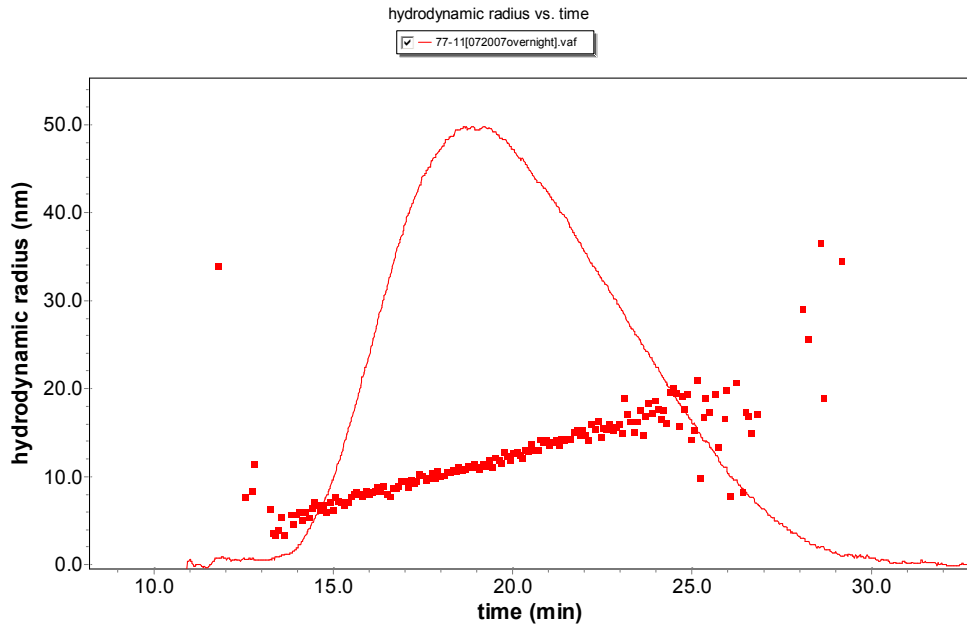


(a)

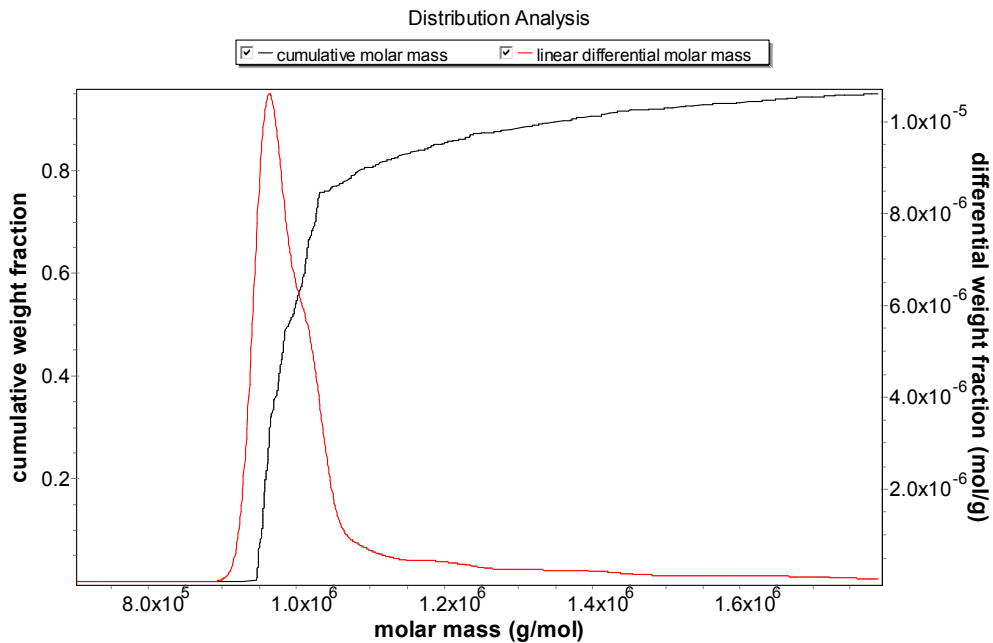


(b)

Figure 1.10. Elution and R_h diagram (a), distribution analysis of the cumulative molar mass and linear differential molar mass (b) of the synthesized PVP nanohydrogels ($c = 0.9 \times 10^{-2} \text{ mol L}^{-1}$) with e-beam irradiation of 10 kGy at 77 °C (pulse repetition rate = 20 Hz).

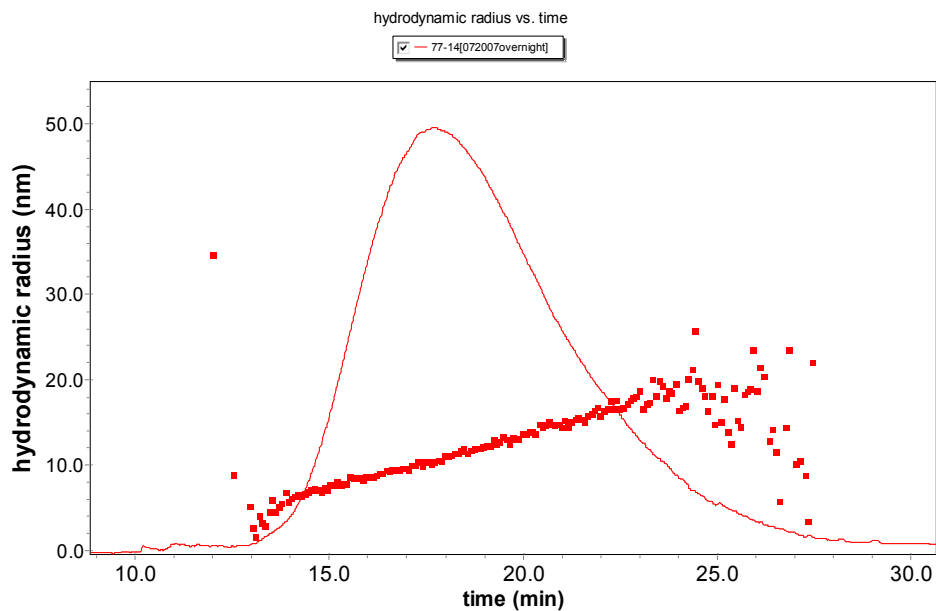


(a)

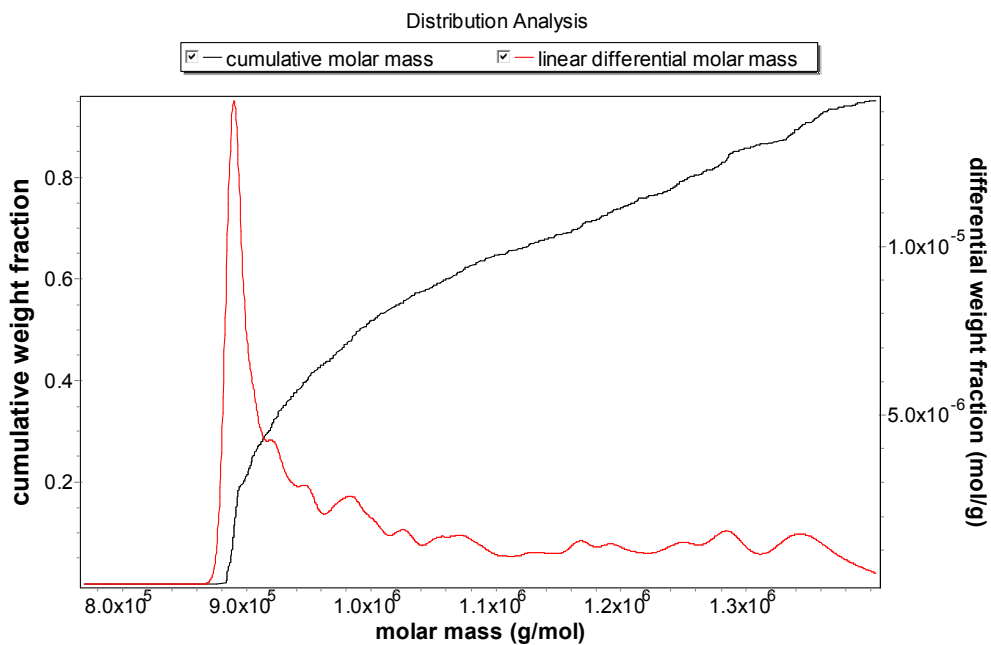


(b)

Figure 1.11. Elution and R_h diagram (a), distribution analysis of the cumulative molar mass and linear differential molar mass (b) of the synthesized PVP nanohydrogels ($c = 0.9 \times 10^{-2} \text{ mol L}^{-1}$) with e-beam irradiation of 10 kGy at 77 °C (pulse repetition rate = 300 Hz).

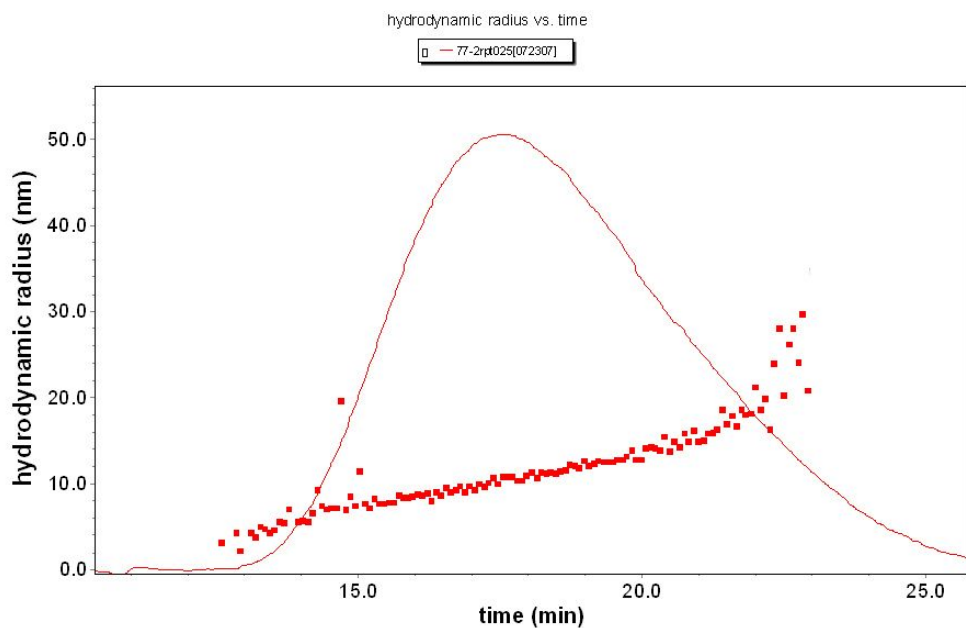


(a)

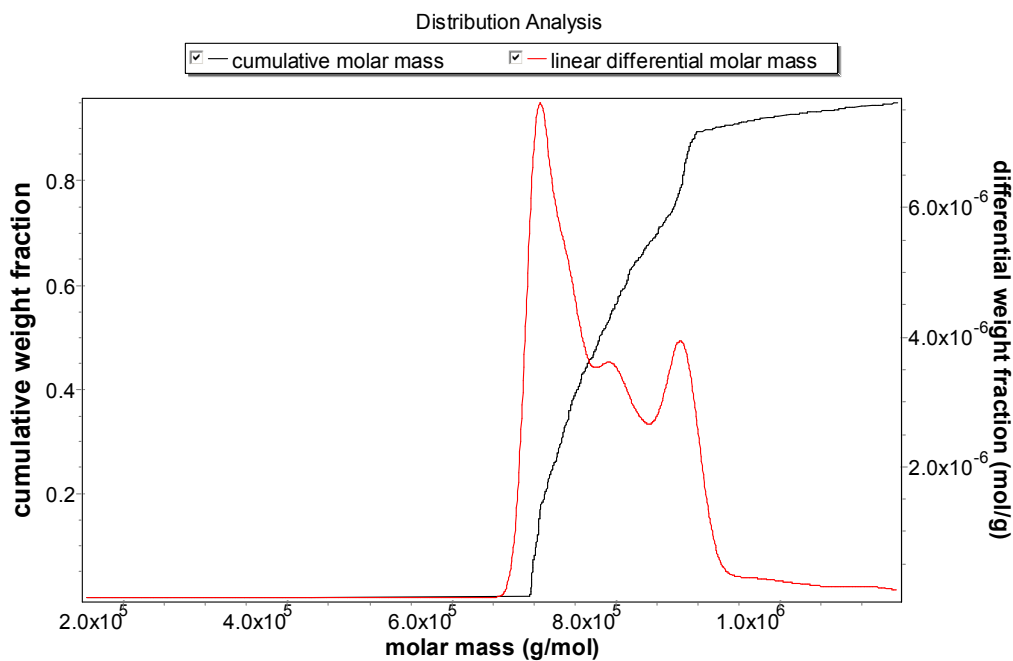


(b)

Figure 1.12. Elution and R_h diagram (a), distribution analysis of the cumulative molar mass and linear differential molar mass (b) of the synthesized PVP nanohydrogels ($c = 0.9 \times 10^{-2} \text{ mol L}^{-1}$) with e-beam irradiation of 5 kGy at 77 °C (pulse repetition rate = 20 Hz).

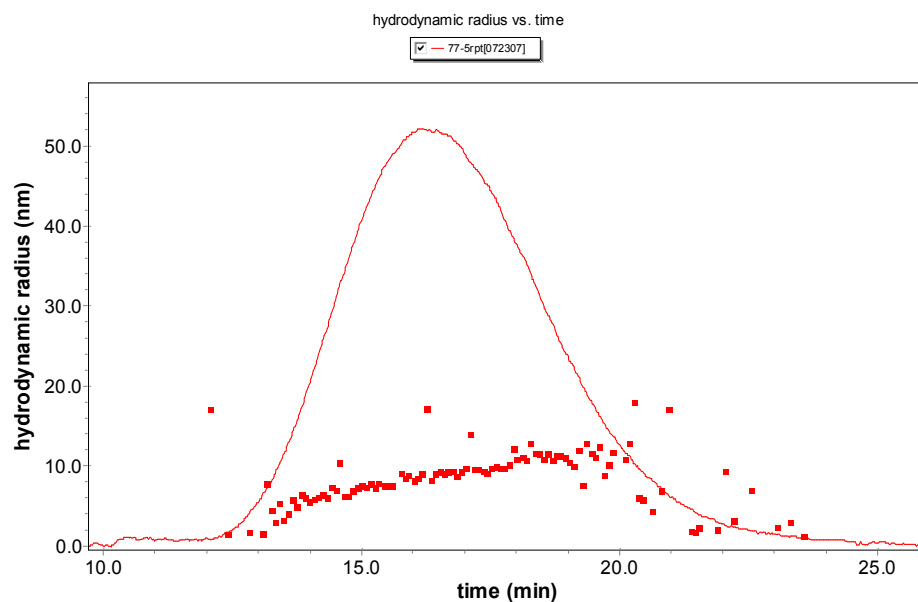


(a)

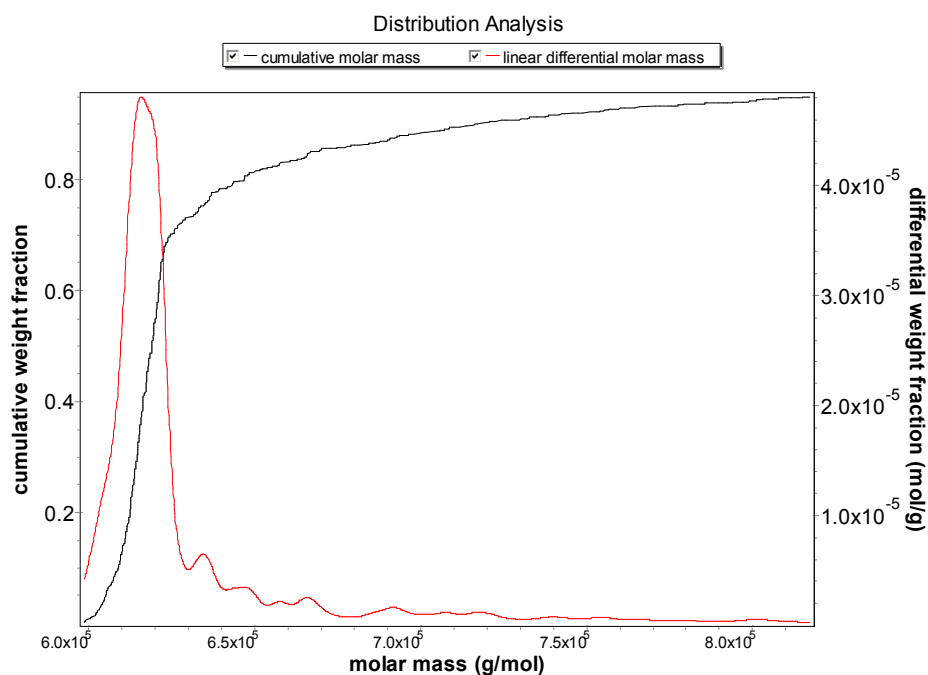


(b)

Figure 1.13. Elution and R_h diagram (a), distribution analysis of the cumulative molar mass and linear differential molar mass (b) of the synthesized PVP nanohydrogels ($c = 0.9 \times 10^{-2} \text{ mol L}^{-1}$) with e-beam irradiation of 5 kGy at 77 °C (pulse repetition rate = 300 Hz).

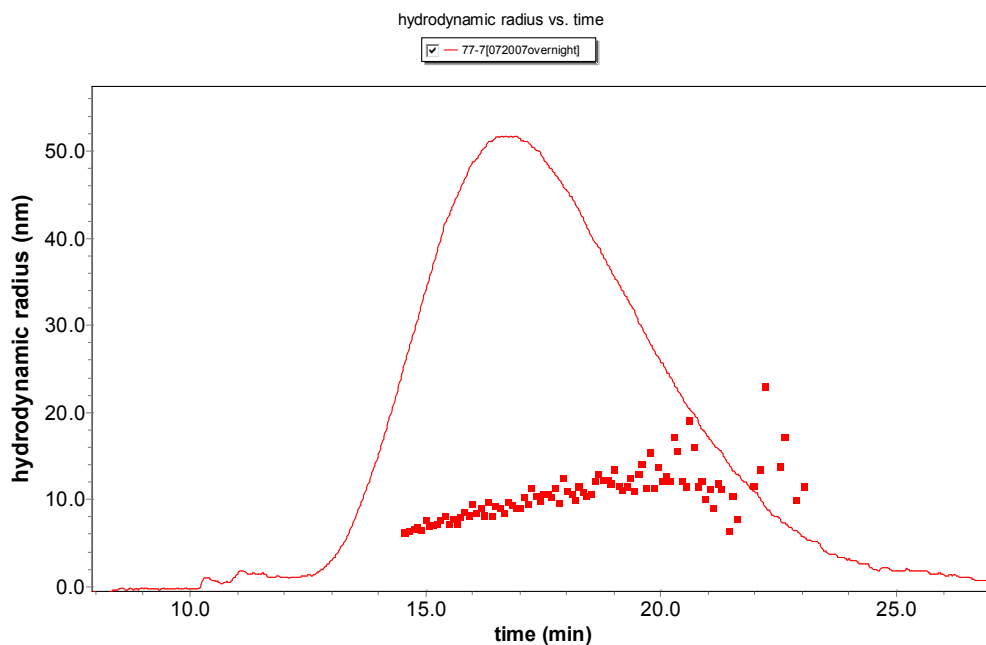


(a)

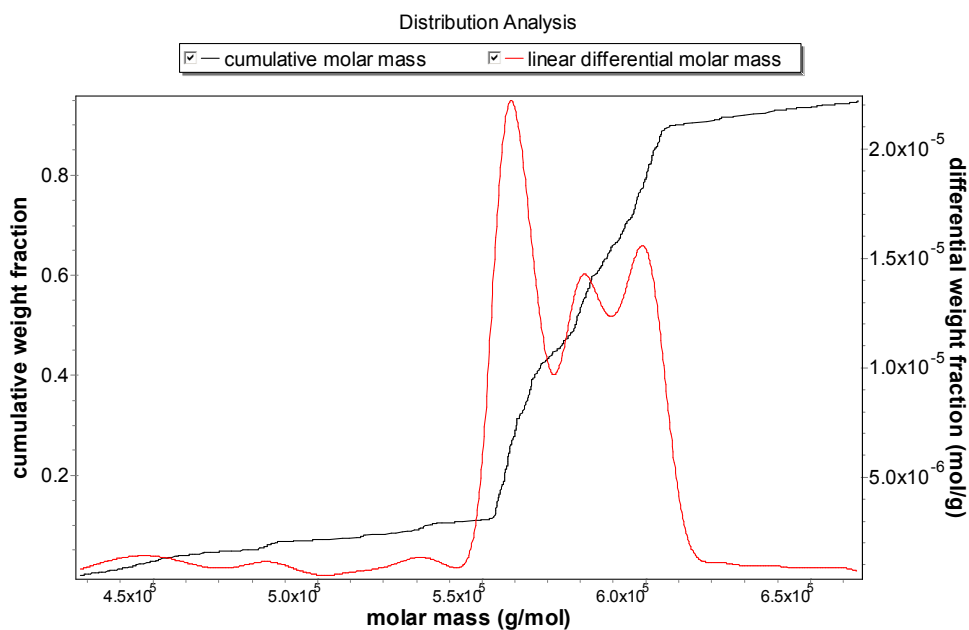


(b)

Figure 1.14. Elution and R_h diagram (a), distribution analysis of the cumulative molar mass and linear differential molar mass (b) of the synthesized PVP nanohydrogels ($c = 0.45 \times 10^{-2} \text{ mol L}^{-1}$) with e-beam irradiation of 10 kGy at 77°C (pulse repetition rate = 20 Hz).

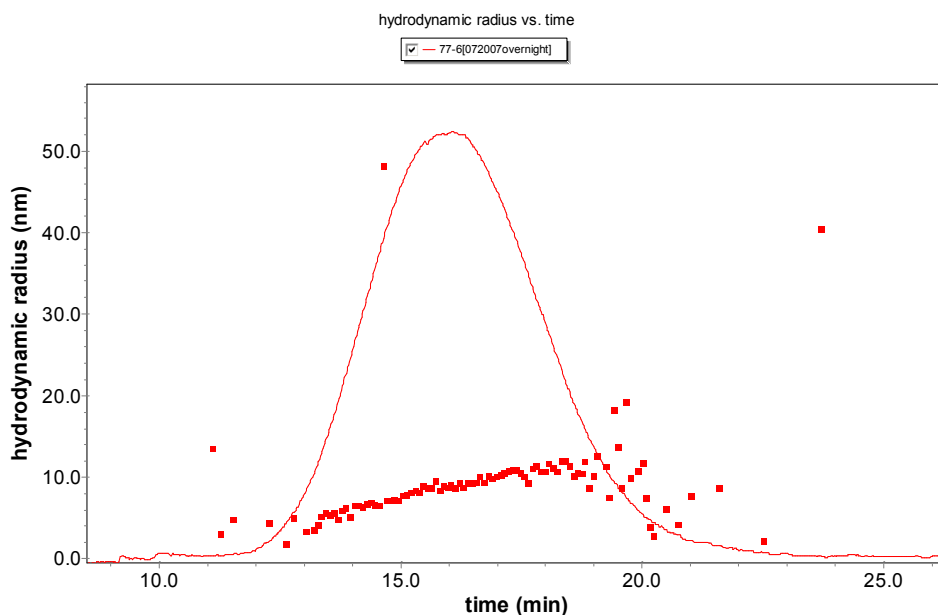


(a)

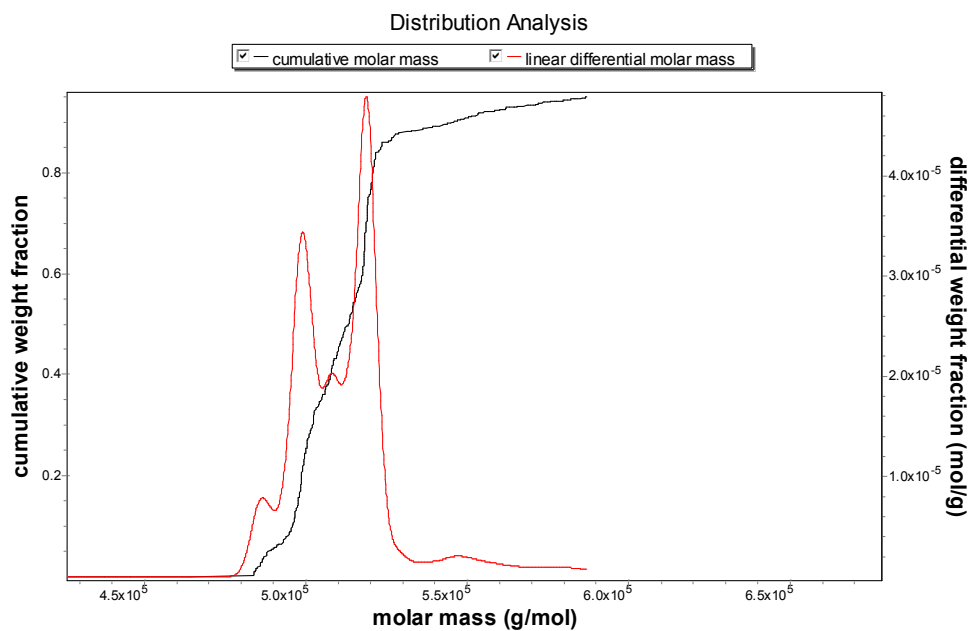


(b)

Figure 1.15. Elution and R_h diagram (a), distribution analysis of the cumulative molar mass and linear differential molar mass (b) of the synthesized PVP nanohydrogels ($c = 0.45 \times 10^{-2} \text{ mol L}^{-1}$) with e-beam irradiation of 10 kGy at 77°C (pulse repetition rate = 300 Hz).

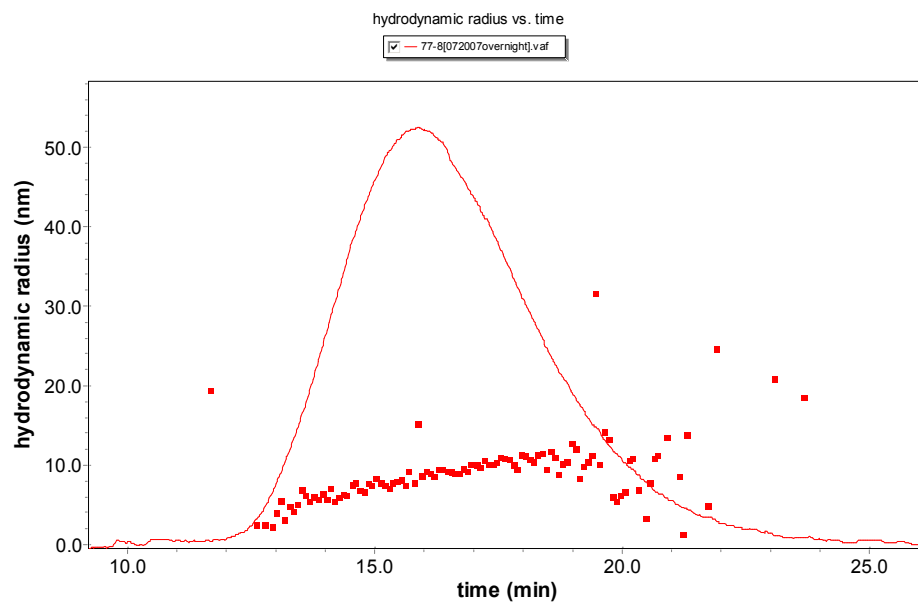


(a)

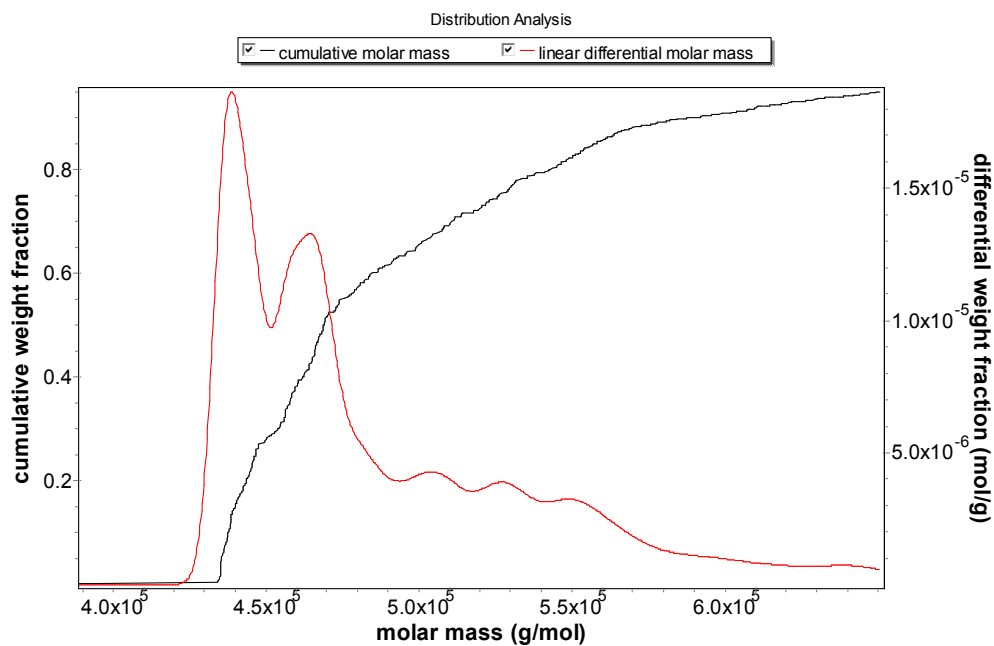


(b)

Figure 1.16. Elution and R_h diagram (a), distribution analysis of the cumulative molar mass and linear differential molar mass (b) of the synthesized PVP nanohydrogels ($c = 0.45 \times 10^{-2} \text{ mol L}^{-1}$) with e-beam irradiation of 5 kGy at 77°C (pulse repetition rate = 20 Hz).

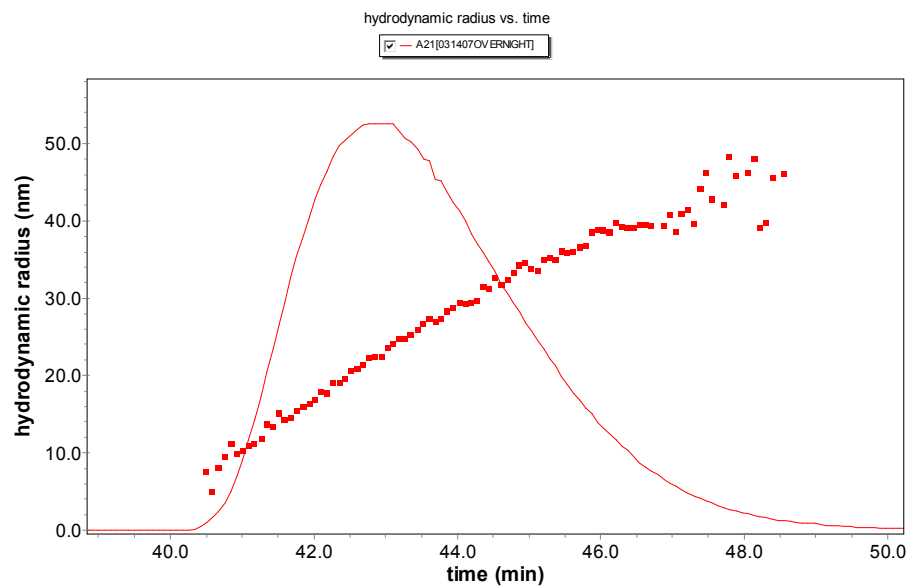


(a)

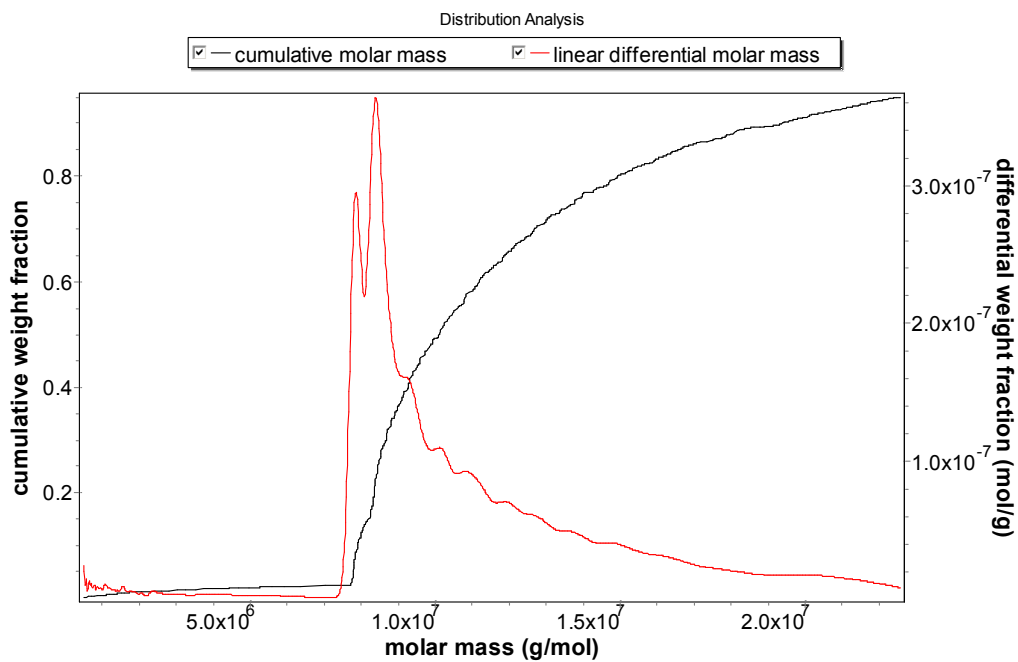


(b)

Figure 1.17. Elution and R_h diagram (a), distribution analysis of the cumulative molar mass and linear differential molar mass (b) of the synthesized PVP nanohydrogels ($c = 0.45 \times 10^{-2} \text{ mol L}^{-1}$) with e-beam irradiation of 5 kGy at 77°C (pulse repetition rate = 300 Hz).



(a)



(b)

Figure 1.18. Elution and R_h diagram (a), distribution analysis of the cumulative molar mass and linear differential molar mass (b) of the synthesized PVP nanohydrogels ($c = 0.9 \times 10^{-2} \text{ mol L}^{-1}$) with γ -ray irradiation of 10 kGy at 10 °C.

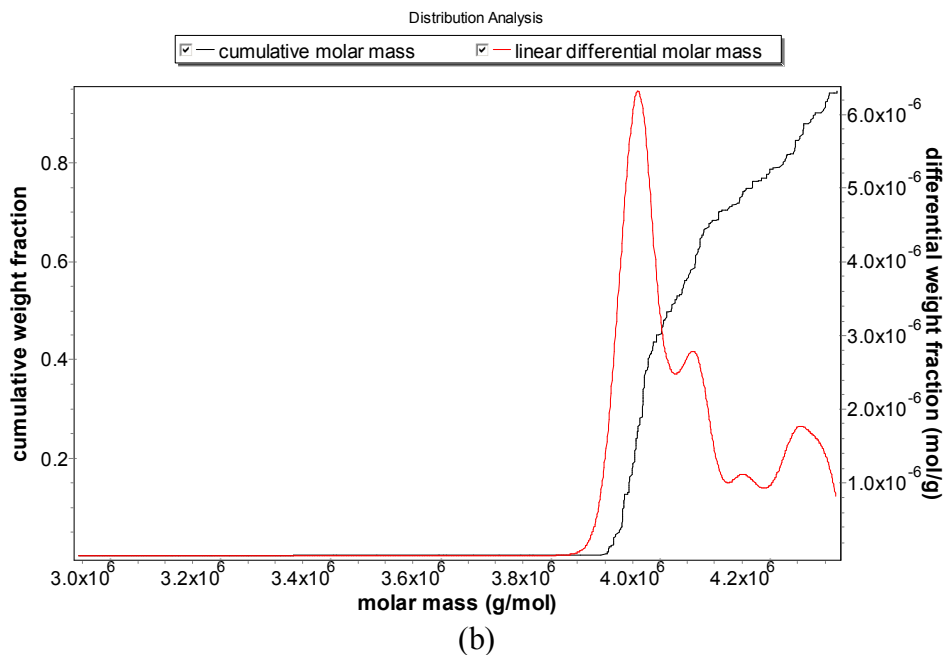
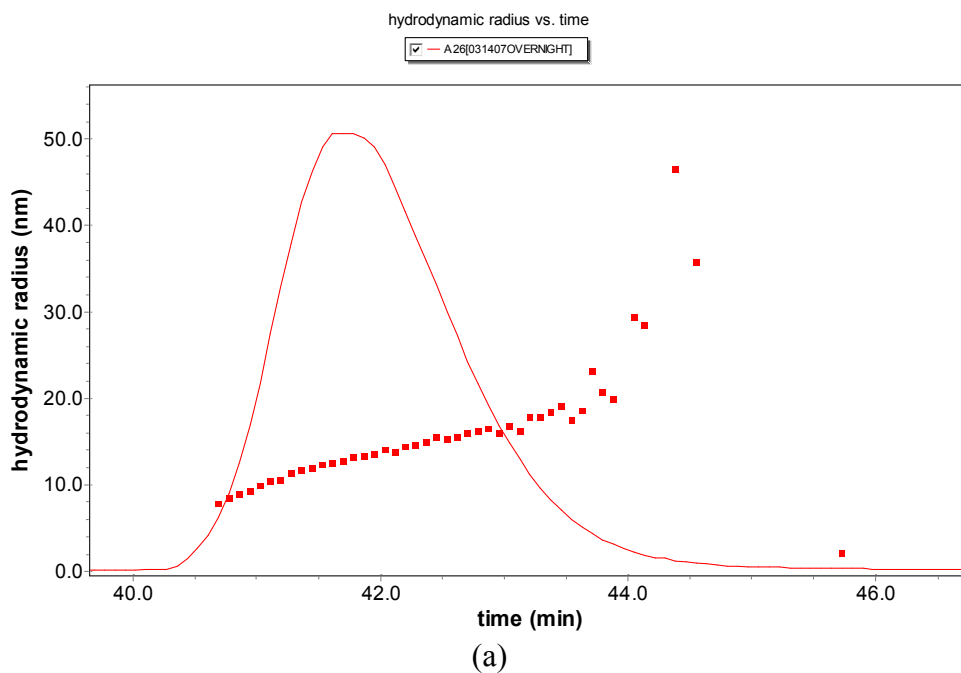


Figure 1.19. Elution and R_h diagram (a), distribution analysis of the cumulative molar mass and linear differential molar mass (b) of the synthesized PVP nanohydrogels ($c = 0.9 \times 10^{-2} \text{ mol L}^{-1}$) with γ -ray irradiation of 10 kGy at 77°C .

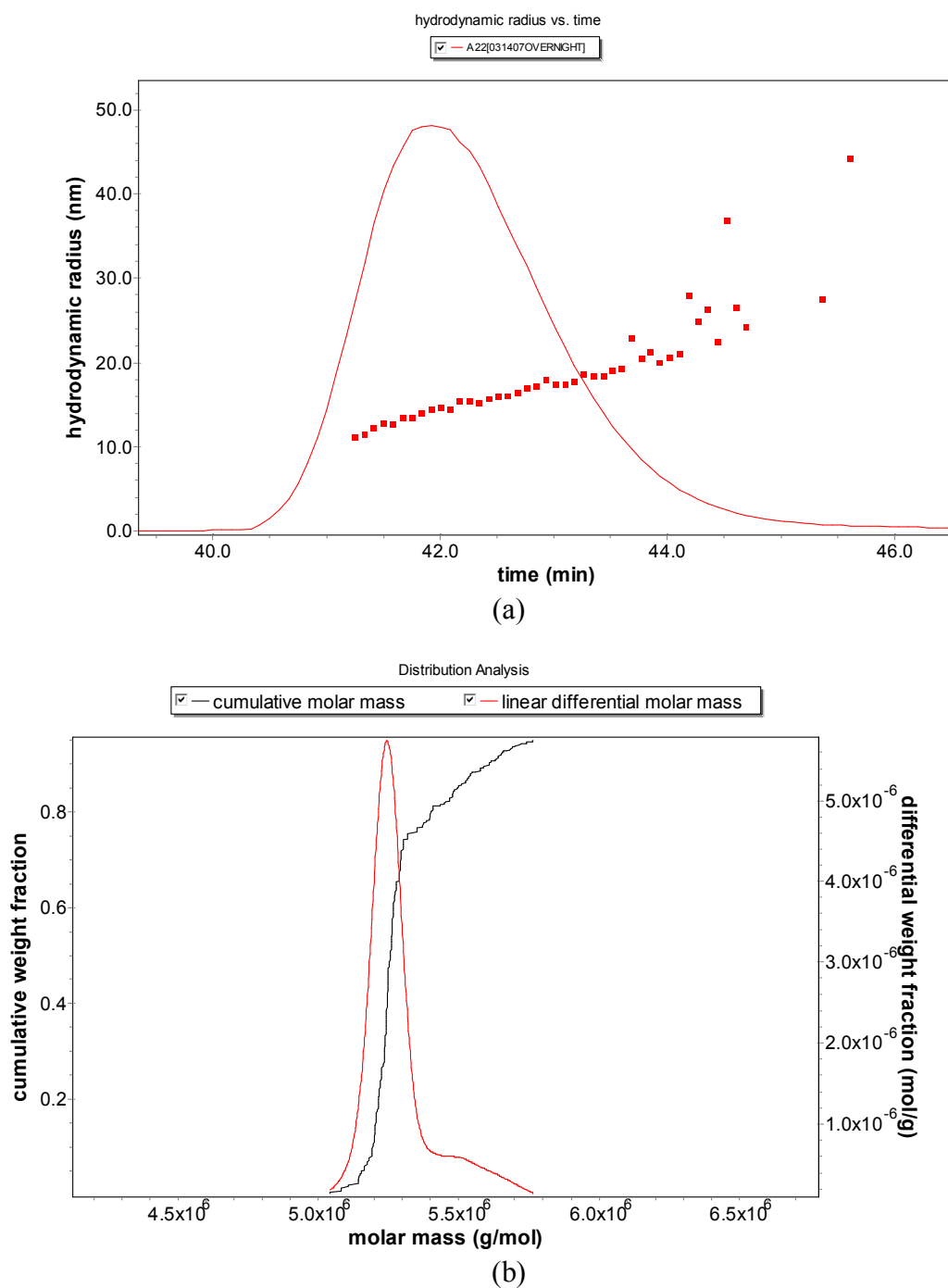


Figure 1.20. Elution and R_h diagram (a), distribution analysis of the cumulative molar mass and linear differential molar mass (b) of the synthesized PVP nanohydrogels ($c = 0.9 \times 10^{-2} \text{ mol L}^{-1}$) with γ -ray irradiation of 5 kGy at 77 °C.

References

1. Kiser, P. F., Wilson, G. and Needham, D., *A synthetic mimic of the secretory granule for drug delivery*. Nature, 1998. **394**(6692): p. 459-462.
2. Kim, B. S., Qiu, J. M., Wang, J. P., and Taton, T. A., *Magnetomicelles: Composite nanostructures from magnetic nanoparticles and cross-linked amphiphilic block copolymers*. Nano Letters, 2005. **5**(10): p. 1987-1991.
3. Liu, S. Y., Weaver, J. V. M., Save, M., and Armes, S. P., *Synthesis of pH-responsive shell cross-linked micelles and their use as nanoreactors for the preparation of gold nanoparticles*. Langmuir, 2002. **18**(22): p. 8350-8357.
4. van der Linden, H., Herber, S., Olthuis, W., and Bergveld, P., *Development of stimulus-sensitive hydrogels suitable for actuators and sensors in microanalytical devices*. Sensors and Materials, 2002. **14**(3): p. 129-139.
5. Kim, S. W., Bae, Y. H. and Okano, T., *Hydrogels - Swelling, Drug Loading, and Release*. Pharmaceutical Research, 1992. **9**(3): p. 283-290.
6. Rosiak, J. M., *Radiation Formation of Hydrogels for Drug-Delivery*. Journal of Controlled Release, 1994. **31**(1): p. 9-19.
7. Ulanski, P., Bothe, E., Hildenbrand, K., Rosiak, J. M., and vonSonntag, C., *Hydroxyl-radical-induced reactions of poly(acrylic acid); A pulse radiolysis, EPR and product study .I. Deoxygenated aqueous solutions*. Journal of the Chemical Society-Perkin Transactions 2, 1996(1): p. 13-22.
8. Safrany, A., *Radiation processing: Synthesis and modification of biomaterials for medical use*. Nuclear Instruments & Methods in Physics Research Section B-Beam Interactions with Materials and Atoms, 1997. **131**(1-4): p. 376-381.
9. Osada, Y., Gong, J. P. and Tanaka, Y., *Polymer gels (Reprinted from Functional Monomers and Polymers, pg 497-528, 1997)*. Journal of Macromolecular Science-Polymer Reviews, 2004. **C44**(1): p. 87-112.
10. Li, Y. and Tanaka, T., *Kinetics of Swelling and Shrinking of Gels*. Journal of Chemical Physics, 1990. **92**(2): p. 1365-1371.
11. Okano, T., *Advances in polymeric systems for drug delivery*. Vol. 4. 1994, Weitzerland: Gordon and Breach Science Publishers.
12. Kohn, J., *Biodegradable polymers as drug delivery systems*. 1990, Newyork: Langer. 195.
13. Funke, W., Okay, O. and Joos-Muller, B., *Microgels - Intramolecularly crosslinked macromolecules with a globular structure*. Microencapsulation - Microgels - Iniferters, 1998. **136**: p. 139-234.

14. Tobita, H., Kumagai, M. and Aoyagi, N., *Microgel formation in emulsion polymerization*. Polymer, 2000. **41**(2): p. 481-487.
15. Rosiak, J. M. and Ulanski, P., *Synthesis of hydrogels by irradiation of polymers in aqueous solution*. Radiation Physics and Chemistry, 1999. **55**(2): p. 139-151.
16. Ulanski, P., Janik, I. and Rosiak, J. M., *Radiation formation of polymeric nanogels*. Radiation Physics and Chemistry, 1998. **52**(1-6): p. 289-294.
17. Ulanski, P. and Rosiak, J. M., *The use of radiation technique in the synthesis of polymeric nanogels*. Nuclear Instruments & Methods in Physics Research Section B-Beam Interactions with Materials and Atoms, 1999. **151**(1-4): p. 356-360.
18. Okada, H., *Theme title: Biodegradable microspheres for therapeutic peptide delivery - Preface*. Advanced Drug Delivery Reviews, 1997. **28**(1): p. 1-3.
19. Langer, R., *Drug delivery and targeting*. Nature, 1998. **392**(6679): p. 5-10.
20. Tanaka, T. and Fillmore, D. J., *Kinetics of Swelling of Gels*. Journal of Chemical Physics, 1979. **70**(3): p. 1214-1218.
21. Stolnik, S., Illum, L. and Davis, S. S., *Long Circulating Microparticulate Drug Carriers*. Advanced Drug Delivery Reviews, 1995. **16**(2-3): p. 195-214.
22. Vinogradov, S. V., Bronich, T. K. and Kabanov, A. V., *Nanosized cationic hydrogels for drug delivery: preparation, properties and interactions with cells*. Advanced Drug Delivery Reviews, 2002. **54**(1): p. 135-147.
23. Ishida, O., Maruyama, K., Sasaki, K., and Iwatsuru, M., *Size-dependent extravasation and interstitial localization of polyethyleneglycol liposomes in solid tumor-bearing mice*. International Journal of Pharmaceutics, 1999. **190**(1): p. 49-56.
24. Slomkowski, S., Sosnowski, S. and Gadzinowski, M., *Microspheres by dispersion polymerization of lactides and epsilon-caprolactone*. Macromolecular Symposia, 1997. **123**: p. 45-60.
25. Harma, H., Lehtinen, P., Takalo, H., and Lovgren, T., *Immunoassay on a single microparticle: the effect of particle size and number on a miniaturized time-resolved fluorometric assay of free prostate-specific antigen*. Analytica Chimica Acta, 1999. **387**(1): p. 11-19.
26. Doherty, E. A. S., Kan, C. W. and Barron, A. E., *Sparsely cross-linked "nanogels" for microchannel DNA sequencing*. Electrophoresis, 2003. **24**(24): p. 4170-4180.

27. Spinks J. W., Woods R. J., *An Introduction to Radiation Chemistry*. third ed. 1990, New York: John Wiley and Sons, Inc.
28. Woods R. J., Pikaev A.K., *Applied Radiation Chemistry, Radiation Processing*. 1994, New York: John Wiley and Sons, Inc.
29. Chatterjee, A., *Interaction of ionizing radiation with matter*. Radiation Chemistry, Principles and Applications, ed. Farataziz, M. Rodgers. 1987, New York: VCH Publishers Inc. 1-28.
30. Sonntag, C. V., *The Chemical Basis of Radiation Biology*. 1987, Philadelphia: Taylor & Francis.
31. Henglein A., Schnabel W., Wendenburg J., *Einführung in die strahlenchemie mit partischen anleitungen*. 1969, Weinheim/Bergstr: Verlag Chemie, GMBH.
32. Sheien B., Slabac L. A., Barky B. K., *Handbook of Health Physics and Radiological Health*. 1998, Baltimore: Williams & Wilkins.
33. Buxton, G. V., *Radiation chemistry of the liquid state: (1) water and homogeneous aqueous solutions* *Radiation Chemistry Principles and Applications*, ed. Rogers, Farhataziz and M A J. 1987, New York: VCH. 321-349.
34. Magee, J.L and Chatterjee, A., *Theoretical aspects of radiation chemistry* *Radiation Chemistry, Principles and Applications*, ed. Rodgers, Farataziz and M. 1987, New York: VCH Publishers Inc. 148.
35. Schuchmann, M. N. and Sonntag, C. V., *Radiation-Chemistry of Carbohydrates .14. Hydroxyl Radical Induced Oxidation of D-Glucose in Oxygenated Aqueous-Solution*. *Journal of the Chemical Society-Perkin Transactions 2*, 1977(14): p. 1958-1963.
36. Steenken, S. and O'Neill, P., *Selectivity of addition of the hydroxyl radical to ring positions of pyridine and pyridine mono- and dicarboxylic acids, An electron spin resonance investigation*. *Journal of Physical Chemistry*, 1978. **82**: p. 372-374.
37. Anbar, M., Meyerste.D and Neta, P., *Reactivity of Aromatic Compounds toward Hydroxyl Radicals*. *Journal of Physical Chemistry*, 1966. **70**(8): p. 2660-&.
38. Farahataziz and Rodgers, M.A., *Radiation Chemistry, Principles and Applications*. 1987, New York: VCH Publishers, Inc.
39. Janata, E and Schuler, R. H., *Rate constant for scavenging e^-_{aq} in N_2O -saturated solutions*. *Journal of Physical Chemistry*, 1982. **86**: p. 2078-2084.

40. Jones, C. G., *Radiation-induced remediation of polychlorinated biphenyls contained in industrial transformer oil from electrical generating stations*. 2001.
41. Swallow, A. J., *Radiation Chemistry, an Introduction*. 1973, New York: John Wiley and Sons.
42. Far West Technology (FWT) Inc. Address: Suite D, 330 South Kellogg Ave., Goleta, CA 93117, U.S.A.
43. Davis, J. E., Sangster, D. F. and Senogles, E., *Pulse-Radiolysis of Aqueous-Solutions of N-Vinylpyrrolidin-2-One and Poly(N-Vinylpyrrolidin-2-One)*. Australian Journal of Chemistry, 1981. **34**(7): p. 1423-1431.
44. L. M. Dorfman, M. S. Matheson, *Pulse Radiolysis*. Progress in Reaction Kinetics. Vol. 3. 1965, New York: Pergamon Press.
45. Pecora, R., *Dynamic light scattering: applications of photon correlation spectroscopy*. 1985, New York: Plenum Press.
46. KS, Schmitz, *An introduction to dynamic light scattering by macromolecules*. 1990, New York: Academic Press Inc.
47. Phillies, G. D. J., *Quasi-Elastic Light-Scattering*. Analytical Chemistry, 1990. **62**(20): p. A1049-a1057.
48. Giddings, J. C., *Conceptual Basis of Field-Flow Fractionation*. Journal of Chemical Education, 1973. **50**(10): p. 667-669.
49. Ratanathanawongs, S. K. and J. C. Giddings. *Chromatography of Polymers*. in *ACS Symp. Series*. 1993. Washington DC: American Chemical Society.
50. Giddings, J. C., Myers, M. N., Lin, G. C., and Martin, M., *Polymer Analysis and Characterization by Field-Flow Fractionation (One-Phase Chromatography)*. Journal of Chromatography, 1977. **142**(Nov): p. 23-38.
51. Venema, E., deLeeuw, P., Kraak, J. C., Poppe, H., and Tijssen, R., *Polymer characterization using on-line coupling of thermal field flow fractionation and hydrodynamic chromatography*. Journal of Chromatography A, 1997. **765**(2): p. 135-144.
52. Li, P., Hansen, M. and Giddings, J. C., *Separation of lipoproteins from human plasma by flow field-flow fractionation*. Journal of Liquid Chromatography & Related Technologies, 1997. **20**(16-17): p. 2777-2802.
53. Giddings, J. C., Yang, F. J. and Myers, M. N., *Flow Field-Flow Fractionation - New Method for Separating, Purifying, and Characterizing Diffusivity of Viruses*. Journal of Virology, 1977. **21**(1): p. 131-138.

54. Schimpf M., Caldwell K. and Giddings J. C., *Field-Flow Fractionation Handbook*. 2000, New York: John Wiley & Sons, Inc. 592.
55. Giddings, J. C., Yang, F. J. F. and Myers, M. N., *Flow Field-Flow Fractionation - Versatile New Separation Method*. Science, 1976. **193**(4259): p. 1244-1245.
56. Pasch, H and Trathnigg, B., *HPLC of Polymers*. Springer Desktop Editions of Chemistry. 1999, New York: Springer.
57. Roessner, D., *Field Flow Fractionation - Basics and Method Development*. 2006, Wyatt Technology Europe.
58. Blanchard, C. R. and Campbell, J. B., *Atomic-Force Microscopy*. Advanced Materials & Processes, 1995. **148**(2): p. 62-62.
59. Yang, Z. Z. and Niu, Z. W., *Binary hydrogel nanowires of invertible core/shell phases prepared in porous alumina membranes*. Chemical Communications, 2002(17): p. 1972-1973.
60. Ratner, B. D., Tsukruk, V. V., *Scanning Probe Microscopy of Polymers*. ACS Symposium Series. 1996, Washington DC: American Chemical Society.
61. J. I. Goldstein, D. E. Newbury, P. Echlin, D. C. Joy, C. Fiori, E Lifshin, *Scanning electron microscopy and X-ray microanalysis*. 1981, New York: Plenum press.
62. Bharali, D. J., Sahoo, S. K., Mozumdar, S., and Maitra, A., *Cross-linked polyvinylpyrrolidone nanoparticles: a potential carrier for hydrophilic drugs*. Journal of Colloid and Interface Science, 2003. **258**(2): p. 415-423.
63. Dasilveira, B. I., *Diffusion in Polyvinylpyrrolidone Hydrogels Prepared by Radiation Technique*. European Polymer Journal, 1993. **29**(8): p. 1095-1098.
64. Lugao, A. B., Rogero, S. O. and Malmonge, S. M., *Rheological behaviour of irradiated wound dressing poly(vinyl pyrrolidone) hydrogels*. Radiation Physics and Chemistry, 2002. **63**(3-6): p. 543-546.
65. Benamer, S., Mahlous, M., Boukrif, A., Mansouri, B., and Youcef, S. L., *Synthesis and characterisation of hydrogels based on poly(vinyl pyrrolidone)*. Nuclear Instruments & Methods in Physics Research Section B-Beam Interactions with Materials and Atoms, 2006. **248**(2): p. 284-290.
66. Wang, B. L., Mukataka, S., Kodama, M., and Kokufuta, E., *Viscometric and light scattering studies on microgel formation by gamma-ray irradiation to aqueous oxygen-free solutions of poly(vinyl alcohol)*. Langmuir, 1997. **13**(23): p. 6108-6114.

67. Wang, B.; Mukataka, S; Kokufuta, E; Ogiso, M.; Kodama, M. J., *Viscometric, light scattering, and size-exclusion chromatography studies on the structural changes of aqueous poly(vinyl alcohol) induced by γ -ray irradiation*. J. Polym. Sci., Part B: Polym. Phys., 2000. **38**(1): p. 214-221.
68. Mporu, P., Addai-Mensah, J. and Ralston, J., *Temperature influence of nonionic polyethylene oxide and anionic polyacrylamide on flocculation and dewatering behavior of kaolinite dispersions*. Journal of Colloid and Interface Science, 2004. **271**(1): p. 145-156.
69. Kavlak, S. and Guner, A., *Intermolecular interactions between bovine serum albumin and certain water-soluble polymers at various temperatures*. Journal of Applied Polymer Science, 2006. **100**(2): p. 1554-1560.
70. Matsuyama, A. and Tanaka, F., *Theory of Solvation-Induced Reentrant Phase-Separation in Polymer-Solutions*. Physical Review Letters, 1990. **65**(3): p. 341-344.
71. Flory, P. J., *Principles of Polymer Chemistry*. 1953, Ithaca: Cornell Univ. Press.
72. Degiorgio, V., *Physics of Amphiphiles: Micelles, Vesicles, and Microemulsion*, ed. Degiorgio, V. and Corti, M. 1985, Amsterdam: North-Holland.
73. Maruthamuthu, M. and Subramanian, E., *Binding of Evans Blue onto Poly (N-Vinyl-2-Pyrrolidone)*. Polymer Bulletin, 1985. **14**(3-4): p. 207-212.
74. Charlesby, A., *Atomic Radiation and Polymers*. 1960, Oxford: Pergamon Press.
75. Yang, J.H., Salamanca-Riba, L., An, J.C., Sweet, D., Martínez-Miranda, L.J., Silverman, J., Al-Sheikhly, M., *Brush-like structure of self-assembled DNA Oligonucleotides on Arsenic-terminated GaAs (001)*. (in preparation).
76. Kadlubowski, S., Grobelny, J., Olejniczak, W., Cichomski, M., and Ulanski, P., *Pulses of fast electrons as a tool to synthesize poly(acrylic acid) nanogels. Intramolecular cross-linking of linear polymer chains in additive-free aqueous solution*. Macromolecules, 2003. **36**(7): p. 2484-2492.
77. Teraoka, Iwao, *Polymer solutions*. 2002, New York: John Wiley & Sons., Inc. 197.
78. Ulanski, P. and Rosiak, J. M., *Pulse-Radiolysis of Poly(Acrylic Acid) in Deoxygenated Aqueous-Solution*. Journal of Radioanalytical and Nuclear Chemistry-Letters, 1994. **186**(4): p. 315-324.

79. Rosiak, J. M., Ulanski, P., Pajewski, L. A., Yoshii, F., and Makuuchi, K., *Radiation Formation of Hydrogels for Biomedical Purposes - Some Remarks and Comments*. Radiation Physics and Chemistry, 1995. **46**(2): p. 161-168.
80. Ulanski, P., Bothe, E., Hildenbrand, K., Rosiak, J. M., and Vonsontag, C., *Radiolysis of Poly(Acrylic Acid) in Aqueous-Solution*. Radiation Physics and Chemistry, 1995. **46**(4-6): p. 909-912.
81. Ulanski, P., Bothe, E., Hildenbrand, K., Rosiak, J. M., and vonSonntag, C., *Hydroxyl-radical-induced reactions of poly(acrylic acid); A pulse radiolysis, EPR and product study .2. Oxygenated aqueous solutions*. Journal of the Chemical Society-Perkin Transactions 2, 1996(1): p. 23-28.
82. Ulanski, P., Zainuddin and Rosiak, J. M., *Pulse-Radiolysis of Poly(Ethylene Oxide) in Aqueous-Solution .2. Decay of Macroradicals*. Radiation Physics and Chemistry, 1995. **46**(4-6): p. 917-920.
83. Safrany, A. and Wojnarovits, L., *First steps in radiation-induced hydrogel synthesis: radical formation and oligomerization in dilute aqueous N-isopropylacrylamide solutions*. Radiation Physics and Chemistry, 2003. **67**(6): p. 707-715.
84. Strauss, P., Knolle, W. and Naumov, S., *Radiation-induced radical formation and crosslinking in aqueous solutions of N-isopropylacrylamide*. Macromolecular Chemistry and Physics, 1998. **199**(10): p. 2229-2235.
85. Kujawa, P., Ulanski, P. and Rosiak, J. M., *Time-resolved investigations of pulse-initiated polymerization*. Radiation Physics and Chemistry, 1998. **52**(1-6): p. 389-393.
86. Gabel, R. A. and Schultz, B., *Solubility of Nitrous-Oxide in Water, 20-80 C*. Anesthesiology, 1973. **38**(1): p. 75-81.
87. Moon, S. I. and McCarthy, T. J., *Template synthesis and self-assembly of nanoscopic polymer "pencils"*. Macromolecules, 2003. **36**(12): p. 4253-4255.
88. Qiao, J. J., Zhang, X. H., Meng, X. M., Zhou, S. M., Wu, S. K., and Lee, S. T., *Morphology-controllable preparation of 1D poly(vinyl pyrrolidone) nanostructured arrays*. Nanotechnology, 2005. **16**(4): p. 433-436.
89. Rubinstein, M. and Colby, R., *Polymer Physics*. 2003, New York: Oxford University Press Inc.
90. Yoshida, W. and Cohen, Y., *Ceramic-supported polymer membranes for pervaporation of binary organic/organic mixtures*. Journal of Membrane Science, 2003. **213**(1-2): p. 145-157.

91. Batchelor, G. K., *An Introduction To Fluid Dynamics*. 1967, London: Cambridge University Press.
92. Huang, Q. R. and Wang, C. H., *Surface laser light scattering studies of the air/poly(N-vinyl-2-pyrrolidone)-water solution interface*. Journal of Chemical Physics, 1996. **105**(15): p. 6546-6552.
93. Dispenza, C., Lo Presti, C., Belfiore, C., Spadaro, G., and Piazza, S., *Electrically conductive hydrogel composites made of polyaniline nanoparticles and poly(N-vinyl-2-pyrrolidone)*. Polymer, 2006. **47**(4): p. 961-971.
94. Zrinyi, M., Barsi, L. and Buki, A., *Deformation of ferrogels induced by nonuniform magnetic fields*. Journal of Chemical Physics, 1996. **104**(21): p. 8750-8756.
95. Kong, Q., Chen, X. G., Yao, J. L., and Xue, D. S., *Preparation of poly(N-vinyl-2-pyrrolidone)-stabilized transition metal (Fe, Co, Ni and Cu) hexacyanoferrate nanoparticles*. Nanotechnology, 2005. **16**(1): p. 164-168.
96. Szabo, D., Barsi, L., Buki, A., and Zrinyi, M., *Studies on nonhomogeneous deformation in magnetic field sensitive gels*. Ach-Models in Chemistry, 1997. **134**(2-3): p. 155-167.
97. Barsi, L. and Zrinyi, M., *Ferrogels as magnetomechanical actuators*. Ach-Models in Chemistry, 1998. **135**(3): p. 241-246.
98. Starodubtsev, S. G., Saenko, E. V., Dokukin, M. E., Aksenov, V. L., Klechkovskaya, V. V., Zanaveskina, I. S., and Khokhlov, A. R., *Formation of magnetite nanoparticles in poly(acrylamide) gels*. Journal of Physics-Condensed Matter, 2005. **17**(10): p. 1471-1480.
99. Zhang, Z. T., Zhao, B. and Hu, L. M., *PVP protective mechanism of ultrafine silver powder synthesized by chemical reduction processes*. Journal of Solid State Chemistry, 1996. **121**(1): p. 105-110.
100. Lu, X. F., Li, L. L., Zhang, W. J., and Wang, C., *Preparation and characterization of Ag₂S nanoparticles embedded in polymer fibre matrices by electrospinning*. Nanotechnology, 2005. **16**(10): p. 2233-2237.
101. Ben-Naim, *Hydrophobic Interactions*. 1980, New York: Plenum.
102. Matteoli, E. and Lepori, L., *Solute Solute Interactions in Water .2. An Analysis through the Kirkwood-Buff Integrals for 14 Organic Solutes*. Journal of Chemical Physics, 1984. **80**(6): p. 2856-2863.
103. Blandamer, M. J., Burgess, J., Cooney, A., Cowles, H. J., Horn, I. M., Martin, K. J., Morcom, K. W. and Warrick P. Jr., *Excess molar Gibbs energies of*

mixing of water and 1,1,1,3,3,3-hexafluoropropan-2-ol mixtures at 298.15 K. Comparison of thermodynamic properties and inverse Kirkwood–Buff integral functions for binary aqueous mixtures formed by ethanol, propan-2-ol, 2,2,2-trifluoroethanol and 1,1,1,3,3,3-hexafluoropropan-2-ol. Journal of the Chemical Society, Faraday Transactions, 1990. **86**: p. 2209-2213.

104. Hu, Z. B., Lu, X. H., Gao, J., and Wang, C. J., *Polymer gel nanoparticle networks.* Advanced Materials, 2000. **12**(16): p. 1173-1176.